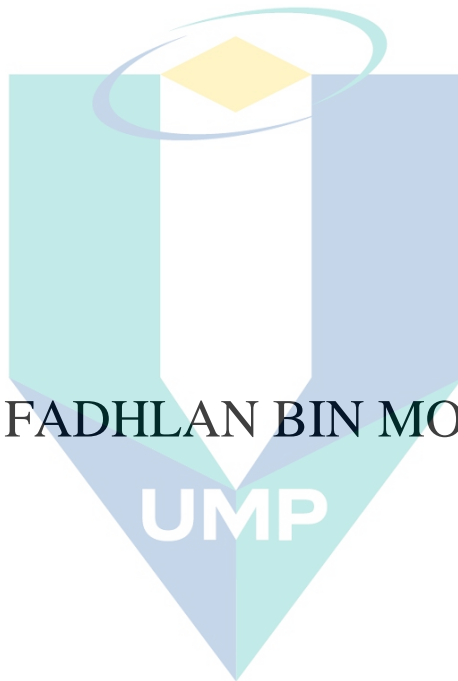# MONITORING AND ASSESSMENT OF WELD PENETRATION CONDITION DURING PULSE MODE LASER WELDING USING AIR-BORNE ACOUSTIC SIGNAL

MOHD FADHLAN BIN MOHD YUSOF

Doctor of Philosophy

UNIVERSITI MALAYSIA PAHANG

UNIVERSITI MALAYSIA PAHANG

DECLARATION OF THESIS AND COPYRIGHT

Author's Full Name : <u>MOHD FADHLAN BIN MOHD YUSOF</u>

Date of Birth : <u>5 OCTOBER 1985</u>

Title : <u>MONITORING AND ASSESSMENT OF WELD</u>
<u>PENETRATION CONDITION DURING PULSE MODE</u>
<u>LASER WELDING USING AIR-BORNE ACOUSTIC</u>
<u>SIGNAL</u>

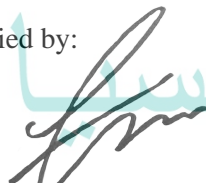Academic Session : <u>SEMESTER 2 2020/2021</u>

I declare that this thesis is classified as:

☐ CONFIDENTIAL (Contains confidential information under the Official Secret Act 1997)*

☐ RESTRICTED (Contains restricted information as specified by the organization where research was done)*

☒ OPEN ACCESS I agree that my thesis to be published as online open access (Full Text)

I acknowledge that Universiti Malaysia Pahang reserves the following rights:

1. The Thesis is the Property of Universiti Malaysia Pahang
2. The Library of Universiti Malaysia Pahang has the right to make copies of the thesis for the purpose of research only.
3. The Library has the right to make copies of the thesis for academic exchange.

Certified by:

_____
(Student's Signature)

851005-06-5125
_____
New IC/Passport Number
Date: 4 / 6 / 2021

_____
(Supervisor's Signature)

PROF. DR. MAHADZIR ISHAK
@ MUHAMMAD
_____
Name of Supervisor
Date: 4/6/2021

NOTE : * If the thesis is CONFIDENTIAL or RESTRICTED, please attach a thesis declaration letter.

SUPERVISOR'S DECLARATION

We hereby declare that We have checked this thesis and in our opinion, this thesis is adequate in terms of scope and quality for the award of the degree of Doctor of Philosophy.

_____

(Supervisor's Signature)

Full Name   : DR. MAHADZIR ISHAK@MUHAMMAD

Position   : PROFESSOR

Date   : 4/6/2021

_____

(Co-supervisor's Signature)

Full Name   : IR. DR. MOHD FAIRUSHAM GHAZALI

Position   : ASSOCIATE PROFESSOR

Date   : 4 / 6 / 2021

STUDENT'S DECLARATION

I hereby declare that the work in this thesis is based on my original work except for quotations and citations which have been duly acknowledged. I also declare that it has not been previously or concurrently submitted for any other degree at Universiti Malaysia Pahang or any other institutions.

_____

(Student's Signature)

Full Name   : MOHD FADHLAN BIN MOHD YUSOF
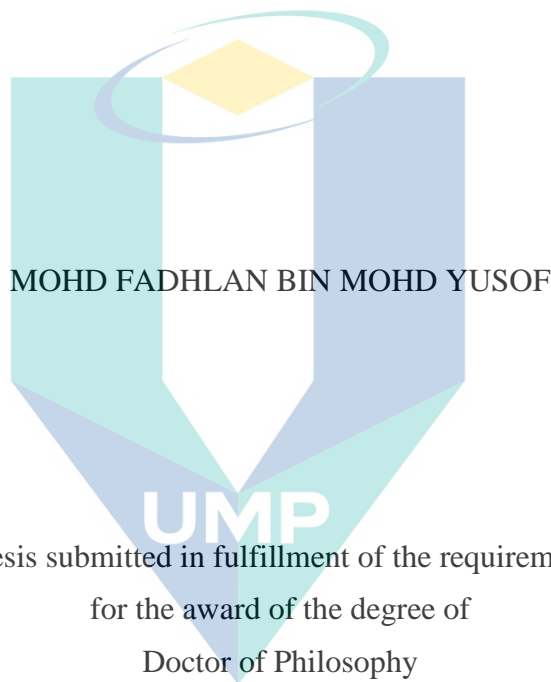ID Number   : PMM16020
Date   : 4 / 6 / 2021

MONITORING AND ASSESSMENT OF WELD PENETRATION CONDITION
DURING PULSE MODE LASER WELDING USING AIR-BORNE ACOUSTIC
SIGNAL

MOHD FADHLAN BIN MOHD YUSOF

Thesis submitted in fulfillment of the requirements

for the award of the degree of

Doctor of Philosophy

Faculty of Mechanical & Automotive Engineering Technology

UNIVERSITI MALAYSIA PAHANG

JUNE 2021

ACKNOWLEDGEMENTS

ABSTRAK

Sistem pemantauan secara atas talian merupakan kriteria penting dalam sistem pembuatan di dalam era revolusi industry 4.0. Dalam aplikasi kimpalan laser, kaedah akustik adalah merupakan salah satu kaedah yang menarik perhatian para pengkaji atas beberapa kelebihan utama seperti, sistem yang ringkas, kos yang rendah dan penderia yang tidak bersentuhan. Namun, mengaplikasikan kaedah ini dalam proses kimpalan laser mod denyutan (PW) adalah sangat mencabar disebabkan sifat isyarat dan hingar yang berbeza diperoleh semasa proses ini berbanding proses laser mod berterusan (CW). Justeru, kajian ini menyasarkan untuk mengkaji sifat isyarat akustik yang diperoleh dari proses kimpalan PW, membangunkan algorithma pemprosesan isyarat yang dapat mengekstrak ciri isyarat bunyi yang kurang dipengaruhi hingar, serta membangunkan model impirikal yang dapat menganggar kedalaman kimpalan semasa proses. Bagi mencapai kesemua objektif, proses kimpalan laser dengan variasi kuasa puncak, dan durasi denyutan telah dijalankan keatas keluli boron 22MnB5 dengan ketebalan 1.8 mm. Semasa proses kimpalan, isyarat bunyi telah dicerap antara frekuensi 20 Hz hingga 12.8 kHz. Ciri isyarat seperti sisihan min mutlak (MAD), sisihan piawai (SD), kurtosis, skala-L, kurtosis-L, kuasa jalur dan jumlah pekali anak gelombang pemerahan-segerak (CSqWCsum), telah diekstrak dari isyarat yang dicerap. Bagi membangunkan algoritma pemprosesan isyarat, kaedah Ruang fasa berbilang-bebatan (MLPS) telah dimodifikasi dengan cara memperkenalkan teknik ambang faktor puncak (CF) untuk mengurangkan pengaruh hingar. Keputusan menunjukkan bahawa isyarat bunyi yang dicerap adalah merupakan isyarat jenis denyutan dimana amplitudnya merekodkan sedikit perubahan keatas perubahan parameter kimpalan. Manakala, frekuensi dominan telah direkodkan sekitar 5760 Hz hingga 7000 Hz tanpa perubahan yang jelas terhadap perubahan parameter kimpalan. Keputusan analisis pemilihan ciri isyarat pula menunjukkan bahawa SD, kurtosis-L, dan MLPS-termodifikasi mencatatkan hubungan yang signifikan dengan kedalaman kimpalan. Kombinasi antara ketiga-tiga ciri ini dengan kuasa puncak laser dan durasi denyutan pula mencatatkan corak regresi yang lebih baik dengan Kuasa dua-R Terlaras yang direkodkan adalah 0.937. Dua model empirikal telah dibangunkan dengan kombinasi ketiga-tiga ciri isyarat dengan parameter kimpalan menggunakan kaedah Regresi Lelurus Berbilang (MLR) dan Rangkaian Neural Buatan (ANN). Melalui kaedah MLR, model yang diperoleh adalah DOP = 0.634SD - 0.814LK + 0.0014MLPS + 116.44PD + 0.0014PP - 0.7781. Keputusan analisis validasi menunjukkan bahawa kedua-dua model dapat menganggar kedalaman kimpalan dengan purata ralat kurang daripada 8%. Namun model ANN telah merekodkan anggaran yang lebih tepat dan jitu dengan purata ralat anggaran sebanyak 3.3%. Keputusan kajian ini menunjukkan bahawa kaedah akustik dapat digunakan untuk memantau kedalaman kimpalan secara atas-talian semasa proses PW. Melalui kaedah ini, kedalaman kimpalan dapat dinilai secara kuantitatif semasa proses PW. Penemuan ini dapat memberikan solusi kepada pembangunan sistem pemantauan secara masa-nyata keatas proses kimpalan laser PW, dimana ianya sejajar dengan keperluan utama dalam era baru sistem pembuatan.

ABSTRACT

Real-time monitoring system is one of the essential criteria in the era of the fourth industrial revolution (Industry 4.0). Among the monitoring systems in laser welding applications, acoustic methods have recently caught the attention of researchers due to their benefits in promoting simple, low-cost, and non-contact systems. However, applying this method in PW mode laser was challenging due to the different characteristic of signal and noise acquired from this process as compared to CW process. Therefore, this particular work aims to investigate the characteristics of acoustic sound signal from PW Fiber laser, develop an appropriate signal processing algorithm to suppress the effect of noise on the extracted sound features, and develop an empirical model for weld depth estimation. To achieve the objectives, a 1.8 mm thick 22MnB5 boron steel plate was welded with varied laser peak power (PP) and pulse duration (PD) levels. Simultaneously, the sound signal was acquired between the frequency of 20 Hz to 12.8 kHz throughout the process. Signal features, such as mean absolute deviation (MAD), standard deviation (SD), kurtosis (K), L-scale (LS), L-kurtosis (LK), bandpower (BP), and sum of synchrosqueezed wavelet coefficient (CSqWCsum) were extracted from the acquired sound. To develop the signal processing algorithm, multi-lag phase space (MLPS) method was adopted in which some modifications on its original algorithm were made by introducing the localized crest factor (CF) thresholding method to reduce the influence of noise. Results showed that the acquired sound recorded transient behaviors with a slight change in its overall amplitudes with respect to the change in the level of weld parameters. Meanwhile, the dominant frequency was found to be fluctuated between 5760 Hz and 7000 Hz without a clear pattern in the case of different levels of weld parameters involved in this study. The results from feature selection analysis show that the combination of SD, L-kurtosis, and modified-MLPS recorded the most significant relation with weld penetration. Furthermore, the combination of these features with the laser peak power and pulse duration recorded a better regression trend with an adjusted R-squared of 0.937. Two empirical models for weld depth estimation were developed from the combination of these sound features and weld parameters using the multiple linear regression (MLR) and artificial neural network (ANN) methods. Through MLR method, the obtained model was DOP = 0.634SD - 0.814LK + 0.0014MLPS + 116.44PD + 0.0014PP - 0.7781. Results from the model validation analysis showed that both models could significantly estimate weld penetration during the PW laser welding process with an estimation error less than 8%. However, the ANN model recorded a more accurate and precise estimation with the lowest estimation error, i.e., 3.3%. The results of the analysis suggest that the acoustic methods can be used to monitor weld penetration on a real-time basis during PW mode laser welding process. Moreover, the methods can also be used to provide a quantitative assessment on weld penetration during the process. This finding gives alternative solution to the development of a real-time process monitoring system in PW mode laser welding, which aligns with the criteria needed in the new era of manufacturing system.

TABLE OF CONTENT

LIST OF TABLES

LIST OF FIGURES

LIST OF SYMBOLS

E	Laser energy
P_{pk}	Laser peak power
t_p	Pulse duration
P_{avg}	Average laser power
f	Frequency of acoustic signals
Td	Damping coefficient
g	unsaturated gain
$g_e,$	gain at threshold
t_S	lifetime of the upper laser level
t_C	photon cavity lifetime
m	vapor creation rate
β	created vapor
ρ_m	vapor density
ρ_f	the density of the ambient fluid
x_i	amplitude
N	Number of amplitudes samples
L_1	First order moment
L_2	Second Order Moment
L_4	Fourth Order Moment
W_x	Wavelet Coefficient
T_x	synchrosqueezed wavelet coefficient
a	scales
b	Shifting constant
ω	Radial frequency
ω_0	Central radial frequency
φ^*	Mother wavelet
v_w	Instantaneous frequency
$v_j,$	phase space vector
m	dimension of phase space
τ	lag between the sample

M	total dimension of phase space
$\lambda_{sqtwolog}$	Sqtwolog threshold
$\lambda_{rigrsure}$	Rigrsure threshold
$\lambda_{minimaxi}$	Minimaxi threshold
λ_{CF}	Localize crest factor threshold
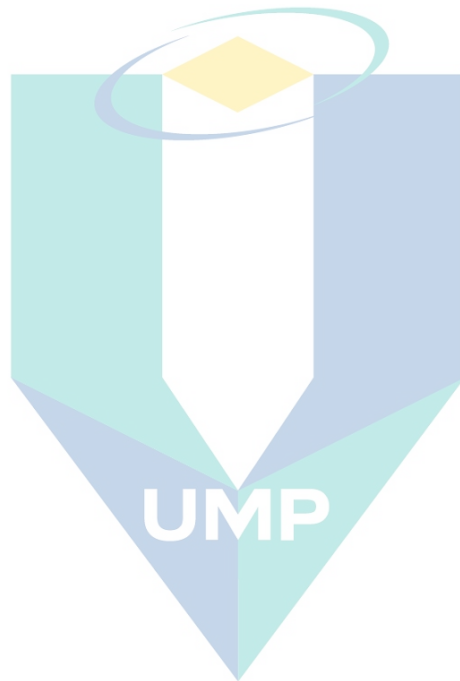
LIST OF ABBREVIATIONS

ANN	Artificial Neural Network
$CSqWC_{sum}$	Sum of Synchrosqueezed wavelet coefficient
CF	Crest Factor
CF_{loc}	Localize crest factor
DC	Duty Cycle
DOP	Depth of Penetration
LK	L-Kurtosis
MAD	Mean absolute deviation
MLPS	Multi-Lag Phase Space
PRR	Pulse Repetition Rate
PO	Pulse Overlap
PW	Pulse duration
PP	Peak power
PSD	Power Spectrum Density
RMS	Root Mean Squares
SPL	Sound Pressure Level

CHAPTER 1

INTRODUCTION

1.1   Introduction

Recently, there are increasing demands for the application of laser welding from numerous clusters of industries. Large industries such as automotive (Hong, K. M. & Shin, Y. C., 2017), oil and gas (Guo, N. et al., 2017), and shipbuilding (Martukanitz, R., 2005) have started to look into the application of laser welding because of its capability in promoting high accuracy, excellent repeatability, versatility and low heat affected zone (Bhadra, R. et al., 2015; Wang, P. et al., 2016). Besides, it is also getting popular due to its ease of use with robots, reduced workforce, full automation, and systematization (Katayama, S., 2013).

In the automotive sector, the laser welding process has been applied to fabricate the Tailor Welded Blank (TWB), as depicted in Figure 1.1. TWB consists of two metal sheets with dissimilar thickness, material, and coating, and it is produced by the laser welding process before it is formed into desired parts via the post-metal forming process (Saunders, F. I. & Wagoner, R. H., 1996). It has been vastly used in the modern-day automotive sector to decrease manufacturing costs, reduce vehicle weight, and improve the strength of automotive body components (Kinsey, B. et al., 2000). Similar to other processes, TWB also has issues relating to weld quality. The existence of defects, such as lack of penetration, misalignment, pin-holes, mis-weld, and sheet deformation is possible in TWB (Vidal, F. et al., 2010). Among these defects, the lack of penetration is quite severe in TWB. A series of studies proved that the existence of incomplete penetration can affect the formability of TWB (Abbasi, M. et al., 2011; Bandyopadhyay, K. et al., 2016). Besides that, it was found that the lack of penetration tended to be a crack initiation point, and could degrade fatigue life (Berto, F. et al., 2016; Boulton, C. F., 1976; Lawrence, F. & Munse, W., 1973; Singh, P. J. et al., 2002).
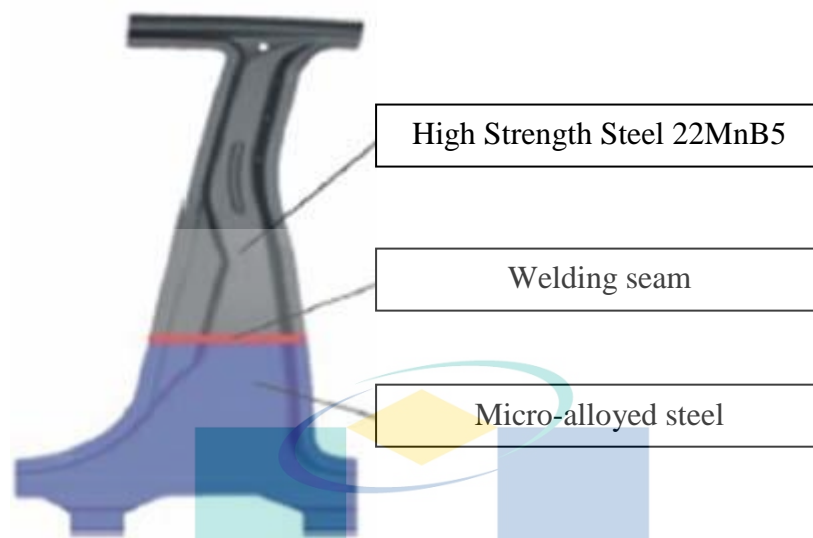
Figure 1.1　　　Tailor Welded Blank for B-Pillar production

Source: Tisza, M., (2013)

Even though optimized process conditions have been applied to obtain pristine weld quality, uncertainties, such as fault in focusing optic, material imperfection, unforeseen contamination, and environmental disturbance can reduce weld quality (Dawes, C., 1992; Lee, S. et al., 2014). Therefore, the development of an in-process monitoring system is believed to be the essential solution to this problem due to its advantages in reducing the amount of reject, improving reproducibility, saving cost, and also enhancing the development of process control system in the future (Purtonen, T. et al., 2014). These are aligned with the needs of Industry 4.0, where an appropriate monitoring system is indicated to be one of the essential criteria to achieve flexible and automated production (Popescu, D. & Amza, C., 2017).

In laser welding, abnormal behaviors of plasma plume, keyhole, and molten metal can lead to information relating to weld penetration condition. Therefore, physical responses in the form of electrical, thermal, optical and acoustic were analyzed in previous works to detect the aforementioned phenomena. In work related to the analysis of electrical signal, the plasma charge voltage signal was found to be significantly correlated with the plasma temperature that emerged from the process. Li

et al., (1996) claimed that the deeper the penetration, the larger the amount of plasma plume liberated. This resulted in higher power absorption and increased plasma temperature.

Apart from electrical signal, other works proved that the thermal signal used is helpful in determining the welding condition. Bertrand et al., (2000) reported that the brightness of temperature profile captured by a pyrometer indicated the drop in laser power, which resulted in the lack of penetration. On the other hand, Gao et al.,(2012) demonstrated the analysis of temperature gradient to evaluate the position of laser beam to avoid misalignment, which could lead to incomplete penetration at certain points along the weld bead.

In the optical method, the light signal emerged from the plasma will be decomposed and analyzed. Besides, this method involves the acquisition and analysis of high-speed digital imaging. Earlier studies demonstrated, phenomena such as molten metal dynamics (Eriksson, I. et al., 2013; Eriksson, I. et al., 2010; Sheng, J. et al., 2017), and plasma intensity (Kong, F. et al., 2012; Sibillano, T. et al., 2012) monitored using these sensors led to the information relating to weld penetration condition.

Other than the previously discussed approaches, acoustic methods have been proven to be able to assess the penetration condition on a real-time basis (Huang, W. & Kovacevic, R., 2009, 2011). There are two types of acoustic signal commonly used for monitoring purposes, which are structure-borne and air-borne acoustic signals, and each signal is captured using different types of sensors.

1.2   Research Overview

There are several approaches for monitoring weld penetration during the laser welding process, namely the electrical, thermal, optical, and acoustic methods. Each method can provide different results. Among these methods, the air-borne acoustic method draws attention from previous researchers owing to some of its unique features, such as high responsible speed, non-contact, and simple sensor setup (Ao, S. et al., 2015; Huang, W. & Kovacevic, R., 2009, 2011; Luo, Z. et al., 2016).

3

Theoretically, the air-borne acoustic waves are generated from sources within an audible frequency range between 20 Hz and 20 kHz. In the laser welding process, these waves originate from the fluctuation of plasma plume ejected from the keyhole. The dynamic pattern of plasma plume results from the interaction between the keyhole and molten metal oscillation (Ao, S. et al., 2015; Farson, D. F. & Kim, K. R., 1999; Hoffman, J. et al., 2002; Szymanski, Z. et al., 2000). Earlier studies proved that the amount of plasma plume is directly related to the laser energy absorption and weld penetration condition (Farson, D. et al., 1998; Lewis, G. & Dixon, R., 1985). Therefore, any instability of plasma plume may affect the behavior of the acquired sound signal and lead to information relating to weld penetration.

In the earlier works, weld penetration condition was accessed from the spectral information of the acoustic signal. Studies reported that amplitude (Duley, W. W. & Mao, Y. L., 1994) and spectral energy (Farson, D. et al., 1996) dropped when insufficient penetration was detected as low amount of plasma plume was produced at that point. Recently, Ao et al., (2015) modeled the spectral behavior of molten metal from different penetration conditions and their model recorded good precision after a comparison of results was made. In studies involving a broader range of laser power and weld speed, the penetration condition was reported to be evaluated up to the case of overheat penetration using the acoustic method. Features, such as root mean square (RMS) (Farson, D. et al., 1998), sum of squared deviation (Gu, H. & Duley, W. W., 1996), and sound pressure deviation (Huang, W. & Kovacevic, R., 2009) were extracted by implying various signal analysis methods. These features were reported to show distinguishable trends according to the penetration categories.

Apart from qualitative evaluation, previous studies proved that quantitative assessment of weld condition can be made via the acoustic method. Huang & Kovacevic, (2011) extracted the sound pressure deviation and bandpower from the acquired signal. The weld penetration estimation model was developed by learning the trend of these features, and the validation result of the model showed good agreement with the experiment.

It could be noticed that reasonable numbers of studies have been made to gain a deep comprehension of the relation between the emitted sound and weld penetration condition. Moreover, some studies investigated the sound characteristics during the presence of other defects in the laser welding process (Ao, S. et al., 2010; Lee, C. J. et al., 2015; Luo, Z. et al., 2016) . Therefore, it can be concluded that the acoustic methods have shown a bright potential to be used in the online monitoring system for the laser welding process. The development of a monitoring system can allow better quality control, and it is one of the essential criteria in modern manufacturing. However, to ensure the robustness of the acoustic methods, many studies are still needed to guarantee that the methods can be extensively used in a wide variation of laser welding process.

1.3   Problem Statement

Based on the research overview, studies related to air-borne acoustic signals for monitoring laser welding covered significant variation in experiment setups and analysis approaches in solving different angles of problems. In order to establish the acoustic methods for industrial applications, there are some problems that lead to the need for extensive studies and it will be the focus of this work.

Based on previous studies, it was found that little attempt was made to understand the emitted sound behavior during pulse mode (PW) laser welding. Most of the recent work focused on the continuous mode (CW) where stationary random-type sound signal emerged from this process (Huang, W. & Kovacevic, R., 2009, 2011; Lee, C. J. et al., 2015; Luo, Z. et al., 2016). PW laser welding promotes other advantages such as low power and more reliable to heat-sensitive component compared to CW process which makes it as one of the popular choice in industry (Assuncao, E. & Williams, S., 2013; Jiang, Z. et al., 2016; Wu, D. J. et al., 2013). Thus, it is important to extend the capabilities of the acoustic method in PW process application. In PW process, a non-stationary random signal will be emitted, which will lead to different challenges in extracting information relating to the weld penetration condition. More to the point, it is vital to understand the characteristics of sound emitted from PW laser welding to relate them with the penetration condition.

Most of the authors agreed that the influence of environmental noise under harsh process surroundings was the main challenge in applying the acoustic methods (Ao, S. et al., 2010; Huang, W. & Kovacevic, R., 2009, 2011). However, there is an insufficient number of literatures that emphasizes the application of signal analysis for noise elimination. Several literature lines were found to demonstrate the application of band-pass filter (Lee, C. J. et al., 2015), spectral subtraction method (Huang, W. & Kovacevic, R., 2009, 2011) and short-time fourier transform (STFT) (Farson, D. et al., 1996) to diminish the noise but these studies were connected to the CW process. In the analysis of transient signals, both spectral-based and STFT methods are often unsatisfactory due to the instantaneous behavior of the signals (Digulescu, A. et al., 2016; Reinhold, I. et al., 2018). Therefore, it is crucial to develop a suitable analysis method for transient signals acquired in the case of PW process. This is important in the attempt to extend the capabilities of the acoustic methods in the laser welding process.

Most of the previous studies highlighted the classification of the acquired sound signals based on the penetration condition. Nevertheless, it will be more noteworthy if the correlation between acoustic sound signal and penetration depth can be modeled. By developing a model based on the sound features, the weld depth can be estimated on an online basis, which is essentially needed in Industry 4.0 (Zhou, K. et al., 2015). In past research, the empirical model for weld penetration estimation from the acquired sound was developed using artificial neural network (ANN) and multiple linear regression (MLR) methods (Huang, W. & Kovacevic, R., 2011). However, this study involved stationary random signals from the CW mode. Hence, the development of a suitable framework is needed in the case of the PW process to enhance the robustness of the acoustic methods.

1.4   Objectives

In order to answer the stated problems, three objectives were established for this study.

a)   To investigate the acoustic signal characteristic from pulse mode laser welding process with different weld parameters level.

6

b)   To develop a signal processing algorithm to eliminate noise and extract sound features associated with the source of information related to the weld penetration status.

c)   To develop the prediction model that that is capable of estimating weld penetration from the acquired sound during the pulse mode (PW) laser welding process.

1.5   Scopes

Basically, in this project, the study will cover the following scopes

a)   A test is run using pulse mode (PW) fiber laser welding with a maximum peak power of 2 kW.

b)   The material under study is ferrous metal. Specifically, the test was conducted on a 22MnB5 Boron steel plate with a thickness of 1.8 mm.

c)   For the weld condition, this study only looks into the depth of penetration condition, as it is also vital to ensure the strength of the weld joined.

d)   Laser peak power and pulse duration were set as independent variables in this study.

e)   Acoustic signals were acquired within the audible frequency range of 20 Hz to 12 800 Hz.

f)   The development of an algorithm in this study involves both sound feature extraction based on time-domain analysis and thresholding method for signal de-noising. Other analysis type such as frequency-based and time-frequency analysis were not considered in this study.

g)   In this study, stepwise regression, which is regression-based feature selection methods, is used to determine the significance of the feature extracted from the developed algorithm. Deep learning feature selection method was not considered in this study.

h)   Prediction models for effective penetration estimation were developed using MLR and ANN methods. Other deep learning methods were not considered in this study.

1.6   Hypothesis

In this study, hypothesis was made by relating the weld parameters, phenomena that occur during laser welding, penetration depth, and behavior of the acquired sound based on previous literature. Based on Figure 1.2, the parameters that were identified to give the main contributions to weld penetration depth are peak power, pulse duration, and focal length.
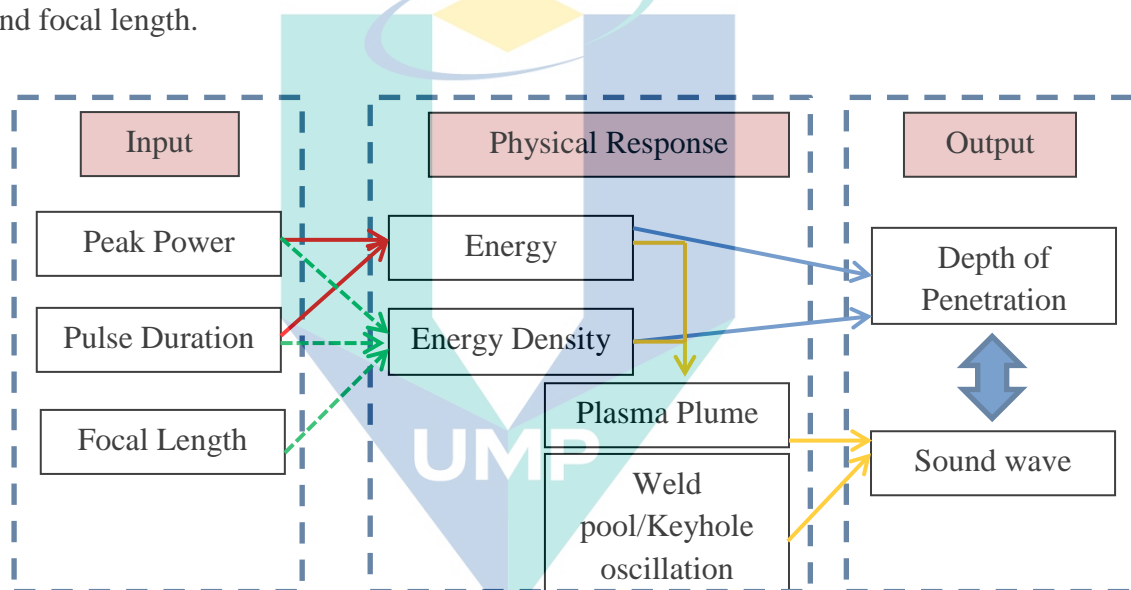
Figure 1.2   Relation between welding parameters with penetration depth and the emerging sound

Previous studies proved that increasing laser peak power and pulse duration resulted in larger laser energy given to the welded material, and deeper penetration. On top of that, the appropriate combination of laser peak power, pulse duration, and focal length will enhance the laser energy density and consequently influence the depth of penetration. Specifically, a larger laser energy will produce more plasma plume, and the pressure from this plasma plume will produce a keyhole shape opening that allows deeper penetration of energy coupling. As energy coupling penetrates deeper, more molten metal is produced from the heating process. A significant amount of plasma plume will be forced to flow out from the keyhole due to the dynamic interaction

between the plasma plume pressure and molten metal oscillation. This particular flow creates the dynamic changes in the air pressure on top of the keyhole opening, which produce sound. Since sound waves will emerge from these phenomena, the hypothesis that can be made is there is a significant relation between the emitted sound wave and penetration depth.

1.7 Thesis Organization

This thesis is composed of five chapters. The first chapter briefly introduces the application of laser welding mainly in the automotive sector. It also emphasizes the importance of the monitoring system due to the endless quality issues. Apart from that, the overview of the related research, problem statement, objectives and scope of study are described. The final part of the chapter explains in detail the hypothesis and focus of the research

The second chapter begins with a deeper explanation on the application of laser welding in the industry, and related physical mechanisms in laser welding process starting from energy coupling to the cooling process. The chapter explains the laser wave mode and all associated weld parameters. It also describes the common defects that occur during the process and the approaches taken for detecting the existence of these defects in previous studies. In this chapter, the source of acoustic signal and studies related to the use of acoustic methods are elaborated in detail.

In Chapter 3, the type of material used in this study and its preparation method are explained. Next, the preliminary experiment method is described and the main results from this experiment are presented to justify the values or range of weld parameters used in this study. The chapter continues with the description of the data acquisition setup, data sampling, and how the macro images of the welded samples were taken. In the next part, the feature extraction method will be explained. The process of developing the signal processing algorithm and empirical model for weld penetration estimation will also be elaborated in detail.

All the results from the experiment and analysis elaborated in Chapter 3 are discussed in Chapter 4. Specifically, Chapter 4 starts with the discussion on the

behavior of sound signal acquired from the PW laser welding process. The trend of features extracted from time-domain, frequency-domain, and time-frequency analyses from the process with different laser peak power levels and laser pulse durations is presented. The performance results of the feature extracted from the developed signal processing algorithm through the feature selection analyses are also discussed in detail. The estimation model developed from both MLR and ANN methods is presented and the results from the validation are discussed at the end of this chapter.

In the closing chapter of this thesis, a summary of the results is presented before the entire work is concluded. At the end of Chapter 5, several recommendations for future work are pointed out.

CHAPTER 2

LITERATURE REVIEW

2.1 Introduction

Over many decades, metal joining has been applied in various industries from large scale such as ship fabrication, gas pipeline networking, automotive assembly, and small scale like electronic component. Under this fact, the technology of metal joining has overgrown, which results in the establishment of various techniques for welding, soldering, and the other type of joining method.

Laser welding has some unique features compared to the other joining method because of its ability to promote good quality welding and reduce the post-machining process (Dawes, C., 1992; Katayama, S., 2018). Due to this fact, it is essential to comprehend the physics of the laser welding process. In this chapter, the physical phenomena behind the process were explained in detail after the general overview of the laser welding is given. Moreover, the wave mode involved in laser welding and how its parameters upbringing the influence to the welding process and quality was discussed. In conjunction with this section, the mechanism of defect formation was pointed out to understand how the combination of parameter sets would enhance the existence of defects. On the other hand, the application of real-time monitoring methods in observing the laser welding process was also described. The next part explained more on the application of the acoustic method due to its interesting features such as low cost, simple and easy setup. In the last part of this chapter, the needs for extensive research in both the laser welding process and the monitoring method were highlighted. Additionally, the main focus of this particular work was described, as well.

2.2 Laser Welding Application in Industries

Recently, laser welding has become more prevalent in the manufacturing process as it has been used in many types of industries. Heavy industries such as automotive (Hong, K. M. & Shin, Y. C., 2017), oil and gas (Guo, N. et al., 2017), and

shipbuilding (Martukanitz, R., 2005) applied this technology due to its advantages such as high accuracy, excellent repeatability, versatility, and low heat affected zone (Bhadra, R. et al., 2015; Wang, P. et al., 2016). As a result, laser welding technology's rapid development could be observed for several decades. Different laser technology offers a different range of wavelength, average power, and any other important parameters that could reflect the physical process during welding, and production cost.

Laser welding technology could be characterized based on its active medium, which functioning as a laser source. These active mediums are categorized as solid-state and gas-state (Dawes, C., 1992). Neodynium yttrium aluminum garnet (NdYAG) and CO_2 are typical examples of solid-state and gas-state active mediums. Commonly, the output power of NdYAG laser welding that available in industry is up to several kW. Even though NdYAG provides lower average power as compared to the CO_2 laser, it could be operated with higher peak powers in pulse mode. Thus, deeper penetration could be obtained from NdYAG laser welding via pulse mode. For this type of laser welding, the output wavelength is around 1.06 micrometers, allowing transmission through fiber optic cables. Unlike NdYAG laser, CO_2 laser welding provides more output power due to low beam quality, resulting in lower laser energy absorptivity. Therefore, to enhance deeper penetration, the output power for CO_2 laser welding could be up to 25 kW, which obviously consumes much energy.

Apart from solid- and gas-state laser sources like NdYAG and CO_2, the use of fiber laser is also becoming popular lately. Unlike the other type of laser, the fiber laser beam is generated in an active fiber optic, which is doped with the rare-earth element and guided to the workpiece by a flexible delivery fiber (Quintino, L. et al., 2007). Besides, a higher degree of laser energy absorption in workpiece due to shorter wavelength have attracted the industry to use this type of laser weld (Kuryntsev, S. V. et al., 2017). Looking back on how this type of laser was developed, fiber laser was invented since the sixties and took several decades of development before it was ready for commercial use (Shi, W. et al., 2014). The first commercially used fiber laser welding only uses a single-mode diode, producing a low power laser beam for the small scale application. Reasoning to the demand for high power laser in a wide variety of industries, an erbium-doped fiber laser was introduced. This invention becomes the groundbreaking finding as the rapid evolution of fiber laser welding technology begins

from this point. By using an erbium-doped fiber laser, a more powerful and precise laser beam could be produced from a single-mode. Accordingly, it became useful for more applications in industries. In modern-day fiber laser technology, further development was done by combining multiple mode pump sources, as shown in Figure 2.1, to achieve greater power (Young, D. & Roychoudhuri, C., 2003). From this point, the introduction of high power fiber laser welding has been dramatically increasing until recently. Unlike its early developed version, the fiber laser welding technology used in industries nowadays could offer some other advantages compared to NdYAG and CO_2 laser. According to Quintino, L. et al., (2007), currently introduced fiber laser welding technology could offer high power, low beam divergence, and flexible beam delivery. Moreover, unlike the other types of laser welding, no alignment is needed for this type of laser, which results in low operating and maintenance costs. Besides that, the good absorptivity of this type of laser beam could promote high electrical efficiency.
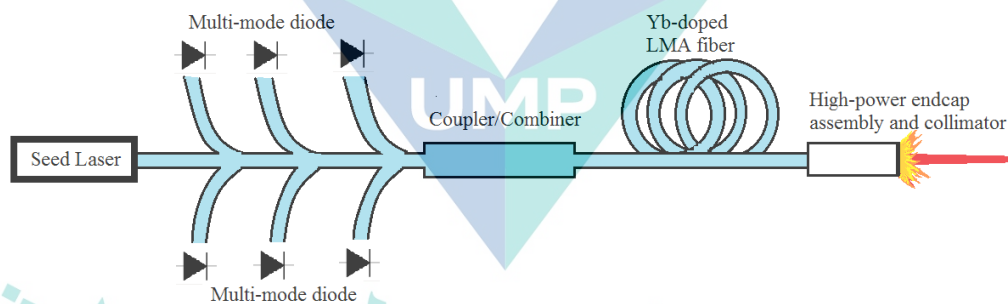
Figure 2.1   Multiple-mode fiber laser.

Source: Young, D. & Roychoudhuri, C., (2003)

In various disciplines of industries, the selection of laser type is explicitly made based on several main factors such as design, productivity as well as production cost. This is to ensure that optimum benefit could be obtained without disregarding the manufacturing cost. In most cases, laser technology with the high power density and high-quality beam are more preferred to satisfy the demand in a wide variety of industries, including micromachining, laser marking, and medical applications (O'Neill, W. et al., 2004). Looking into this factor, fiber laser technologies that are available nowadays seems to promote more advantages as compared to CO_2 or NdYAG laser. With inherent advantages and attractive properties of the latest technology, the

13

uses of fiber laser technology have been expanded into many areas, and its performance will continue to improve (Shi, W. et al., 2014).

2.3   Principle of Laser Welding

Laser welding is inherently different, as the physics behind the process is compared with other welding types. In general, to form a laser weld, the laser beam needs to be focused on the workpiece, and the process afterward involves three major processes, which are coupling, fusion, and cooling.

In the very beginning stage of the laser welding process, the photon in laser beam is either absorbed or reflected from the workpiece surface. For the case of a workpiece with good reflectivity such as metal, majority of photon are reflected from the surface. However, some of the absorbed photon is converted into heat, resulting in increased local temperature. Hence, the absorptivity eventually increased by the local temperature gain. This is because absorptivity of the material could be induced by increasing temperature. As the absorptivity increases, more photons assimilate into the material and accelerate the heating process (Bergström, D., 2008; Kelkar, G., 2008). These whole processes explained the establishment of the coupling phase in the laser welding process. Another factor could enhance coupling, and numerous studies have attempted to explain on this. According to the previous studies, it is found that the surface oxidization (Dausinger, F. & Shen, J., 1993; Nath, A. K. et al., 2002), and increasing surface roughness (Barbarino, S. et al., 1982; Bergström, D., 2008; Bergström, D. et al., 2007) could intensify the absorptivity of the laser beam energy.

(a)

(b)
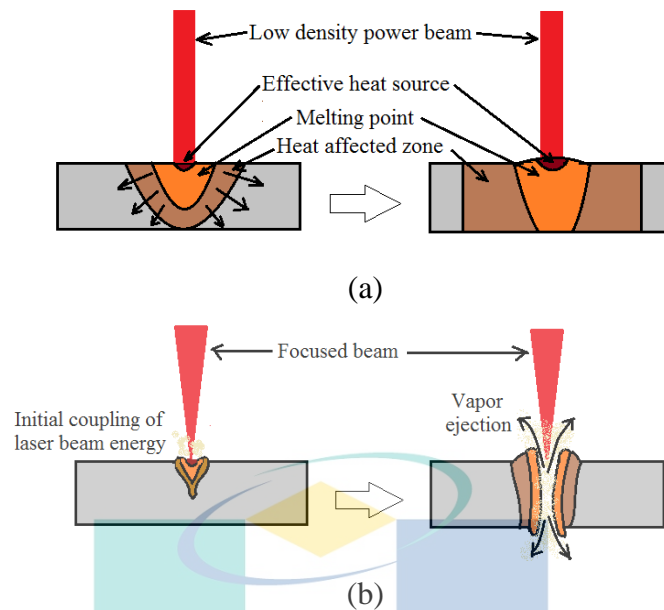
Figure 2.2   Weld geometry for a conduction and keyhole mode welding. (a)
conduction mode (b) keyhole mode

Source: Dawes, C., (1992)

In the next phase, the process of authenticating the fusion zone is involved. This process could be accomplished in two different ways, which is either conduction or keyhole mode. Theoretically, the conduction mode welding occurs when the process is operated with low energy density, whereas heat generated from the coupling process is dispersed underneath the workpiece surface through conduction. When the melting point is achieved, the weld pool occupied by the molten metal is formed. These physical phenomena consequently produce a wide and shallow fusion zone (Dawes, C., 1992; Quintino, L. & Assunção, E., 2013). Nevertheless, the heat-affected zone is also larger in size, as illustrated in Figure 2.2 (a). In contrast, at high beam energy density, the molten metal is forced to move to a weld pool surrounding by the plasma pressure produced from the evaporation of molten metal itself. As a result, a keyhole-shaped cavity is formed. This allows more photon absorption whilst increasing the absorption efficiency (Katayama, S., 2018). Zhang, Y. et al., (2012) in their investigation, have revealed that the distribution of absorbed laser energy inside the keyhole was not uniform. Uniquely, the maximum absorption was found at the keyhole's bottom due to both Friesnel and Inverse Bremsstrahlung absorption during multiple reflections. As a result, the laser beam could penetrate deeper into the workpiece, and due to this

phenomenon, the fusion zone becomes narrow and deeper in shape as illustrated in Figure 2.2 (b).

After fusion stage established, the cooling process took place. In fact, for pulsed laser spot weld, cooling rates are one of the fastest, perhaps second only to resistance spot weld (Kelkar, G., 2008). At this stage, the defect formation is affected upon the cooling rate behavior. Such fast cooling rates can cause many issues, including trapped porosity (Zhou, J. & Tsai, H. L., 2006), high residual stress (Zhang, Y. et al., 2016), cracks (Böllinghaus, T. et al., 2011; von Witzendorff, P. et al., 2015), and excessive weld metal hardness (Malek, G. F. et al., 2007; Sokolov, M. et al., 2011) . However, some of these issues can be alleviated by controlling the cooling rate.

As shown in Figure 2.2, in the progress of establishing the fusion zone, the process could happen either in conduction or keyhole mode (Dawes, C., 1992). In essence, the characteristic of conduction and keyhole mode laser welding is distinctive and identical, giving some of the advantages or drawbacks in different ways. For instance, Quintino, L. & Assunção, E., (2013) has put forward the comparison between those two modes of laser welding. Their review emphasized that in conduction welding, the heat deposited into the material could be easily controlled. Moreover, using a large beam in this mode could reduce the fit-up problem, and high beam quality is not a priority. Besides, fewer defects could be found for conduction mode welding due to the absence of spatter during the process (Assuncao, E. et al., 2012). Meanwhile, shallow penetration and low coupling efficiency are among the disadvantages of using this mode. According to Nath, A. K. et al., (2002), the coupling efficiency is achieved around 15 % only during the conduction mode welding.

On the other hand, in keyhole mode laser welding, high productivity, deep penetration, and small heat-affected zone could be achieved (Ready, J. F. & Farson, D. F., 2001). However, this process is considered unstable due to the weld pool's dynamical behavior and plasma plume itself. This would enhance the formation of defects such as spatters, porosity, undercut, and incomplete penetration (Chen, M. et al., 2017; Pang, S. et al., 2016; Panwisawas, C. et al., 2017; Ready, J. F. & Farson, D. F., 2001).

Even though the difference between conduction and keyhole could be distinguished, the transition region between both modes is still one of the debating topics among scholars. In some studies, the threshold between conduction and keyhole mode welding is determined from power density value. For instance, it was explained that the conduction mode would present if the power density is lower than 10 MW/cm^2 while the opposite mode took place if this value is exceeded (Steen, W. M. & Mazumder, J., 2010). On the other hand, another popular approach in distinguishing the conduction and keyhole mode is by determining the depth-to-width ratio of the weld geometry. According to Nakamura, S. et al., (2000), conduction mode welding occurred when the aspect ratio less than 0.5. In another study, Assuncao et. al., (2012) believed that the other parameter such as welding speed, beam diameter, should not be completely neglected in defining the transition regime. They have also pointed out that previous approaches are assuming that there is a sharp transition between conduction and keyhole mode welding. Hence, in their investigation, it was revealed that the weld character in the transition regime is actually the combination of both modes, and no sharp transition is recorded from their observation. According to the finding, it was reported that the aspect ratio is the suitable parameter to determine the transition due to the result showing that there is a consistent aspect ratio value along with the transition, as illustrated in Figure 2.3. Nonetheless, the exact transition value of aspect ratio depended on the interaction time adjusted by varying the speed during the experiment. This finding was aligned with what has been reported by Chelladurai, A. M. et al., (2015).
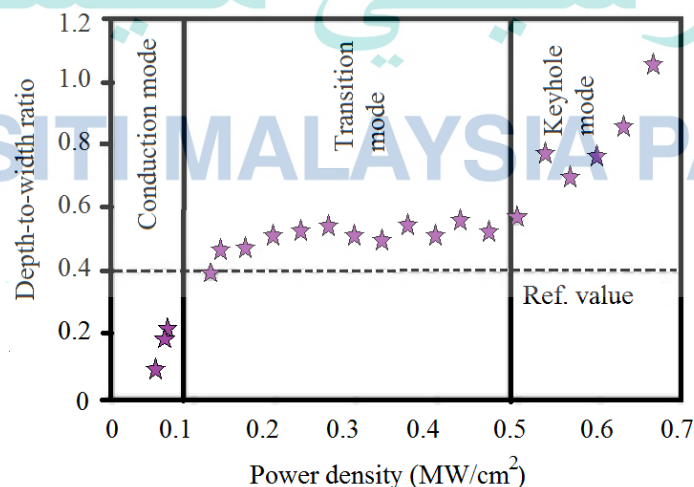
Figure 2.3   Aspect Ratio vs Laser Power Density

Source: Assuncao, E. et al., (2012)

2.4   Wave Mode in Laser Welding

Commonly, laser welding is conducted in continuous wave (CW) or pulse wave (PW) mode. As compared to the other type of welding process, continuous wave mode laser welding is similar to the standard arc welding. On the other hand, the PW mode resembles the resistant spot welding but a bit different because the spot could overlap with each other to obtain hermitic seam (Kelkar, G., 2008). In contrast to CW mode welding, pulse energy, pulse duration, duty cycle, pulse repetition rate, and pulse overlap are some of the additional parameters that commonly considered in PW mode laser welding alongside with the weld speed, average power, power density and the focal length (Yaakob, K. et al., 2017).

Figure 2.4 illustrates specific parameters involved in pulse wave mode (Miyachi, A., 2017). According to the figure, peak power, P_{pk} could be defined as the highest power whilst the pulse duration, t_p is the exposed time in a single pulse. Meanwhile, the pulse energy, E, could be determined by the giving equation (Chelladurai, A. M. et al., 2015).

$$E = P_{pk} \text{ x } t_p \qquad\qquad 2.1$$
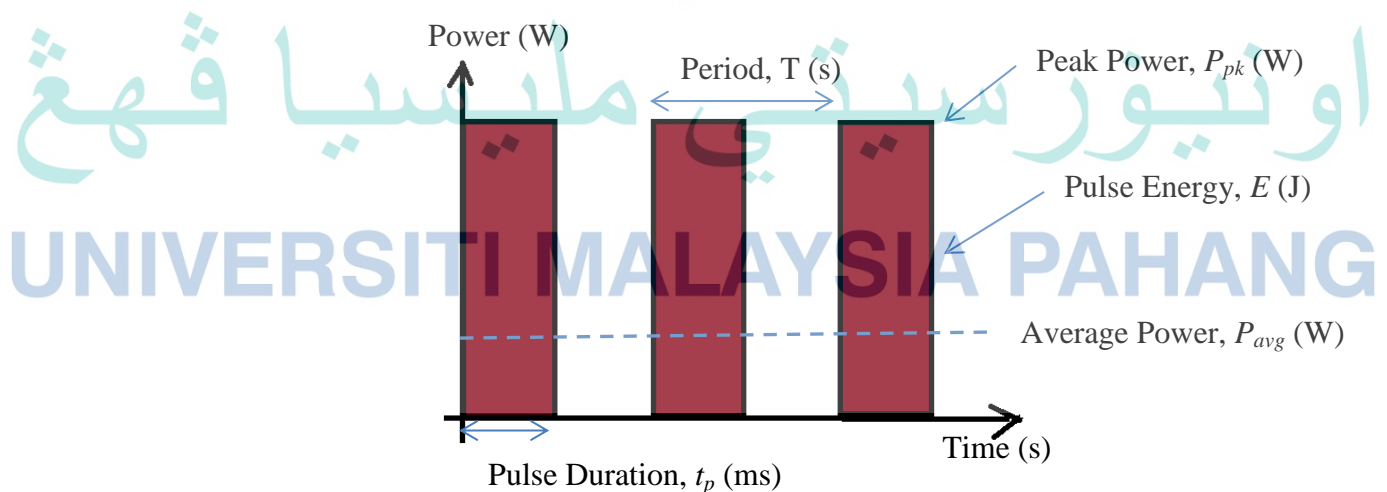
Figure 2.4   Parameters in pulse-mode laser welding
Source: Miyachi, A.,(2017)

The shaded area in Figure 2.4 represents pulse energy. For the case of multiple pulses, the average power, P_{avg}, is obtained from the product of pulse energy, E, and pulse repetition rate, PRR, as shown by equation 2.2 (Miyachi, A., 2017).

$$P_{avg} = E \text{ x } PRR \qquad\qquad 2.2$$

where the pulse repetition rate, PRR represent the amount of pulse given each seconds.

$$PRR = \frac{1}{T} \qquad\qquad 2.3$$

Beside all these parameters, other essential parameters that need to be considered in pulse wave mode are the duty cycle, DC, and pulse overlap, PO, which could be calculated by using equation 2.4 and 2.5 respectively (Yaakob, K. et al., 2017).

$$DC = PRR \text{ x } t_p \qquad\qquad 2.4$$

$$PO = 1 - \left(\frac{v_w}{d_s \text{ X } PRR} \right) \qquad\qquad 2.5$$

Theoretically, the duty cycle, DC, is the ratio between the pulse duration, t_p, and the total period, T, for one complete cycle. Meanwhile, the pulse overlap, PO, is the percentage of overlapping along the seam whereas v_w and d_s in equation 2.5 represent the weld speed and spot diameter respectively.

On the other hand, CW mode laser welding is usually operated by controlling the speed and power. Nevertheless, other common parameters that would affect the weld geometry and quality for both type of wave mode are beam diameter and interaction time. Beam diameter is an important measure because it could influence the beam power density given to the workpiece. Basically, the power density, PD, could be determined by equation 2.6, whereas d_b in this equation is the diameter of the laser beam at the weld spot (Assuncao, E. & Williams, S., 2013).

$$PD = \frac{P}{\pi d_b^2} \qquad\qquad 2.6$$

As compared to the CW mode, PW mode emerged the difference in the process nature and involving more parameters. Both types are widely used in industries for various applications. However, the specific reason for the selection of different type of laser emission is yet unclear among both scholars and industries (Caprio, L. et al., 2018). Comparing both types, PW mode seems to be advantageous if the average power is the only thing that is considered. By using PW mode, high average power laser machines are unnecessary (Dawes, C., 1992). If compared both processes under the same condition, Assuncao, E. & Williams, S., (2013), reported that PW process gives same penetration at lower laser density as compared to CW process as shown in Figure 2.5. This finding suggested that PW process gives higher penetration efficiency as only low heat input was needed to achieved same penetration with CW process. This advantage results in low distortion on the welded joint as well as giving more chances to weld heat-sensitive components (Assuncao, E. & Williams, S., 2013; Frewin, M. R. & Scott, D. A., 1999; Liu, J. T. et al., 1993; Weckman, D. C. et al., 1997; Wu, D. J. et al., 2013). However, reaching the process stability in PW welding is quite difficult, as numerous parameters need to be considered. This attracted the scholars to study more in-depth on PW weld and how it could overcome the drawback from CW mode weld (Assuncao, E. & Williams, S., 2013; Jiang, Z. et al., 2016; Kuo, T. Y., 2005).
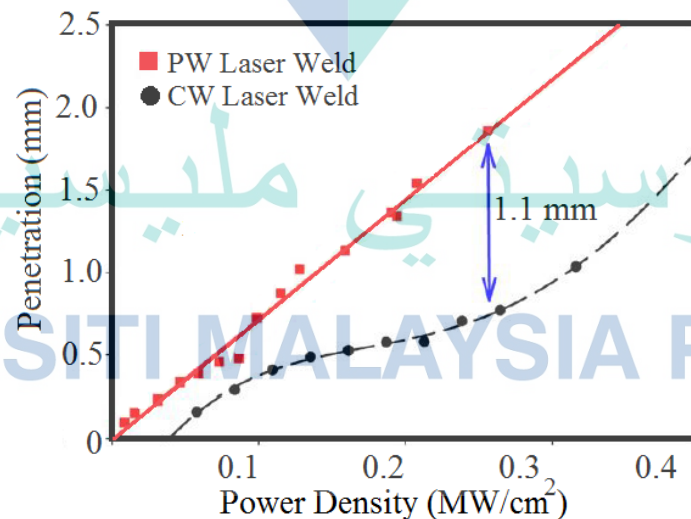
Figure 2.5   Comparison between PW and CW process under the same interaction time and beam size

Source: Assuncao, E. and Williams, S., (2013)

2.5 Defect Formation during Laser Welding Process

The previous section clearly shows that the laser welding process involves various parameters, especially in PW mode. Due to this reason, reaching process stability is one of the major challenges. Obtaining the process stability is essential to avoid the formation of a defect and get the desired weld quality. Generally, if the instability occurs during the laser welding process, both geometrical imperfection and sub-surface defects could exist. Moreover, the laser machine consistency and environmental disturbance could also contribute to defects formation. As a result, it would also affect the physical or mechanical properties of the welded parts. Therefore, it is crucial to understand deeper into the mechanism of defect formation before selecting parameters for the process. In this section, the formation welding imperfection and it's effect was discussed.

2.5.1 Geometrical Imperfection

Commonly in industries, the product is fabricated by the series of metal forming and machining. Likewise, in some fabrication involving laser welding, the post-machining process is necessary until the complete product is finished. Hence, avoiding geometrical imperfection such as distortion, burn through, underfill, humping, and undercut is truly important. This is because any of these geometrical imperfections tend to affect the mechanical properties of the product in later stage of machining process.

2.5.1.1 Weld Distortion

For product fabrication that involves stamping after the welding process, weld distortion is one of the major issues. Weld distortion would appear when there is a large difference between the top and the bottom width of the weld pool. As a result, uneven thermal expansions occur at the upper and lower part of the workpiece, which consequently bends it (Carrolo, V. S., 2010), as illustrated in Figure 2.6. Apart from weld pool geometry, uneven residual stress that emerged from the welding process also contributes to distortion formation (Moraitis, G. A. & Labeas, G. N., 2009), Moreover, this type of defect could also exist in case of high thermal expansion coefficient and low thickness material (Katayama, S., 2013).
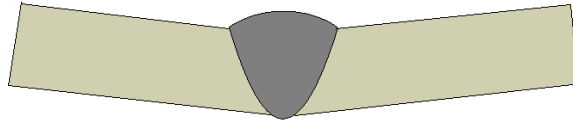
Figure 2.6   Distortion of the welded thin plate.

Source: Carrolo, V. S.,(2010)

Because of the quality problem that emerged from the distorted welded product, some alternatives have been suggested to overcome this problem. Appropriate clamping method (Katayama, S., 2013), pre-bending process (Carrolo, V. S., 2010), and rapid cooling (Zhang, Y. et al., 2016) were the proposed method in the previous research. Uniquely, the application of this methods were proven to reduce the amount of distortion.

2.5.1.2   Burn through

Apart from distortion, another critical defect that would affect the post-weld quality is burn-through. As shown in Figure 2.7, Burn-through exists when melt in a molten pool is dropped down during the welding process to form underfill bead with a concave top and convex bottom surface. This is happen due to excessive plasma pressure as a result from high heat input (Akman, E. et al., 2009; Luo, Z. et al., 2016). Commonly, this defect tends to exist when the process involves full penetration welding with a wide bottom surface of the weld pool with high heat input (Katayama, S., 2013). Avoiding burn through defect is highly important because this defect could degrade the strength of the welded joint (Abbasi, Z. et al., 2018). However, it's visibility degree is making it easy to be visually detected, which allows the rejection before the next machining process. Process parameters optimization has been reported as one of the solution to suppress this kind of defect (Dawes, C., 1992; Katayama, S., 2013; Liu, L. et al., 2018).
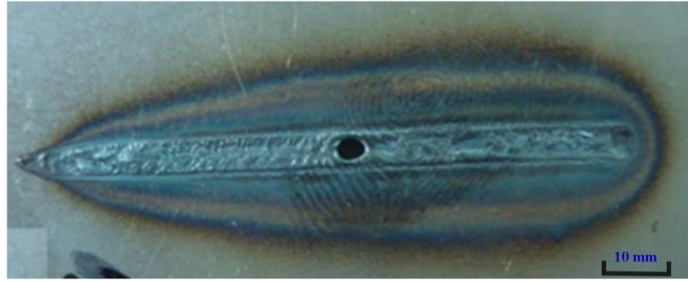
Figure 2.7   Burn through defect

Source : Luo, Z. et al.,(2016)

2.5.1.3   Underfill

Underfill could be described as incomplete penetration on the top surface of the fusion zone, and this is drawn in Figure 2.8. This type of defect takes place mainly due to the severe spattering of melts during the laser welding process (Kawahito, Y. et al., 2009; Wahba, M. et al., 2010). Based on the previous studies, the existence of low boiling temperature element (Kaplan, A. F. H. & Powell, J., 2011), keyhole instabilities (Chang, B. et al., 2016; Kawahito, Y. et al., 2015; Volpp, J., 2017; Zhang, M. J. et al., 2013), and excessive metal evaporation (Li, S. C. et al., 2014) were among the factors leading to the large amount of spatter. To tackle this issue, finding the optimized parameter is important in which the power needs to be reduced without disregarding the other factor, especially the desired penetration (Heider, A. et al., 2015; Li, S. C. et al., 2014; Matsunawa, A. et al., 1992).

Figure 2.8   Underfill defect

Source: Huang, W. & Kovacevic, R.,(2011)

2.5.1.4   Undercut

A bit different from the underfill, the undercut could be described as a groove along the toe of the weld bead (Figure 2.9). It is likely to occur due to high power and high pressure of an assisted gas (Dawes, C., 1992). On the other hand, the undercut formation might as well occurred from the process with low welding speed (Frostevarg, J. & Kaplan, A. F. H., 2014). Basically, with slower welding speed, non-uniform cooling process could form pre-solidified material at the gouge rim. In case of butt joint, an excessive gap could result in improper melt flow, and the gouge is too far to be filled completely leading to the undercut formation. Since inappropriate parameter condition has contributed to undercut formation, the optimization of welding condition is needed as a measure to overcome this problem (Katayama, S., 2013).
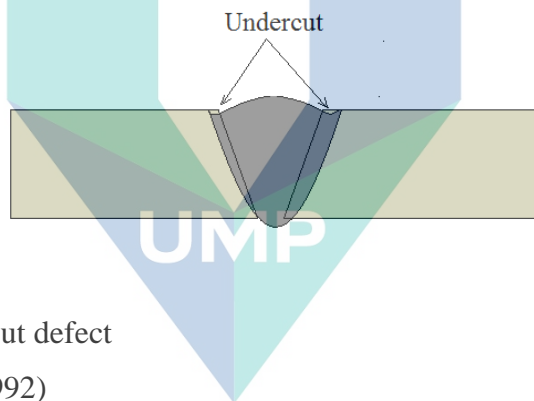
Figure 2.9   Undercut defect
Source: Dawes, C.,(1992)

2.5.1.5   Humping

Unlike another type of geometrical imperfection, humping is formed due to the backward flow of melt due to the ejection of plasma plume and high surface tension of accumulated melt due to narrow molten pool width (Gratzke, U. et al., 1992). The narrow molten pool may occur due to small focused beam during high weld speed (Amara, E. H. & Fabbro, R., 2010; Thomy, C. et al., 2008). Consequently, a hump-shaped weld bead is formed on top of weld bead, as shown in Figure 2.10. The occurrence of humping might be suppressed under a defocused condition (Kawahito, Y. et al., 2009). Moreover, by shifting from partial to full penetration, the ejection of melt in upward direction might reduce, which lessens the tendency of humping to form (Katayama, S., 2013).

24
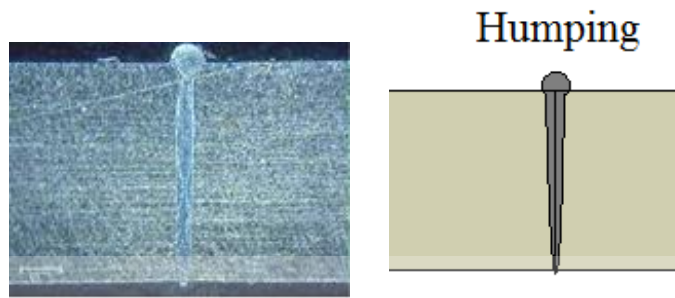
Figure 2.10   Humping Defect

Source: Gratzke, U. et al., (1992)

2.5.2   Sub-surface Defect

Another major problem associated with the welding quality is the formation of sub-surface defects such as incomplete penetration, crack, and porosity. These defects are more severe than the other geometrical imperfection due to the difficulties in detecting it. Detecting sub-surface defects could be done through a nondestructive testing method such as X-ray radiography, ultrasound, and acoustic emission. However, they were costly, time-consuming, and need a certified practitioner to run the test and interpret the data.

2.5.2.1   Incomplete Penetration

One of the common internal defects that possibly occurred from the laser welding process is incomplete penetration. As illustrated in Figure 2.11, this type of defect existed when the process of laser energy coupling is not desirably completed, which causing the fusion zone not reach the bottom of the workpiece. This might degrade the strength of the welded joint, and conceivably happen due to several factors. Based on the previous studies associates with the process optimization in pulse mode laser welding (Assuncao, E. & Williams, S., 2013; Assuncao, E. et al., 2012; Nath, A. K. et al., 2002; Ready, J. F. & Farson, D. F., 2001), weld penetration was reported to be closely related to several parameters, but it is mainly affected from the focal position, laser peak power, and pulse duration. This is due to the fact that the laser energy coupling process is depending on the amount of laser energy as well as its absorptivity (Bergström, D., 2008; Bergström, D. et al., 2007; Kelkar, G., 2008).

Conceptually, by controlling the above-mentioned parameters, the incomplete penetration in pulse mode laser welding are simply could be addressed. However, the occurrence of these types of defects remains an issue until now. Even though the process have been carry out with the optimal parameter set, the faulty on the focusing optic might certainly cause a sudden drop in laser power, which subsequently results in the sudden loss of weld penetration. On the other hand, the dynamic of the plasma cloud that emerged along the process might causing the fluctuation of energy absorption, and sudden shallow penetration might appear accordingly (Dawes, C., 1992).

Figure 2.11   Incomplete Penetration

Source: Huang, W. & Kovacevic, R., (2009)

2.5.2.2   Crack

In laser welding process, crack formation can be categorized into hot and cold crack. Hot cracking presence at the weld fusion and heat-affected zone. In establishing solidification process, certain alloy forms a brittle incomplete solidified mass until it cooled into lower temperatures. This brittle liquid film is present surround the grains or dendrite. When it is subjected to high transverse contraction stress, solidification cracking might be introduced in the film boundaries as shown in Figure 2.12. In steel, elements such as sulphur, phosphorus, and boron could induce solidification cracking (Dawes, C., 1992).

In particular, the tendency of the occurrence of solidification cracking is larger for the case of PW laser welding (Katayama, S., 2013; Kelkar, G., 2008) or high-speed welding with CW laser (Katayama, S., 2013). Several studies show that there is an

26

alternative to suppress the formation of this defect. According to the previous studies, optimum weld speed (Kadoi, K. et al., 2013), cooling time (Kelkar, G., 2008; Yan, F. et al., 2017), and pulse shape control (von Witzendorff, P. et al., 2015) were proven to be significant in reducing the critical strain which could initiate the solidification crack.

On the other hand, the formation of cold cracking took place when there is hydrogen accumulated in the highly stress-concentrated zone (Stout, R. D. & Doty, W. D., 1971). The crack usually forms in the heat-affected zone in the post-weld phase, but it could also occur in the fusion zone (Dawes, C., 1992). In addition, it occurs in a shorter period under conditions of higher hydrogen content, higher restraint stress, and higher hardness of the weld (Katayama, S., 2013).

Figure 2.12   Solidification crack
Source: Yan, F. et al., (2017)

2.5.2.3   Porosity

Apart from hot and cold cracking, another type of defect underneath the fusion zone is porosity. Porosity takes place when there are trapped bubbles during the solidification phase (Dawes, C., 1992). These bubbles were originated from vapor and ambient gas at both the rear side and tip of the keyhole. It were trapped upon the accomplishment of the solidification process as a result from slow back-filling speed (Berger, P. et al., 2011). Meanwhile, inappropriate solidification rate or backfilling speed are initiate from the instability of keyhole or molten metal (Chen, M. et al., 2017; Li, K. et al., 2015; Meng, W. et al., 2014; Pang, S. et al., 2016; Pastor, M. et al., 1999; Zhou, J. & Tsai, H. L., 2006). In attempts to reduce the formation of porosity, several approaches have been taken in the previous research. Generally, optimization of weld speed, defocusing value, peak power was proven to be significant in reducing the

occurrence of porosity (Li, K. et al., 2015). In case of PW welding, it have been reported that the porosity could be suppressed almost completely when the overlapping factor reaches 75% (Gao, X. L. et al., 2014). Meanwhile, in case of lap joint, the amount of porosity could be reduced by optimizing the gap between the upper and lower plate to be joined (Meng, W. et al., 2014). The gap and root porosities were shown in Figure 2.13.
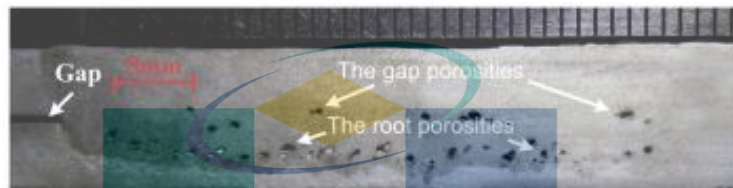
Figure 2.13   Porosity
Source: Meng, W. et al., (2014)

Table 2.1 shows the summary of the defects formation sources of all types of defects discussed in 2.5.1 and 2.5.2. According to the table, it is clear that the welding defects emerge from numerous physical sources that were initiated from improper welding design, material selection, and parameter combination. In the previously discussed topic, optimizing the welding condition by finding a suitable combination of parameters seems to be a feasible solution to this problem. However, quality assurance is still could not be fully guaranteed because the defects might still occur from ambient factors such as machine instability and faulty.

In TWB production, all types of defects discussed in Section 2.5 are commonly existed (Vidal, F. et al., 2010). The occurrence of these defects could degrade the strength of the welded joint which makes it important to be controlled during the process. Comparing between two different categories of defect in section 2.5.1 and 2.5.2, sub-surface defects are more severe as it is not easy to be detected. In previous studies, non-destructive testing has been demonstrated to be useful to detect sub-surface defect (Chengning, Z. et al., 2010; Montgomery, A. et al., 2003). However, the suitability and sensitivity of these option is subjective (Li, M. M., 2011).

28

Table 2.1   Summary on the defect formation sources.

Defect	Physical source of defect	Parameter that influence the source of defect	References
Distortion	Inappropriate size of weld pool dimension Uneven residual stress	Groove design Laser power/energy Workpiece thickness	(Carrolo, V. S., 2010; Katayama, S., 2013; Moraitis, G. A. & Labeas, G. N., 2009; Zhang, Y. et al., 2016)
Underfill	Excessive spattering Molten pool and keyhole instability	Laser Power/energy Gap size (In case of lap joint) Material (with low boiling temperature element)	(Chang, B. et al., 2016; Heider, A. et al., 2015; Kaplan, A. F. H. & Powell, J., 2011; Kawahito, Y. et al., 2009; Li, S. C. et al., 2014; Matsunawa, A. et al., 1992; Nakamura, S. et al., 2000; Volpp, J., 2017; Wahba, M. et al., 2010; Zhang, M. J. et al., 2013)
Undercut	Non-uniform cooling High pressure of assisted gas	Welding speed Shielding Gas Gap size (In case of lap joint)	(Dawes, C., 1992; Frostevarg, J. & Kaplan, A. F. H., 2014; Katayama, S., 2013)
Humping	Backward flow of melt Ejection of melt from plasma plume pressure Narrow keyhole size	Focal length Laser power/energy	(Amara, E. H. & Fabbro, R., 2010; Gratzke, U. et al., 1992; Katayama, S., 2013; Kawahito, Y. et al., 2009; Thomy, C. et al., 2008)
Incomplete penetration	Laser energy coupling Dynamic of plasma cloud	Focal position Laser power Pulse duration (in case of pulse mode) Weld speed	(Assuncao, E. & Williams, S., 2013; Assuncao, E. et al., 2012; Bergström, D., 2008; Bergström, D. et al., 2007; Kelkar, G., 2008; Nath, A. K. et al., 2002; Ready, J. F. & Farson, D. F., 2001)
Crack	Improper solidification	Welding Speed Pulse repetition rate (in case of pulse mode)	(Dawes, C., 1992; Kadoi, K. et al., 2013; Katayama, S., 2013; Kelkar, G., 2008; von Witzendorff, P. et al., 2015; Yan, F. et al., 2017)
Porosity	Rapid solidification Improper backfilling speed Gas trapped	Weld speed Pulse repetition rate	(Berger, P. et al., 2011; Chen, M. et al., 2017; Dawes, C., 1992; Gao, X. L. et al., 2014; Li, K. et al., 2015; Meng, W. et al., 2014; Pang, S. et al., 2016; Pastor, M. et al., 1999; Zhou, J. & Tsai, H. L., 2006)

Among the described subsurface defect, incomplete penetration is one of the defects that need to be controlled in TWB production. Li, M. M., (2011) pointed out that incomplete penetration have better chance to be detected by using ultrasound and eddy current method. However it is difficult to discover when the depth is less than 0.1 mm. Previous study revealed that the existence of incomplete penetration caused the reduction in weld geometry and simultaneously affect the strength of the welded joined

(Bandyopadhyay, K. et al., 2016). Another study showed that the dome height which represented as the degree of formability was reduced as the incomplete penetration existed. This was clearly shown in Figure 2.14 whereas the fracture was found initiated at the weld zone (Abbasi, M. et al., 2011).
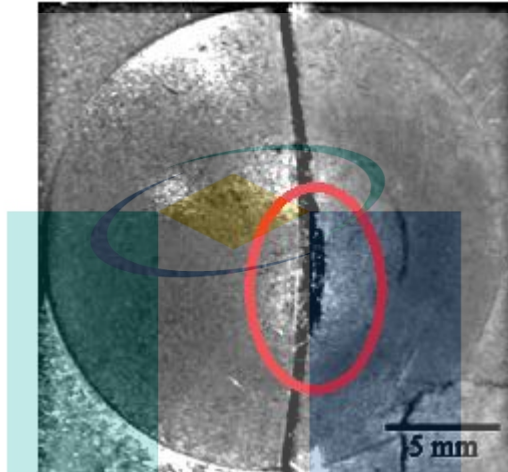
Figure 2.14   Fracture from weld line due to incomplete penetration during metal forming process

Source: Abbasi, M. et al., (2011)

Apart from formability issue, the existence of incomplete penetration is also being concerned due to its ability to turn into a crack tip and speed up the fatigue failure (Berto, F. et al., 2016). In earlier work by Boulton, C. F., (1976), the fatigue life of the welded joint with incomplete penetration was estimated by developing the mathematical model. This study revealed that the toe size and the location of the incomplete penetration play an important role to the fatigue life. Similar finding also have been reported by Singh, P. J. et al., (2002).

2.6   Monitoring the Laser Welding Process

The mechanisms of defect formation have been described in section 2.5. Among the suggested solution to reduce these defects, identifying the optimum welding parameters seem to be one of the popular solution. However, despite the right practical steps, quality assurance still becomes a major issue for several reasons. As example, a fault occurring in the focusing optic like thermal distortion and cracked lens would

distort the focus spot, consequently changing the power density (Dawes, C., 1992). Furthermore, material imperfection and unforeseen contamination would also reduce the absorptivity of laser beam energy. From another angle of view, other scholar pointed out that the occurrence of defects might also happen when the process responding in non-linear way even though the optimum parameters have been set out (Lee, S. et al., 2014). Considering this factor, it is difficult to rely only on parameter optimization to overcome the weld quality problems. Hence, the feasible solution for this drawback is to develop an in-process monitoring system. Process monitoring is the essential way to reduce the amount of reject, improve reproducibility, and save cost. Furthermore, it could also enhance the development of the process control system in the future (Purtonen, T. et al., 2014).

During the laser welding process, many physical responses in the form of electrical, thermal, optical, and acoustic were dynamically emerged from the laser-material interaction. Due to this reason, monitoring the laser welding process is commonly done by capturing the information concerning to these responses. For instance, previous work related to the electrical signal demonstrated that the analysis of a plasma potential signal significantly aided in monitoring laser weld quality. This is because the emitted plasma potential signal contains the information related to the size and behavior of plasma plume in which it could be correlated with the penetration status and other types of defects (Li, L. et al., 1996). As illustrated in Figure 2.15, measuring the plasma potential in the vicinity between the weld nozzle and workpiece could be done using a plasma charge sensor (You, D. Y. et al., 2014).
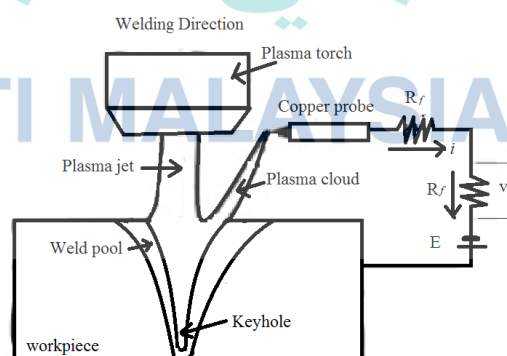
Figure 2.15   Schematic diagram of plasma charge sensor
Source: You, D. Y. et al., (2014)

Apart from the electrical signal, the use of thermal signal is also helpful in evaluating the welding condition. By utilizing probes such as pyrometer and infrared camera, the temperature trends during the cooling process could be monitored. Bertrand, P. et al., (2000) have demonstrated the use of a pyrometer to monitor the surface temperature during CW laser welding. It was reported that the signal from different wavelengths acquired by pyrometer shows a trend according to the solidification stage. Moreover, the drop in laser power, presence of contamination, and lack of shielding gas could be detected by brightness temperature from a particular wavelength. This could be referred in Figure 2.16. In another study, (Gao, X. et al., (2012) used the infrared camera to extract the thermal distribution of the molten metal during the process. As a result, this parameter could be used to determine the deviation between the laser beam focus and weld seam center, which significantly helped control the process.

(a)　　　　　　　　　　　　　　(b)

(c)
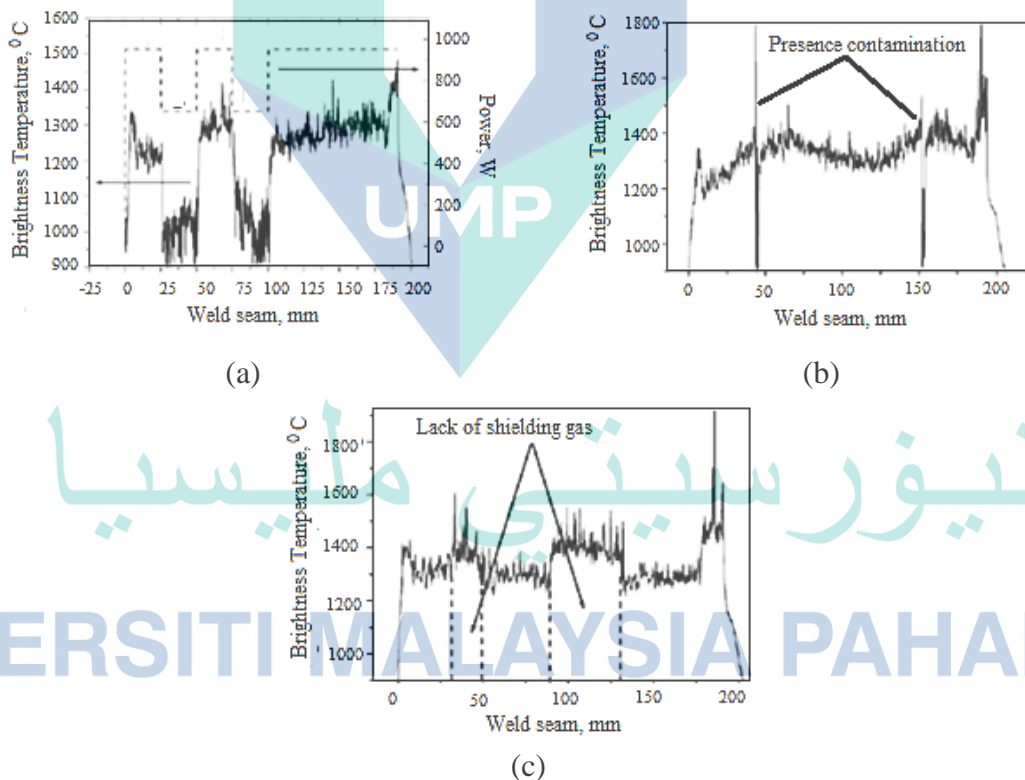
Figure 2.16   Brightness temperature reading acquired from pyrometer with respect to the variation of (a) Laser power (b) presence contamination (c) shielding gas.
Source: Bertrand, P. et al., (2000)

By the fact that the laser-material interaction produces a large amount of light, the spectrometer application for monitoring purposes has also been established.

Basically, spectroscopic analysis is carried out by acquiring the light emission from the plasma, and the characteristic of this signal has been proved to show good agreement with the welding condition. For example, in the previous work, Kong, F. et al., (2012) revealed that the zinc vapor originated from the workpiece coating could be detected from the spectroscopy analysis. According to their result in Figure 2.17, the plasma intensity above the weld pool seems to be reduced when there is zinc coating on the workpiece surface. In another part of their study, the increase in weld speed was found to cause a drop in plasma intensity value because the increasing speed would reduce the interaction time, which consequently caused a lack of plasma plume formation. This have leading to the information related to the penetration condition (Sibillano, T. et al., 2012). Apart from penetration condition, defect such as porosity (Zhang, Z., Kannatey-Asibu, E., et al., 2015), and local thickness reduction (Sebestova, H. et al., 2012) were previously detected from spectroscopic analysis.

(a)   (b)
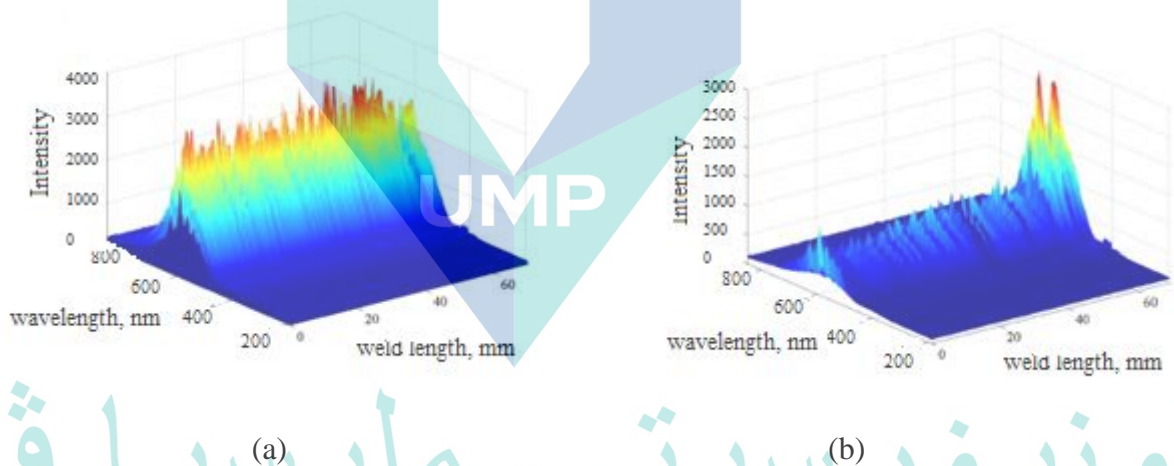
Figure 2.17   Spectrum of laser-induced plasma captured by spectroscopy of lap-jointed galvanized steel with a speed of 30 mm/s (a) without zinc coating (b) with zinc coating

Source : Kong, F. et al., (2012)

In another approach, the use of acoustic signals has also been demonstrated to monitor the laser welding process. Theoretically, the acoustic signal emitted from the laser welding process lies within 20 Hz to several MHz, propagating through air or structure. Many research shows that this method was capable of detecting defect such as burn through (Ao, S. et al., 2010; Luo, Z. et al., 2016), humping (Lee, C. J. et al., 2015), and porosity (Gu, H. & Duley, W. W., 1996; Sun, A. et al., 2001). Furthermore,

33

instability in weld pool oscillation (Ao, S. et al., 2015) and the dynamic of plasma plume (Farson, D. F. & Kim, K. R., 1999) have also been studied using this approach.

Table 2.2   Summary of four major categories of laser welding process monitoring methods

Signal Type	Sensor	Commonly detected phenomena	References
Electrical	Plasma Charged Sensor	Plasma Plume Size	(Li, L. et al., 1996; You, D. Y. et al., 2014)
Thermal	Pyrometer Thermal Camera	Cooling trend Thermal Distribution	(Bertrand, P. et al., 2000; Gao, X. et al., 2012)
Optical	Spectrometer	Plasma intensity Weld pool dynamic Keyhole oscillation	(Kong, F. et al., 2012; Sebestova, H. et al., 2012; Sibillano, T. et al., 2012; Zhang, Z., Kannatey-Asibu, E., et al., 2015)
Acoustic	Microphone Acoustic Emission Sensor	Plasma plume dynamic Weld pool dynamic Keyhole oscillation Phase transformation	(Ao, S. et al., 2010; Farson, D. F. & Kim, K. R., 1999; Gu, H. & Duley, W. W., 1996; Lee, C. J. et al., 2015; Luo, Z. et al., 2016; Sun, A. et al., 2001)

Based on four major categories of monitoring method summarized in Table 2.2, it was clear that different method have its own ability to monitor different phenomena during the laser welding process. However, there are plenty of options for monitoring phenomena such as plasma plume, weld pool, and keyhole dynamic which could lead to the significant information related to the penetration condition. Comparing between the options lead to the subjective answer as each method promotes their advantages in different ways. However, the use of microphone grasp attention by the researchers lately due to its high responsible speed, non-contact, and simple sensor setup features (Ao, S. et al., 2015; Huang, W. & Kovacevic, R., 2011; Luo, Z. et al., 2016).

2.7   Signal Analysis of the Acquired Sound

Based on the explanation in Section 2.6, it was learned that in any method, signal was acquired and analyse to investigate its correlation with weld condition. In work involving the single-dimensional data or signal, the analysis was done by extracting the signal features. In some works related to the acoustic method application, the filtering methods have been implemented to enhance the trend of the extracted features (Duley, W. W. & Mao, Y. L., 1994; Huang, W. & Kovacevic, R., 2009, 2011;

Lee, C. J. et al., 2015). Meanwhile, many studies implement direct feature extraction analysis (Ao, S. et al., 2010; Farson, D. et al., 1998; Farson, D. F. et al., 1999; Gu, H. & Duley, W. W., 1996; Sun, A. et al., 2001). The trend of these features was learned or analyzed in order to develop the predictive model which can be used to predict the weld condition. As shown in Figure 2.18, prediction model can be categorized into two sub-areas which are regression and pattern classification. According to Fahrmeir, L. et al., (2013), regression model is the type model which is able to make a prediction on continuous variable. In other word, this type of model offers a quantitative estimation of the measurable weld condition such as the size of porosity, crack length, and the depth of penetration. On the other hand, pattern classification is the approach where the weld conditions were evaluated qualitatively (García-Laencina, P. J. et al., 2010).
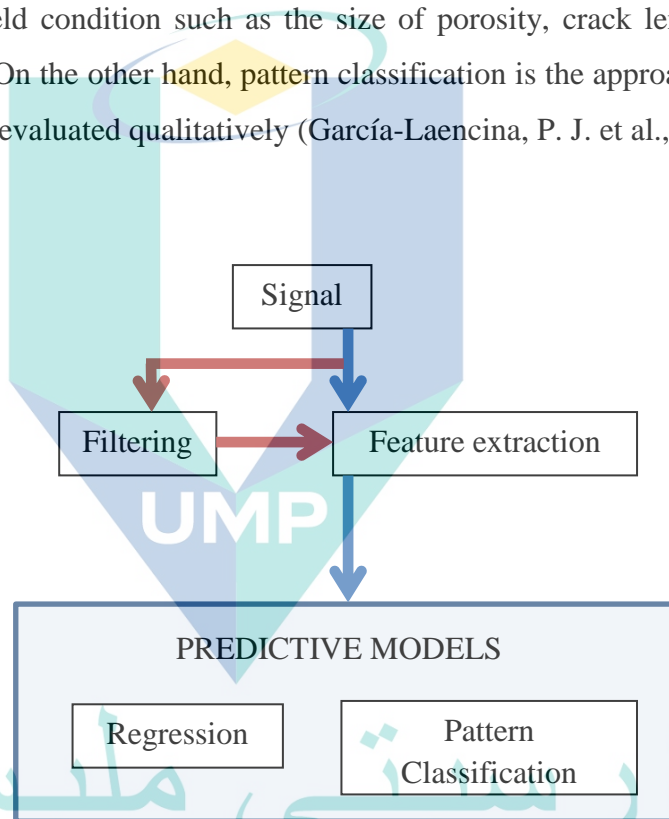
Figure 2.18   Analysis of the acquired signal for welding process monitoring

2.7.1   Common type of signal acquired from sensors

Before giving further explanation on the signal analysis, it is also essential to know the general type of signals. As depicted in Figure 2.19, two major types of signals are the periodic and random signals. For a periodic signal, the characteristic of several features such as peak amplitude and cycle period is periodically constant. Additionally, this type of signal could be formed from a single- or multi-frequency. In contrast, the

random-type signal typically appeared in a random pattern. It is a combination of an infinite number of periodic signals with different amplitudes and frequencies.
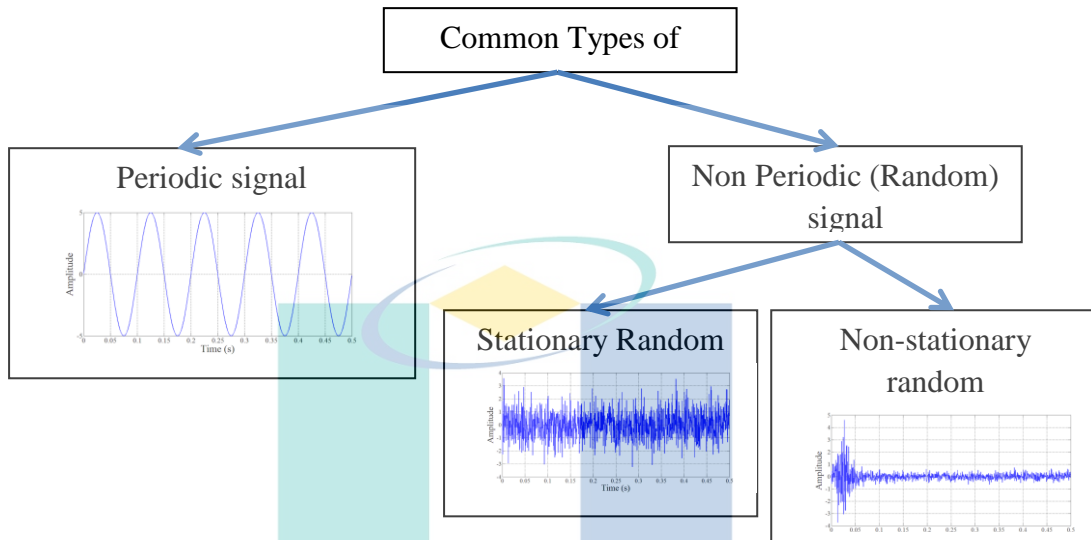
Figure 2.19   Types of Signals
Source: Fish, P. J., (2017)

Despite its distinguishable trend, a random signal is characterized based on some features. According to Fish, P. J., (2017), the random signal can be categorized into two groups, which are stationary and non-stationary random. In stationary random signals, features such as mean and variance from the segmented part are normally recorded almost constant value. Meanwhile, the non-stationary random signal behaves in another way round. This is why the challenge in characterizing non-stationary random signals such as transient might be different compared to the stationary-random signal.

Previous studies revealed the difficulties of characterizing the transient-type signal due to their broad spectrum and short duration (Digulescu, A. et al., 2016; Digulescu, A. et al., 2019). It have been reported that the stationary random acoustic signal was recorded in the previous studies related to CW mode laser welding process (Huang, W. & Kovacevic, R., 2009, 2011). However, due to the pulsation characteristic of PW mode laser welding process, it is expected that non-stationary type of acoustic signal is occurred during this process.

2.7.2   Signal Filtering

Figure 2.18 briefly elaborated on the common approaches taken in signal analysis for the process monitoring purpose. In some studies, signal filtering was done prior to the feature extraction analysis. Basically, the purpose of this process is to eliminate the unrelated bandwidth or noise which influence the trend of signal features. This is vital as the signal features is the predictive variables which could entirely affect the efficiency of the developed predictive model. The acquired signals are filtered either by analog or digital filters (Regalia, P., 2018). Jan, J., (2000) claimed that the digital filter is more adaptive to the modern-world signal processing system as compared to the analog-type.

In signal processing, digital filter can be categorize into Finite Impulse Response (FIR) and Infinite Impulse Response (IIR) filter. Both type of filters can be applied in form of low-pass, band-pass, and high-pass. For the FIR filter, the general transfer function is as shown in equation 2.7 (Kamen, E. W. & Heck, B. S., 2006).

$$H_d(z) = \sum_{n=0}^{N-1} h_d[n] z^{-n} \qquad 2.7$$

In this equation, $H_d(n)$, and N are the truncation of the impulse response, and the length of filter respectively. Meanwhile, the truncation of the infinite impulse respond can be obtained by using equation 2.8 in which it is the multiplication product of the impulse response $h(n)$ and window $w(n)$.

$$h_d[n] = w(n) . h[n] \qquad 2.8$$

Basically, there are several types of window that are available. The most common ones are the rectangular, hanning, and hamming which are shown in equation 2.9, 2.10, and 2.11 respectively.

$$w(n)_{rectangular} = 1 \qquad 2.9$$

$$w(n)_{hanning} = \frac{1}{2} \left(1 - \frac{cos\, 2\pi N}{N-1} \right) \qquad 2.10$$

$$w(n)_{hamming} = 0.54 - 0.46\, cos \left(\frac{2\pi n}{N-1} \right) \qquad 2.11$$

On the other hand, the IIR filters are commonly applied to save time and when the linear phase are secondary factor that need consideration (Smith, S. W., 1997). This type of filter is widely used in sensor signal processing. The most common type of IIR filters are Butterworth and Chebyshev (Kamen, E. W. & Heck, B. S., 2006). Comparing between both types of filters, Chebyshev offer a sharper transition from the passband to the stopband. However, the ripple in the passband might cause significant loss of information which makes Butterworth filter became a popular choice based on the previous works (Bakshi, S. et al., 2019; Rabbi, N. F., 2021). The transfer function of the Butterworth filter is shown in equation 2.12 (Kamen, E. W. & Heck, B. S., 2006). In that equation, $|H(\omega)|$, ω, ω_c and p are the filter transfer function, frequency, cut-off frequency and pole index respectively.

$$|H(\omega)| = \frac{1}{\sqrt{1 + \left(\frac{\omega}{\omega_c}\right)^{2p}}} \qquad 2.12$$

In the previous studies, the uses of filter have been proven to give a significant impact on the predictive model. For instance, in the work related to laser welding process, bandpass filter have been used to enhance the signal features such as root mean squares, and bandpower. As a results, the information associate with the keyhole status, penetration condition, spatter, underfill and humping were well extracted from the filtered signal (Duley, W. W. & Mao, Y. L., 1994; Lee, C. J. et al., 2015).

Apart from the frequency-based filtering method, there is another filtering technique which is made based on the amplitude threshold. Through this technique, the threshold value was set whereas the time-series amplitudes which exceed or less than this value was filtered out. In case of hard-thresholding, the amplitudes that were less than threshold are eliminated. Meanwhile the opposite procedure is implemented in case of soft-thresholding process (Bindusri, M. & Rao, S. K., 2019).

Previous studies associated with transient-type signals, such as in speech (Mihov, S. G. et al., 2009) and electrocardiogram (ECG) applications (Devnath, L. et al., 2015; Karthikeyan, P. et al., 2012) have revealed the significance of the thresholding technique for noise elimination purposes. Among the various techniques, the wavelet thresholding method offers a good de-noising effect and simple algorithm,

making it a popular choice in signal de-noising (He, C. et al., 2015). Basically, Heursure, Rigrsure, Sqtwolog, and Minimaxi are the four types of thresholding methods in wavelet de-noising. However, a comparison between these methods based on the previous works leads to contradicting answers since the performance of these thresholds depends on the decomposition level and type of mother wavelet (Valencia, D. et al., 2016).

Basically, if the time series signal, *x(t)* is represented as a vector with the length of *N*, the following equation can determine the Sqtwolog threshold (Verma, N. & Verma, A. K., 2012).

$$\lambda_{sqtwolog} = \sigma_j \sqrt{2 \log N} \qquad\qquad 2.13$$

In the above equation, σ_j is represented by the following equation

$$\sigma_j = \frac{median\,(|x|)}{0.6745} \qquad\qquad 2.14$$

Different from the Sqtwolog thresholds, the Rigrsure threshold was obtained from several steps of the algorithm (Raj, A. S. et al., 2016). The process began by obtaining a new sequence of *f(k)* by sorting the squared element of x_i in ascending order as shown in equation 2.15.

$$f(k) = (sort(|x_i|))^2 \qquad k=0,1,2,3,\dots N\text{-}1 \qquad 2.15$$

Next, the square root of each element of *f(k)* was calculated through equation 2.16 to obtain a series of threshold λ_k

$$\lambda_k = \sqrt{f(k)} \qquad\qquad 2.16$$

Then, a series of risk, $Risk(k)$ from the series of threshold k was determined according to Equation 2.17.

$$Risk(k) = \left[N - 2k + \frac{\sum_{i=1}^{k} f(i) + (N-k)f(N-k)}{N} \right] \qquad 2.17$$

Finally, the index of k, which corresponded to the minimum risk point in $Risk(k)$ plot was identified and denoted as k_{min} to determine the threshold, as shown in Equation 2.18.

$$\lambda_{rigrsure} = \sqrt{f(k_{min})} \qquad\qquad 2.18$$

Meanwhile, the heursure threshold is the combination of sqtwolog and rigrsure (Bindusri, M. & Rao, S. K., 2019; Valencia, D. et al., 2016). Bindusri, M. & Rao, S. K., (2019) claimed that this type of threshold gives an impact if the rigrsure threshold is small.

Unlike the unbiased risk estimation method, the formula for the Minimaxi threshold is much simpler. The model of this threshold is shown in Equation 2.19 (Karthikeyan, P. et al., 2012).

$$\lambda_{minimaxi} = \sigma_j(0.3936 + 0.1829\,(ln\,N)) \qquad 2.19$$

2.7.3 Signal Feature Extraction

In order to build the predictive model for estimating the weld condition, the trend of predictive variables need to be studied. In signal analysis, these variables are often called the signal features. Basically, there are three main types of analysis involved in features extractions which are time-domain, frequency-domain, and time-frequency analysis. In the time-domain analysis, the discrete point of amplitudes logged from the data acquisition process is normally accumulated in amplitudes distribution, as illustrated in Figure 2.20. Then, statistical features such as maximum amplitude, mean, median, standard deviation, skewness, and kurtosis are extracted from this amplitudes distribution. The trends of these features are commonly used to characterize the signal.
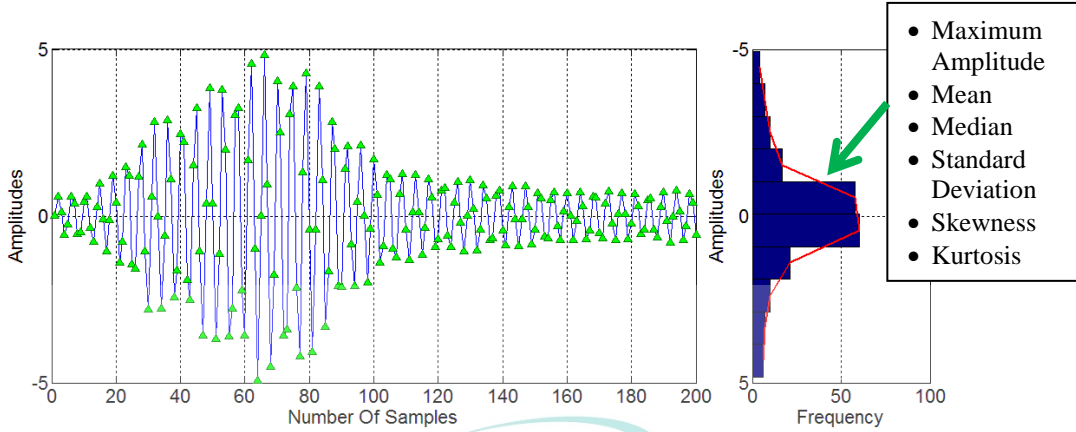
Figure 2.20   Feature extracted from a time-domain signal.

In the previous studies, mean absolute deviation (MAD), standard deviation (SD), and kurtosis were proven to give a significant correlation with weld condition in the case of laser and arc welding processes (Farson, D. et al., 1998; Fidali, M., 2018; Huang, W. & Kovacevic, R., 2009; Zhang, Z., Chen, H., et al., 2015). These features are determined from the equation 2.20 to 2.22

$$Mean\ absolute\ deviation = \frac{1}{n}\sum_{i=1}^{N}|x_i - \mu| \qquad 2.20$$

$$Standard\ Deviation = \sqrt{\frac{\sum_{i=1}^{N}(x_i-\mu)^2}{N}} \qquad 2.21$$

$$Kurtosis = \frac{1}{N}\sum_{i=1}^{N}\left(\frac{x_i - \mu}{\sigma}\right)^4 \qquad 2.22$$

Apart from the common features which apply the concept of statistical moment, there are another method which adapting the L-moment concept. L-moment concept was introduced by Hosking, J. R. M., (1990), to overcome the effect of sampling variability and outlier in the overall distribution. It is a linear combination of order statistic which is computed by using equation 2.23. In this equation r and j represents the L-moment index and sample subset.

$$L_r = r^{-1}\binom{n}{r}^{-1}\sum_{x_1<\cdots<x_j<\cdots<x_r}(-1)^{r-j}\binom{r-1}{j}x_j \qquad 2.23$$

Meanwhile, features such as L-Scale, L-Skewness and L-Kurtosis could be extracted from the ratio between the L-moment. The L-scale, L-Skewness and L-

41

kurtosis were determined by the L-moment ratio shown in Equation 2.24 and Equation 2.26, respectively.

$$L - Scale = \frac{L_2}{L_1} \qquad\qquad 2.24$$

$$L - Skewness = \frac{L_3}{L_2} \qquad\qquad 2.25$$

$$L - Kurtosis = \frac{L_4}{L_2} \qquad\qquad 2.26$$

Even though the use of this type of features is not yet being demonstrated in the studies related to the welding process, it has been proven to be significant in other condition monitoring application recently. In the work associates with the bearing fault diagnosis, Liu, S. et al., (2018) claimed that the use of L-kurtosis extracted from the vibration signal can overcome the inherent drawbacks of the traditional kurtosis which is too sensitive to the outliers. Align with this claim, Bao, W. et al., (2020) detected the periodic impulse by determine the L-kurtosis of the enveloped spectrum of the vibration signal. As a result, the condition of rolling element bearing was successfully revealed. Disregard of these works, there were also other studies which demonstrated the implementation of L-moment concept for rotating machinery application (Gao, Q. et al., 2021; Liu, H. & Shi, Z., 2020)

Apart from statistical moment, the exploration on the other types of algorithm for extracting features from time-series signal still active until recently. Methods such as Non-circular MUSIC algorithm (Chen, Z. et al., 2018), subspace tracker (Lassami, N. et al., 2020), and Multi-lag Phase Space (Bernard, C. et al., 2014) were among the recently proposed method to a time-series signal analysis. Those algorithms were introduced to adapt with various problems related to the signal characteristic which make it challenging to develop the predictive model.
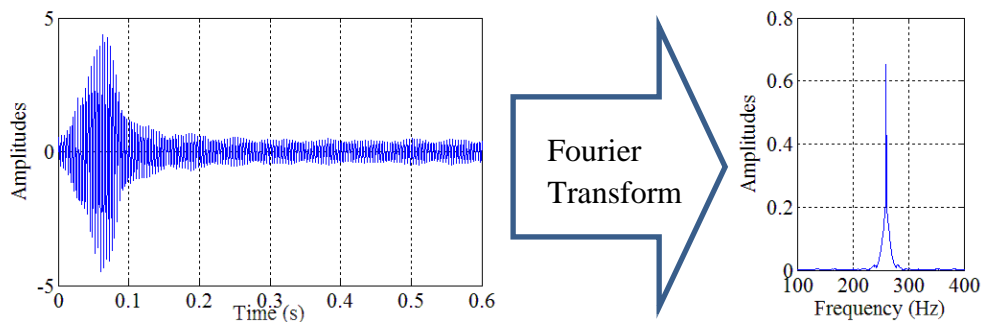
Figure 2.21   Conversion from time-domain signal to a frequency-domain signal.
Source: Staszewski, W. J. & Worden, K., (2009)

In frequency domain analysis, the time-series amplitude is converted into a frequency-amplitude representation by Fourier transform, as shown in Figure 2.21. The conversion is made based on equation 2.27 whereas X_n, x_r, and N, are the complex spectral line, discrete time-series, and number of data point respectively (Staszewski, W. J. & Worden, K., 2009). Based on frequency-amplitude representation, features such as the dominant frequency and bandpower are extracted to characterize the signal. In the previous work, the analysis of amplitude at the dominant frequency band have been claimed to be significant in detecting weld condition (Duley, W. W. & Mao, Y. L., 1994). Moreover, the use of bandpower in the study by Huang, W. & Kovacevic, R., (2009) results in the reliable weld depth prediction model.

$$X_n = \sum_{r=0}^{N-1} X_r \, e^{\frac{-i2\pi nr}{N}} \qquad\qquad 2.27$$
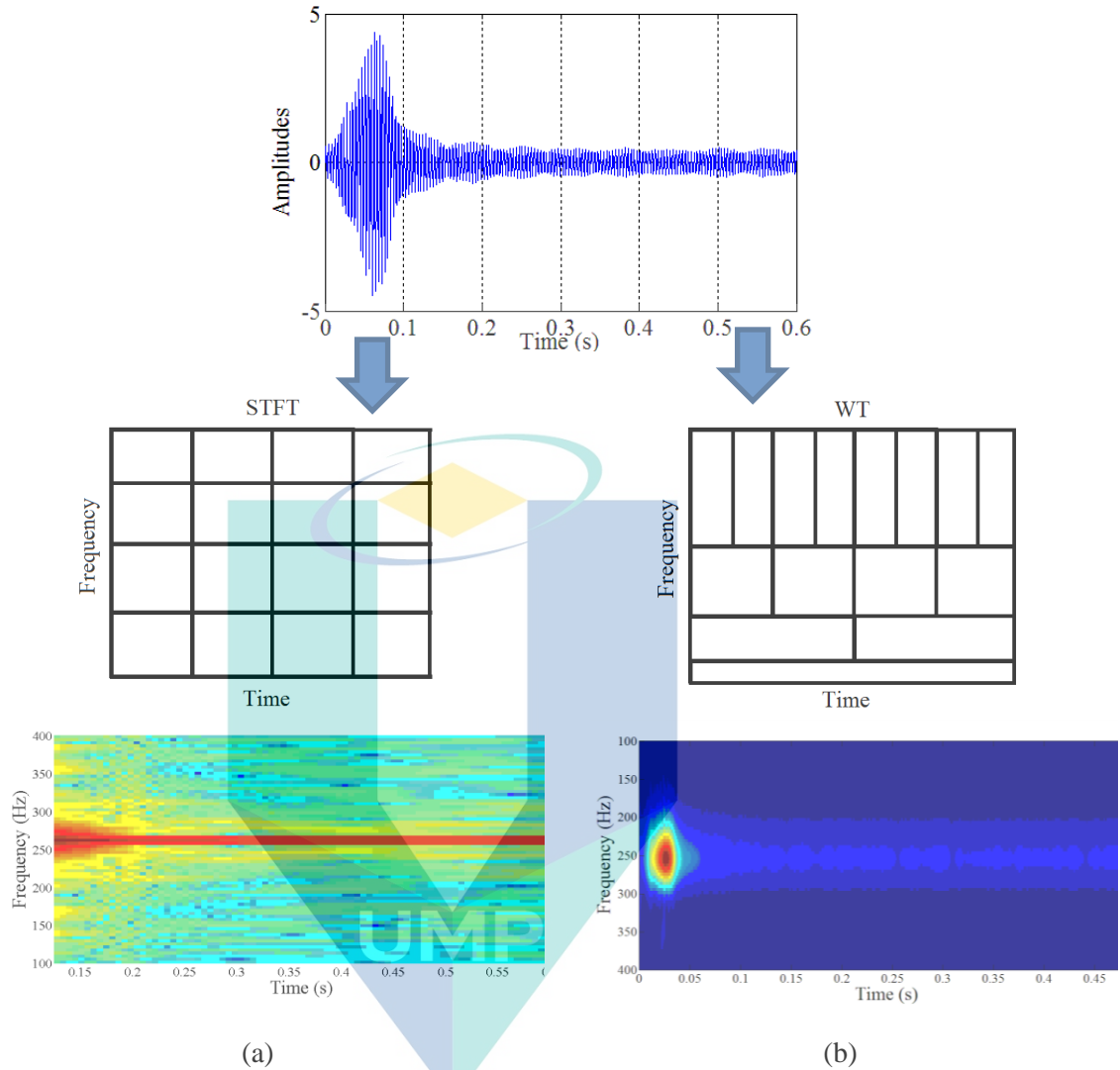
Figure 2.22   Conversion from time-domain to time-frequency representation (a)Short-time Fourier Transform (b) Wavelet Transform.

Source: Giurgiutiu, V. & Yu, L., (2003)

On the other hand, due to the incapability of time-amplitude and frequency-amplitude representation to provide much information simultaneously, analysis of time-frequency is preferable in some applications. Commonly, time-frequency representation is obtained from the Short-Time Fourier Transform (STFT), or wavelet transforms (WT). Both analyses imply a different algorithm that provides their advantages in different ways. As shown in Figure 2.22, time-frequency representation through STFT is done by segmenting the signal into a finite number of components with different time interval and converting each segment into frequency-amplitude (Portnoff, M., 1980).

This provided fast and non-complex analysis, which could save more processing time (Durak, L. & Arikan, O., 2003).

Unlike STFT, the WT represents different frequency resolutions at different bandwidth due to scaling and shifting process of the mother wavelet. As a result, good time resolution but relatively poor frequency resolution could be obtained at high frequencies. Meanwhile, a contradict pattern could be found at low frequencies. This is the reason why WT gives excellent advantages in the analysis of the transient signals (Giurgiutiu, V. & Yu, L., 2003).

Generally, continuous wavelet transform could be done by the formula in equation 2.28 (Staszewski, W. J. & Worden, K., 2009), whereas a, b and φ are scale factor, shifting factor, and mother wavelet, respectively. Specifically, the relationship between frequency, f, and scales, a, is mathematically explained by equation 2.29 whereas ω_0 is the central frequency

$$W_x(a,b) = \frac{1}{|a|^{1/2}} \int_{-\infty}^{\infty} x(t)\varphi\left(\frac{t-b}{a}\right) dt \qquad 2.28$$

$$a = \frac{\omega_0}{\omega} \qquad 2.29$$

Meanwhile, $\varphi(t)$ in equation 2.28 is the function of mother wavelet. Basically, there are several types of mother wavelet that are available for the analysis. In case of transient-type signal, Morlet mother wavelet provided more advantageous as compared to the others (Li, H., 2010). The model of the morlet mother wavelet is shown in equation 2.30 (Iatsenko, D. et al., 2015).

$$\varphi(t) = \frac{1}{\sqrt[4]{\pi}} e^{-j\omega_0 t} e^{-\frac{t^2}{2}} \qquad 2.30$$

After conversion from scale to the frequency in time-frequency space, the wavelet transform of x(t) for a chosen $\varphi(t)$ could be written as

$$W_x(\omega,t) = \int x^+(t)\varphi^*(\frac{\omega(t-b)}{\omega_0}) \frac{\omega dt}{\omega_0} \qquad 2.31$$

2.7.4 Predictive Modelling

Conceptually, the predictive model is developed either for qualitative evaluation or quantitative assessment of the process condition or the output product quality. For the purpose of the quantitative predictive model development, regression-based approach is commonly applied. In welding quality monitoring studies, the most popular methods are the multiple linear regression (MLR) and the artificial neural network (ANN) (Chen, C. et al., 2020; Tomaz, I. V. et al., 2021; Wan, X. et al., 2017; Zhao, D. et al., 2020).

In essence, the development of regression-based predictive model involved several predictive variables from both signal features and process parameters. Through multiple linear regression (MLR) method, the predictive model was generated using a general model shown in Equation 2.32 (Olive, D. J., 2017).

$$Y = \beta_0 + \beta_1 x_1 + \beta_2 x_2 + \cdots + \beta_n x_n \qquad 2.32$$

In Equation 2.32, n is a series of predictive variables from both sound features and weld parameters selected based on the feature selection analysis result. β_0 is the intercept of multi-dimensional surface, while β_n is a series of partial regression coefficients. These coefficients were obtained from the least squares estimation method.

The least squares function is shown in Equation 2.33, and it must be minimized by satisfying both Equation 2.34 and Equation 2.35 to obtain the optimal value of regression coefficients (Montgomery, D. C. & Runger, G. C., 2010). In these equations, n and k represent the number of predictive variables and total number of samples, respectively.

$$L = \sum_{i=1}^{n}\left(Y_i - \beta_0 - \sum_{j=1}^{k}\beta_j x_{ij}\right)^2 \qquad 2.33$$

$$\left.\frac{\partial L}{\partial \beta_0}\right|_{\hat{\beta}_0, \hat{\beta}_1, \dots, \hat{\beta}_k} = -2\sum_{i=1}^{n}\left(Y_i - \hat{\beta}_0 - \sum_{j=1}^{k}\hat{\beta}_j x_{ij}\right) = 0 \qquad 2.34$$

$$\left.\frac{\partial L}{\partial \beta_0}\right|_{\widehat{\beta}_0,\widehat{\beta}_1,\dots,\widehat{\beta}_k} = -2\sum_{i=1}^{n}\left(Y_i - \hat{\beta}_0 - \sum_{j=1}^{k}\hat{\beta}_j x_{ij}\right)x_{ij} = 0 \qquad 2.35$$

In the recent work, Zhao, D. et al., (2020) used MLR method to develop the predictive model for estimating the nugget diameter during the spot welding. Using five different features which were extracted from the power signal, the MLR model was successfully developed. The mean of errors of the model recorded in this study was 5.29%. In another study related to the laser welding process, MLR model (as shown in equation 2.36) was developed to estimate the depth of penetration (Huang, W. & Kovacevic, R., 2011). This model was constructed from the series of predictive variables that combined both sound signal features and weld parameters such as sound pressure deviation (SPD), band power (BP), laser power (LP) and weld speed (WS).

$$DW = 0.7428 + 1.4714\,SPD - 2.0614\,BP + 0.8227\,LP - 0.5504\,WS \quad 2.36$$

In ANN approach, the series of n input parameters have been analyzed to train the neural model. Similar to the MLR method, the general form of the neural network model is formed from the linear combination of weightage and input parameters as shown in equation 2.37. Meanwhile, the overall process flow is illustrated in Figure 2.23

$$f(x_1, x_2, \dots x_n) = w_1 x_1 + w_2 x_2 + \cdots + w_n x_n \qquad 2.37$$

Normalization of Input

Model Training

Model Validation

Model Testing
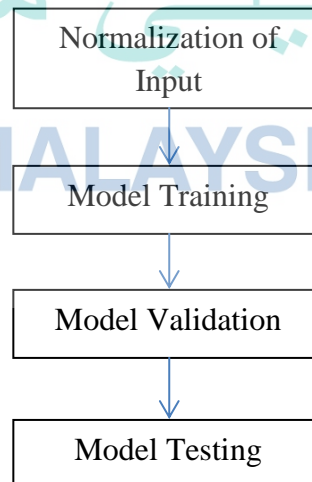
Figure 2.23   Neural Network model development flow diagram

As shown in Figure 2.23, prior to the neural model development, all the input and output data were normalized. This pre-processing technique is important to ensure that the difference in each input range does not affect the entire trend learning (Gupta, A. et al.; Huang, W. & Kovacevic, R., 2011; Zhang, T. & You, X., 2015). Basically, there are several options for the data normalization such as z-score, min-max, lognormal and tanh (Chen, L. et al., 2018; Wu, G. D. & Lo, S. L., 2010). Comparing these methods, min-max seems to be a popular choice cause it offers less time, space and algorithm complexities (Chen, L. et al., 2018). Through min-max technique, both inputs and output were normalized to ensure they ranged from -1 to 1. This was done using Equation 2.38, where y, x_i, x_{max} and x_{min} are the normalized input variables, original input variables, maximum value in the original input variables, and minimum value in the original input variables, respectively. Meanwhile, y_{max} and y_{min} are 1 and -1, respectively, in this case.

$$y = [y_{max} - y_{min}] . \left[\frac{x_i - x_{min}}{x_{max} - x_{min}} \right] \qquad 2.38$$

After the normalization process, the neural model training is being done. There are plenty of alternatives for this purpose and the Lavenberg Marquart backpropagation is the most commonly used neural training model due to its adaptive behavior (Marquardt, D. W., 1963). The purpose of the training algorithm is mainly to minimize the sum of squares error of the network model (Bishop, C. M., 2006; Dreyfus, G., 2005)

Based on the illustration in Figure 2.24, when the multi-layer neuron network received the inputs, the output for each neuron which is the weighted sum of input, is computed by the activation function. Through Lavenberg-Marquart method, both weight and biased is keep on updated until the sum square error (SSE) recorded the lowest achievable amount (Lv, C. et al., 2018). The SSE is computed using equation 2.39 (Yu, H. & Wilamowski, B. M., 2011) in which H, J, μ and I are the SSE function, Jacobian Matrix, combination coefficient, and the identity matrix.

$$H = J^T J + \mu I \qquad 2.39$$

The relationship between gradient vector, g and Jacobian matrix, J is shown by equation 2.40. The element of gradient vector, g is gradient of the relation between errors of neural network model, e and its weightage, w as shown in equation 2.41. In equation 2.41, p is the pattern index while m is the output index.

$$g = Je \qquad\qquad 2.40$$

$$g_i = \frac{\partial E}{\partial w_i} = \frac{\partial\left(\frac{1}{2}\sum_{p=1}^{P}\sum_{m=1}^{M} e_{p,m}^2\right)}{\partial w_i} \qquad\qquad 2.41$$

Recalling back to the briefly explained activation function, there are several options can be choose such as pure linear, tan sigmoid and log-sigmoid. Using the pure linear function does not altering the inputs. However, through tan-sigmoid and log-sigmoid, the inputs of any particular layers are transformed by the equation 2.42 and 2.43 respectively (Kriesel, D., 2007).

$$f(x) = \frac{2}{1 + e^{-2x}} - 1 \qquad\qquad 2.42$$

$$f(x) = \frac{1}{1 + e^{-x}} \qquad\qquad 2.43$$
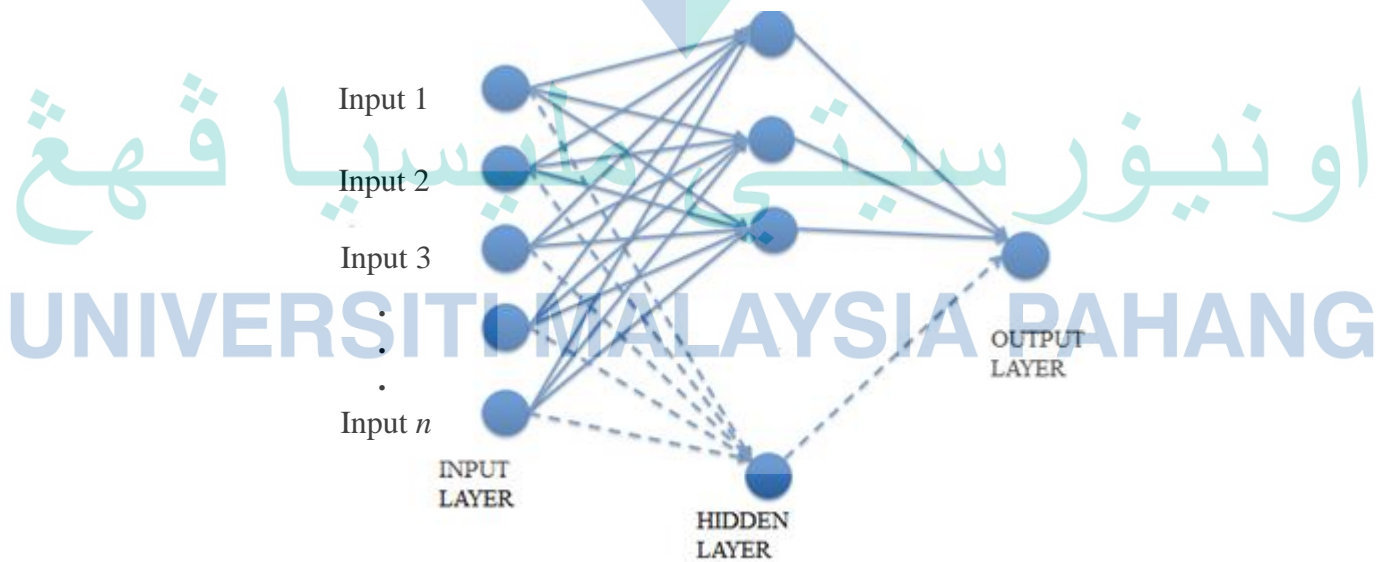
Figure 2.24   Network Model

Like MLR method, the use of ANN method for constructing the prediction model for welding application also recorded a significant numbers. In the previous studies related to the welding process, the predictive models build by ANN method have been proven to be able to predict the nugget diameter during spot welding (Zhao, D. et al., 2020), failure load (Wan, X. et al., 2017) and the depth of penetration (Huang, W. & Kovacevic, R., 2011). The direct comparison between models developed from MLR and ANN methods show that the model developed from ANN method recorded less error (Huang, W. & Kovacevic, R., 2011; Zhao, D. et al., 2020).

2.8   Application of Acoustic Method for Laser Welding Process Monitoring

It was learned that there are plenty of options for monitoring the laser welding process, such as using the electrical, thermal, optical, or acoustic methods. Each method offers its capabilities uniquely in different ways. Among these methods, the acoustic method draws the most attention from previous researchers due to their unique capabilities. For the structure-borne acoustic method, its ability to capture higher frequency signals makes it free from environmental noise disturbance (Bastuck, M. et al., 2016). Besides, detecting a high-frequency signal could lead to the information associated with microscopic phenomena such as phase transformation. On the other hand, an airborne acoustic method has also attracted both academia and industrial practitioner due to their unique features such as high responsible speed, non-contact, and simple sensor setup (Ao, S. et al., 2015; Huang, W. & Kovacevic, R., 2011; Luo, Z. et al., 2016).

In this section, the discussion was extended into the application of both structure-borne and air-borne acoustic methods in studies related to the monitoring laser welding process. Prior to that, the source of acoustic signal from the laser welding process was also explained.

2.8.1   Source of Acoustic Signal during Laser Welding Process

Acoustic signal is emerged from the physical phenomena that occur during the laser welding process. According to the reference (Sun, A. et al., 1999), the structure-borne acoustic signals are commonly originated from crack formation, porosity, phase

50

transformation, and the back-reflected laser. However, until this point, the studies connected to the source of the structure-borne acoustic signal during the laser welding process were not involved the development of a mathematical model except for the case of back-reflected laser, which has been explained by Weerasinghe, V. M. et al., (1990).
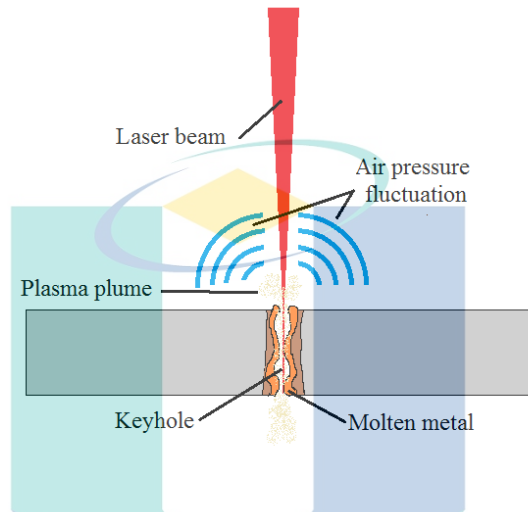
Figure 2.25   Source of air-borne acoustic signal during the laser welding process
Source: Smith, E. T., (1999)

Unlike the structure-borne acoustic signal, Smith. E. T., (1999) explained that physical processes such as plasma plume formation, weld pool dynamics, keyhole oscillation, and gas jet pulsation are among the sources of the air-borne acoustic signal. As illustrated in Figure 2.25, these phenomena resulted in the air pressure variations which fluctuated around the weld zone, producing the air-borne acoustic or sound signal. Previous research shows good agreement with this statement whereas the acquired sound has proved to be significantly related to the aforementioned phenomena. However, not many scholars try to present this correlation numerically due to the fact that many sources including noises influence acoustic generation. In agreement with this statement, Ali, M., (1999) emphasized that the question on how sound generated from laser welding process are still complex to answer, but many scholars agreed that its major source is from the violent plume fluctuation, which causing surrounding air displaced rapidly and propagated as an acoustic wave. Further detail of this phenomenon has been explained earlier through the mathematical model by Dowling, A. P. & Williams, J. E., (1983). In their work, it was pointed out that the

51

evaporation process could be modeled by vapor creation rate, m, which involve parameter such as volume fraction occupied by newly created vapor, β, and vapor density ρ_m as shown in equation 2.44

$$m = \frac{\partial}{\partial t}(\beta \rho_m) \qquad\qquad 2.44$$

When the formed vapor is assumed to displace the ambient air as it streams out from the keyhole, the mass density in a control volume above the keyhole is given by the equation 2.45

$$\rho = \beta \rho_m + (1-\beta)\rho_f \qquad\qquad 2.45$$

Whereas in this equation, the density of the ambient fluid is denoted as ρ_f. Under this circumstance, a differential equation could be written as

$$\frac{1}{c^2}\frac{\partial p'}{\partial t} - \nabla^2 p' = \rho_0 \frac{\partial_2 \beta}{\partial t^2} \qquad\qquad 2.46$$

Under the assumption that the evaporant source is relatively small to the acoustic wavelength in ambient air, acoustic pressure at distance r from the source could be written as the following equation in which c is the speed of sound, and the mass flow rate from the keyhole is proportional to the time derivatives of the volume fraction β

$$p'(r,t) = \rho_0 \frac{\partial^2}{\partial t^2}\left(\frac{\beta(t-\frac{r}{c})}{4\pi r}\right) \qquad\qquad 2.47$$

$$\frac{m}{\rho_m} = \frac{\partial}{\partial t}(\beta) \qquad\qquad 2.48$$

The sound pressure perturbation from unsteady evaporation relates to the time derivative of the evaporation mass flowrate. As the radius distance from the plume increases further, the sound pressure decrease.
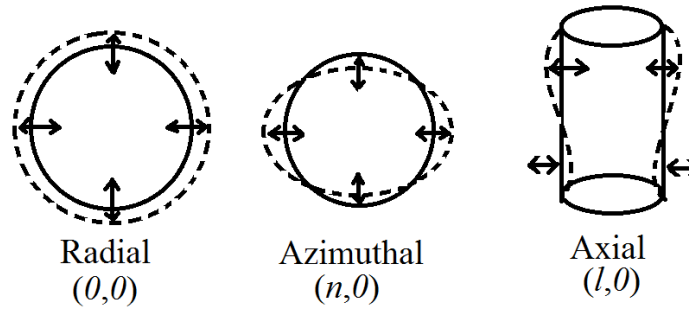
Figure 2.26   Basic keyhole oscillation mode

Source: Klein, T. et al., (1994)

Basically, the oscillation pattern of the formed vapor streamed out from the keyhole was strongly related to the keyhole oscillation behavior. In the previous study, Klein, T. et al., (1994) numerically explained the keyhole oscillation phenomena in response to the difference in the process parameters such as laser energy and keyhole depth. The numerical model was initiated by assuming that the keyhole was cylindrical shape with the primary oscillation mode as depicted in Figure 2.26

Before governing the equation, the pressure and energy balance equation at the equilibrium state was explained. Based on Kroos, J. et al., (1993) , the keyhole was held open by the balance between the surface tension, ablation pressure, and excessive pressure from gas flow along with the keyhole, as shown in equation 2.49

$$P_{abl} + \partial P_g = P_\gamma \qquad\qquad 2.49$$

Explicitly considering the physical phenomena behind the formation of each of the pressures denotes in equation 2.50, the pressure balance equation was expanded as follows

$$mn_g u_g^2 + \frac{1}{3} mn_g u_g^2 \left(\frac{d}{a}\right)^2 = \gamma \left(\frac{1}{a}\right) \qquad\qquad 2.50$$

In equation 2.50, m, n_g, u_g, γ, d, and a, represent the mass of ablating particles, hydrodynamic density, velocity, surface tension coefficient, the thickness of the workpiece, and equilibrium radius of the keyhole respectively.

Apart from the pressure balance equation, the energy balance equation was also governed to determine the equilibrium-state keyhole radius. In principle, the absorbed energy flux is balanced from the summation of ablation energy flux and heat conduction loss as been represented in equation 2.51

$$q_{abs} = q_\lambda + q_{abl} \qquad 2.51$$

Under an assumption that the laser power is distributed in Gaussian pattern and it is uniformly distributed along the keyhole's wall, the absorbed heat flux density was governed as shown in equation 2.52 whereas A, P_L, and r_0 in the equation denotes the overall absorption coefficient, total power, and laser beam radius respectively.

$$q_{abs} = \frac{AP_L}{2\pi a d} \left(1 - e^{-2\left(\frac{a}{r_0}\right)^2}\right) \qquad 2.52$$

On the other hand, by the basis of the governing equation from the previous work related to the analysis of heat conduction in penetration welding (Simon, G. et al., 1993), the approximation of heat loss represented in equation 2.53

$$q_\lambda = \frac{T_s - T_0}{2} \varrho c_p v \left(\frac{K_1(Pe)}{K_0(Pe)}\right) \qquad 2.53$$

In equation 2.53, T_s, c_p, Pe, and ϱ are the keyhole surface temperature, specific heat, Peclet Number, and the average mass density of the liquid phase. Meanwhile, the ablation energy flux at the keyhole surface could be represented by equation 2.54 in which h_{ev} is the latent heat of evaporation

$$q_{abl} = m n_g u_g h_{ev} \qquad 2.54$$

Combining these equations, the stable radius of keyhole at equilibrium state could be obtained. Based on this radius value, the fluctuation of the keyhole radius was represented in equation 2.55 in which $\alpha(t)$ denotes the oscillating value of the radius, a, with respect to time.

$$r_s(t) = a + \alpha(t) \qquad 2.55$$

This is also known as the ground mode oscillation, which is the basic mode of keyhole oscillation, and its eigenfrequency was governed by applying energy balance equations and Langrage mechanic (Klein, T. et al., 1994) as shown in equation 2.56

$$\omega_{00} = \frac{B}{\varrho\, a\, \ln(C)} \qquad\qquad 2.56$$

Referring to Figure 2.26, there is another mode of keyhole oscillation apart from the ground mode. Basically, the axial and azimuthal oscillation mode was represented by equation 2.57, whereas k denotes the axial wavenumber while n is the mode number.

$$r_s(t) = a + \cos(n\emptyset)\cos(kz)\alpha(t) \qquad\qquad 2.57$$

Like ground mode or radial oscillation, the eigenfrequency of the axial and azimuthal oscillation in equation 2.58 was also governed from the energy balance concept.

$$\omega_{nl}^2 = \frac{ka\,|kn'(ka)|}{kn\,(ka)}\left[\frac{\gamma}{a^3\varrho}(n^2 + k^2 a^2) + \frac{B}{a\,\varrho}\right] \qquad\qquad 2.58$$
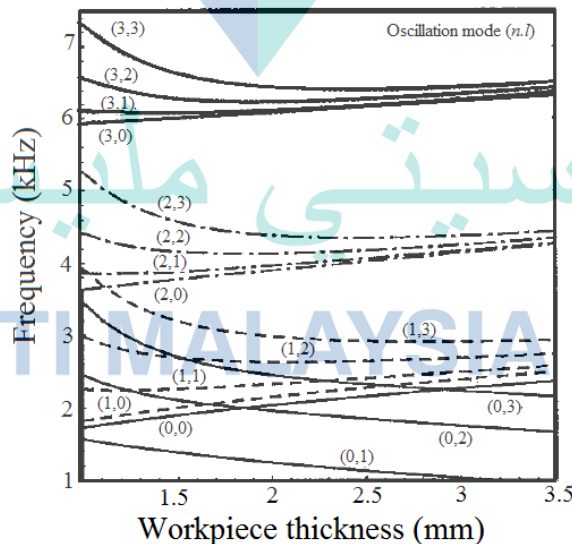
Figure 2.27   Eigen-frequency of radial, axial and azimuthal oscillation calculated for the iron plate with the variation of thickness

Source: Klein, T. et al., (1994)

Figure 2.27 shows the variation of eigen-frequency of radial, axial, and azimuthal oscillation calculated for iron plates with the variation of thickness and laser beam radius of 150 μm (Klein, T. et al., 1994). In this figure, n and l represent the azimuthal and axial mode numbers, respectively. According to the plot, the frequency value is not much clearly distinguishable by the change in workpiece thickness and different axial wave number at the same azimuthal mode number. However, the change in frequency was quite evident when there is a change in azimuthal mode.

2.8.2 Application Of Structure-Borne Acoustic wave for Monitoring Laser Welding

As underlined in section 2.7, the acoustic method implies either by acquiring a structure-borne or air-borne acoustic wave signal. Table 2.3 shows the list of studies associated with laser welding quality monitoring using both types of acoustic signals for the past several decades. Basically, structure-borne acoustic wave or transient elastic wave is emitted as a response from the rapid release of energy from the localized source at a vast frequency range, typically from 20 kHz to 2MHz. Therefore, the acquired signal is usually not influenced by the harsh environmental noise from the process (Bastuck, M. et al., 2016). Besides, the phrase structure-borne is used due to its nature of propagating through the solid structure. For this reason, acquiring structure-borne acoustic waves is commonly done by using a piezoelectric sensor which contacted directly on the surface of the workpiece (Lee, S. et al., 2014).

Past evidence, which was generally described in Table 2.3, shows that this method is capable of detecting defects such as crack initiation mechanism (Lee, S. et al., 2014), back-reflected laser (Li, L., 2002; Weerasinghe, V. M. et al., 1990) as well as porosity (Sun, A. et al., 2001). In a study by Lee, S. et al., (2014), it was revealed that the acoustic emission signal was originated from the rapid phase transformation between liquid and solid state. As the crack are occurred from the uncertainties in solidification process (Huang, R. S. et al., 2008), the change in characteristic of the acoustic emission signal was lead to the information related to the initiation of crack. On the other hand, Sun, A. et al., (2001) revealed that the acoustic emission signal was more sensitive in detecting porosities underneath the weld bead. According to Berger,

P. et al., (2011), the porosity was formed due to inappropriate solidification rate and back filling speed of the molten metal. In case of PW mode laser welding process, plasma temperature dropped drastically when the laser beam was shut down, especially at the bottom part of the fusion zone. Consequently, the solidification completed before the keyhole is completely collapse which results in the formation of porosity as shown in Figure 2.28 (Zhou, J. & Tsai, H. L., 2006). As the rapid transformation between liquid and solid state have been the source of acoustic emission signal, these phenomena gives a significant impact to the characteristic of the signal.
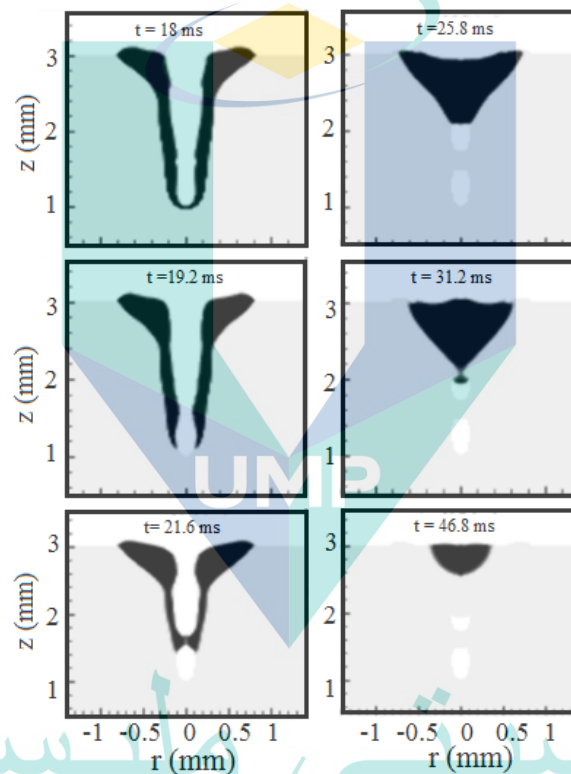
Figure 2.28   Evolution of keyhole collapse and solidification in a large depth-to-width weld bead

Source: Zhou, J. & Tsai, H. L., (2006)

Even though the capabilities of the acoustic emission method have been reported in the previous studies, the application of this method recorded a lack in number. This might be due to the nature of this method, which needs the sensor to be directly contacted on the surface of the workpiece, which is considered difficult when dealing with high-temperature processes like welding.

Table 2.3   Studies related to the laser welding quality monitoring using structure-borne and air-borne acoustic method

Author	Methodology	Material	Signal Type	Pre-Processing	Analysis	Detected phenomena
(Weerasinghe, V. M. et al., 1990)	CO₂ Laser Bead on plate	N/A	Acoustic emission	N/A	AE RMS, frequency	Back reflected laser
(Li, L., 2002)	CO₂ laser	Mild Steel	Acoustic Emission	N/A	AE RMS, frequency	Back reflected laser
(Lee, S. et al., 2014)	NdYAG laser Pulse mode	304 stainless steel	Acoustic emission	N/A	AE signal values at selected frequency band Back Propagation ANN	Melting Solidification Joined Condition
(Sun, A. et al., 2001)	N/A	N/A	Acoustic Emission Infrared Ultraviolet Acoustic	N/A	Choi William Kernel Distribution	Depth of penetration Porosity
(Farson, D. et al., 1998)	CO₂ Laser Continuous mode LapJoint	Carbon steel	Acoustic	N/A	Root Mean Square	Depth of penetration (classification)
(Duley, W. W. & Mao, Y. L., 1994)	CO₂ Laser Bead on plate	Alluminum 1100	Acoustic	Bandpass filter	Amplitude of Frequency domain signal	Depth of penetration keyhole condition
(Farson, D. et al., 1996)	Continuous mode Lap joint	304 stainless steel	Acoustic	Short Time Fourier Transform	Band power Artificial Neural Network (Classification penetration condition) Spectrum energy (Gap analysis)	Depth of penetration Gap
(Szymanski, Z. et al., 2000)	CO₂ laser Continuous mode	Mild steel Stainless steel	Acoustic	N/A	Mathematical Model Spectrum analysis	plasma plume oscillation
(Hoffman, J. et al., 2002)	N/A	Austenitic steel	Acoustic	N/A	Mathematical Model (Verified by experiment)	plasma plume oscillation
(Huang, W. & Kovacevic, R., 2009)	Continuous mode Lap joint	DP980 HS steel	Acoustic	Spectral Subtraction	Band power Sound Pressure Deviation	Depth of penetration (classification)
(Huang, W. & Kovacevic, R., 2011)	Continuous mode Lap joint	DP980 HS steel	Acoustic	Spectral Subtraction	Band Power Sound Pressure Deviation Artificial Neural Network Multiple regression	Depth of penetration (estimation model)
(Ao, S. et al., 2015)	NdYAG laser	Iron	Acoustic	N/A	Mathematical Model (Verified by experiment)	Weld Pool Oscillation frequency
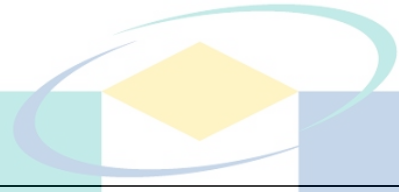
Table 2.3　　Continued

Author	Methodology	Material	Signal Type	Pre-Processing	Analysis	Detected phenomena
(Luo, Z. et al., 2016)	NdYAG laser Continuous mode	Steel plate	Acoustic	N/A (use sound proofing equipment to avoid noise)	Acoustic pressure level Time delay recognition	Burn through
(Lee, C. J. et al., 2015)	CO_2 Laser Continuous mode LapJoint	AH 36 structural steel	Acoustic Photodiode	Bandpass filter	Root Mean Square	Spatter / Underfil Humping
(Farson, D. F. et al., 1999)	CO_2 Laser Continuous mode ButtJoint	Carbon steel	Acoustic OpticalPlasma	N/A	Linear Discriminant analysis	Classification of full penetration, overheat penetration and half penetration
(Gu, H. & Duley, W. W., 1996)	CO_2 Laser Lap & Butt joint, Bead on plate	Mild & Galvanized steel	Acoustic	N/A	Sum of a squared standard deviation Discriminant function	Depth of penetration
(Farson, D. F. & Kim, K. R., 1999)	CO_2 Laser Bead on plate	Low carbon steel	Acoustic Optical	N/A	Prediction model	Acoustic and plasma emission trend based on material evaporation and formation of ionized plume
(Ao, S. et al., 2010)	NdYAG laser Bead on plate	Cold rolled steel	Acoustic	N/A	Frequency Domain PCA-ICA	Blowholes

59

2.8.3 Application Of Air-Borne acoustic wave for Monitoring Laser Welding Process

Apart from using a structure-borne acoustic signal, the use of air-borne acoustic signals as a medium for monitoring the laser welding process has also been explored since the past several decades. Theoretically, the air-borne acoustic waves are generated from sources within the audible frequency range between 20Hz to 20 kHz (Huang, W. & Kovacevic, R., 2011). It is propagating through the air, which would promote non-contact measurement. Apparently, plasma plume formation and weld pool oscillation are two phenomena that could be considered major sound sources during the laser welding process (Smith, E. T., 1999; Ali, M., 1999; Dowling, A. P. & Williams, J. E., 1983). Any instability on those occasions would consequently affect weld quality. Thence, it is crucial to monitor those phenomena.

Studies related to the use of acoustic method for monitoring laser welding process were shown in Table 2.3. In early work, attempts have been made to understand the process of sound emission from the dynamic of plasma plume, keyhole, and molten metal. For example, Farson, D. F. & Kim, K. R., (1999) have formulated the prediction model for generating air-borne acoustic signals. According to their formulation, the generated sound pressure was influenced by the vapor flow rate since the surrounding air was displaced by the vapor emanating from the keyhole. Szymanski, Z. et al., (2000) and Hoffman, J. et al., (2002) also have confirmed this statement in both of their mathematical and experimental analysis. Moreover, in their analytical work, the zone occupied by plasma was considered as an impenetrable pulsating sphere.

Regardless of plasma plume formation, the acoustic signal could also emerge from the weld pool or keyhole oscillation. Due to this fact, Ao, S. et al., (2015) make an effort to predict the oscillatory frequency from the modeling process of weld with different penetration depth induced by different weld speeds, as shown in Figure 2.29. Results from their work show that from two-dimensional modeling process, the simulated weld pool oscillation frequency deviates around 4 % from the experimental results.
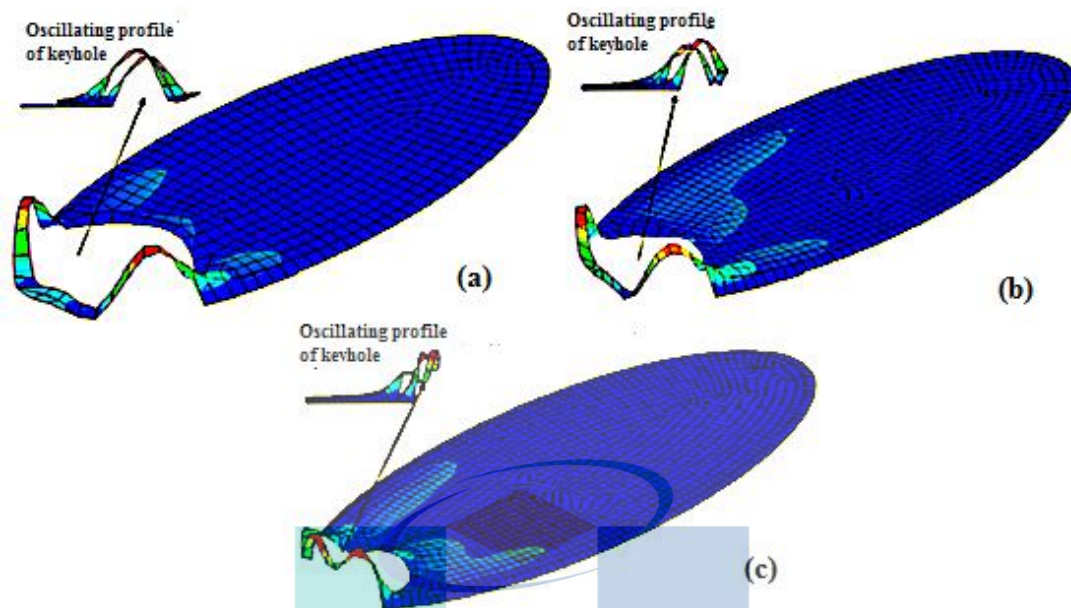
Figure 2.29   Simulation results of the weld pool oscillatory profile from the process with different weld speed (a) f=1453.125 Hz, v=3 cm/s (b) f=1890.625 Hz, v=4 cm/s (c) f=2750 Hz, v=5 cm/s

Source : Ao, S. et al., (2015)

The earlier statement emphasized that any instability of physical phenomena that emerges from the laser welding process could lead to defects. Hence, despite implying an air borne acoustic signal to gain a deeper comprehend on plasma plume formation and keyhole oscillation, the direct relation between the behaviors of the acquired acoustic signal with weld condition also has been investigated. Some evidence proved that information embedded in the acquired acoustic signal could be significantly used to determine the weld condition, detect and locate the defect. For instance, the correlation between acoustic spectral features and depth of penetration has been investigated by Duley, W. W. & Mao, Y. L., (1994) . In their study, the test was done on 2 mm thickness Aluminum 1100 using CO_2 laser welding while the captured sound signal was low passed filtered with a cut off frequency of 10 kHz. According to the result in Figure 2.30, it was reported that the emission of the acoustic signal was dominant between 0 - 1 kHz at low incident laser intensity. In contrast, a peak within 9 kHz to 10 kHz was found increasing in its amplitude simultaneously with gaining laser intensity. Consequently, the overall amplitude arises with extended depth of penetration. Furthermore, the frequency component between 3 – 9 kHz was perceived

to be connected with the closure of the keyhole over part of its length due to hydrodynamical instabilities. Thence, the partial closure of the keyhole could be detected by observing the spectrum within this frequency range.
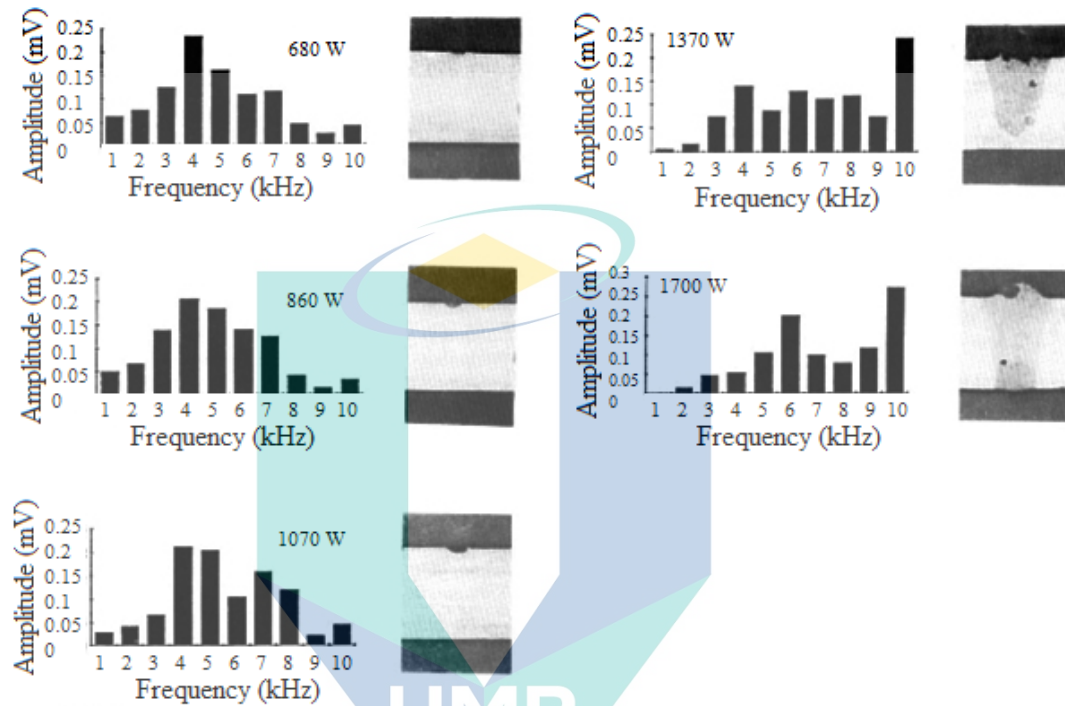
Figure 2.30   Acoustic Spectral Trend from the process with different laser power and weld penetration

Source: Duley, W. W. & Mao, Y. L., (1994)

Similar work also has been reported by Farson, D. et al., (1996), whereas the characteristic of the acoustic signal was analyzed in an attempt to identify the weld quality, which is qualitatively determined by the depth of penetration and gapping. The experiment was done on a 304 stainless steel plate. Unlike the previously reported works, the time-frequency approach was taken by implying Short Time Fourier Transform (STFT) to identify the significant frequency range with respect to the weld quality. The significant range was recorded to be within 1 kHz to 2 kHz in which its energy dropped when insufficient penetration was detected through the analysis. This trend could be referred to in Figure 2.31. Meanwhile, by calculating the total signal strength, a clear distinction between the gapped and normal weld could be observed. The use of an Artificial Neural Network to classify the penetration status also has been

demonstrated in their study. With the use of ANN, full penetration and partial penetration weld could be distinguished in a different group.

Energy drop within this bandwidth
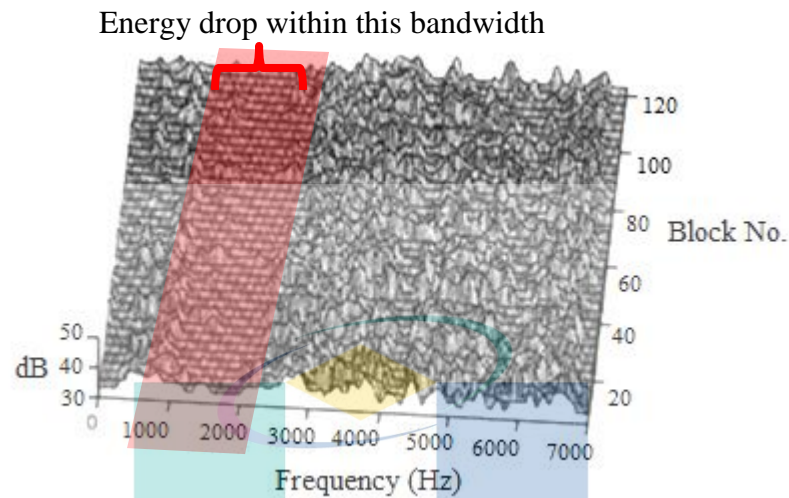
Figure 2.31   Spectrogram of acquired sound signal
Source: Farson, D. et al., (1996)

As reported in earlier work, it could be concluded that monitoring the penetration status by analyzing the acquired sound is possible to be done. However, the reported work emphasizes the cases involving a narrow range of welding parameters, making it challenging to ensure the robustness of the method. Hence, in the comprehensive study by Farson, D. et al., (1998), the investigation was done in a broader range of power and travel speed. As a result, the classification of penetration status could be extended into moderately full penetration as an addition to the present full and partial penetration class. This work described that the Root Mean Square (RMS) of the acoustic signal was high at moderate full penetration and eventually decreasing as the penetration status felt into partial penetration class. Disparate from the other work, Farson, D. et al., (1999) paid more attention in identifying the penetration status during high power or keyhole welding. Supported by measured optical charged particle data, the depth of penetration status could be classified into full- , overheat- , and half-penetration. In this study, the overheat penetration referred to weld produced by excessive linear heat input, which consequently caused a significant level of top surface concavity and larger heat affected zone. Meanwhile, the classification was done through Linear Discriminant Analysis (LDA). Similar findings have also been described by Gu, H. & Duley, W. W., (1996), whereas through discriminant analysis,

three penetration status groups were successfully classified. Moreover, it was found that bad quality weld could be easily identified by determining the sum of a squared standard deviation. In another work by Huang, W. & Kovacevic, R., (2009), the classification was done by analyzing both time and frequency domain signal characteristics. Uniquely, in their research, the spectral subtraction method was demonstrated to diminish the influence of noise in the analysis result, and the outcome was found to be promising. As an observation made onto the captured time domain, it was reported that the overall sound pressure increase aligns with the growth in penetration depth. Meantime, the power density of the frequency spectrum from 500 Hz to 1500 Hz was large for full penetration cases as compared to half penetration.

Classifying the penetration status is insufficient for the case where the quantitative assessment of weld penetration is needed. To overcome the drawback, Huang, W. & Kovacevic, R., (2011) have utilized the Artificial Neural Network (ANN) analysis in an attempt to quantitatively characterize the relation between the captured sound and the depth of penetration. In this extended work, the multiple regressions also have been applied and campared with ANN results. According to the obtained results, by giving the value of sound pressure deviation and band power as an input to the model, the best neural network model was found to predict penetration depth with a standard deviation error of 8.91%. Meanwhile, for the multiple linear regression model, the standard deviation error was recorded to be 8.25 %.

Despite the classification and characterization of the weld penetration depth, studies were also extended into the detection of other types of defects. For instance, Luo, Z. et al., (2016) exhibit the use of multiple microphones to detect and locate the burn through. In their study, the soundproof equipment was specially design and used to avoid the influence of noise during the sound acquisition process. Based on the illustrated result, soundproof equipment was evidently influence the result. It was noted that the detection and location of burn trough defect based on the sound pressure level and time delay recognition analysis was done with a lesser error when soundproof equipment was used.

Lap welding : f_d = -2 mm, P = 6 kW, v = 1 m/min, G_C = 0.2 mm, He shield (Q = 25 l/min)
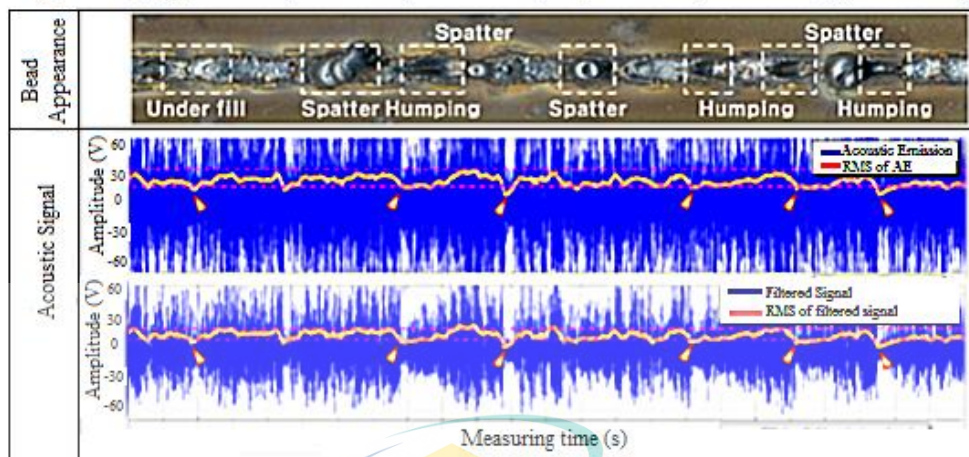
Figure 2.32   RMS of the acoustic signal during the presence of damage
Source: Lee, C. J. et al., (2015)

In other studies, the use of the acoustic method was also reported to be significant in detecting detect other types of defect such as underfil and humping. As depicted in Figure 2.32, in work by Lee, C. J. et al., (2015), the effect of Zn coating thickness and gap between the lap joint, to the degree of those defects were monitored based on the acquired sound signal. From the drawn result, the amount of spatter that influences the existence of underfil and humping was found to be consistent between 0.08 to 0.2 mm gap size depending on the coating thickness. Simultaneously, within the same range, the recorded RMS of the sound signal was significantly changed. Moreover, the frequency spectrum analysis shows that the dominant frequency lies within 1 kHz for both 15 micrometers and 30 micrometers Zn coating thickness. However, the amplitude of the spectrum appeared in a descending pattern when coating thickness increased. They have suggested that this is due to the large thickness value contributing to high vapor pressure, which consequently suppressed the keyhole's periodic motion. In addition, the amplitude of the time-domain sound signal, which was filtered at the dominant frequency, has also show deviating values from 22V to 38V when the defect exists. In another unique study, Ao, S. et al., (2010) apply a blind source separation technique that combining principal component analysis (PCA) and independent component analysis (ICA). Through blind source separation analysis, the acoustic signal was successfully decomposed into cooling and keyhole component, and the existence of blowholes was detected.

65

2.9   Literatures Summary

The chart in Figure 2.33 represents the summary of previous works discussed in section 2.7. According to the chart, studies that involved the use of sound method for monitoring the laser welding process were varied in its experimental setup, analysis approach, and giving different significant results. Focusing on the experimental setup variation, all studies were distinguishable by the different laser mode, laser type, workpiece materials, and the joining configuration or design. Meanwhile, the diversity in the analysis approach was also noticeable. However, it could be said in general that the sound feature extraction and noise elimination analysis have been implied to characterize the signal before correlating its trend with the weld condition. As a result, each study has given different contributions, which could be divided into three main categories which were the detection of defects, qualitative classification of defects, and characterization of defects. In studies that attempted to detect the presence of a defect, several signal feature extraction analysis have been explored to find the best features that could give significant information regarding defects during the process.

In another group of work, the signal analysis was done to qualitatively classify the defect by its size. For example, the weld penetration size could be classified into half-penetrated and fully penetrated based on the trend of the analysis sound features. On the other hand, some studies significantly developed the model to quantitatively characterize the weld condition or the defect's actual size.
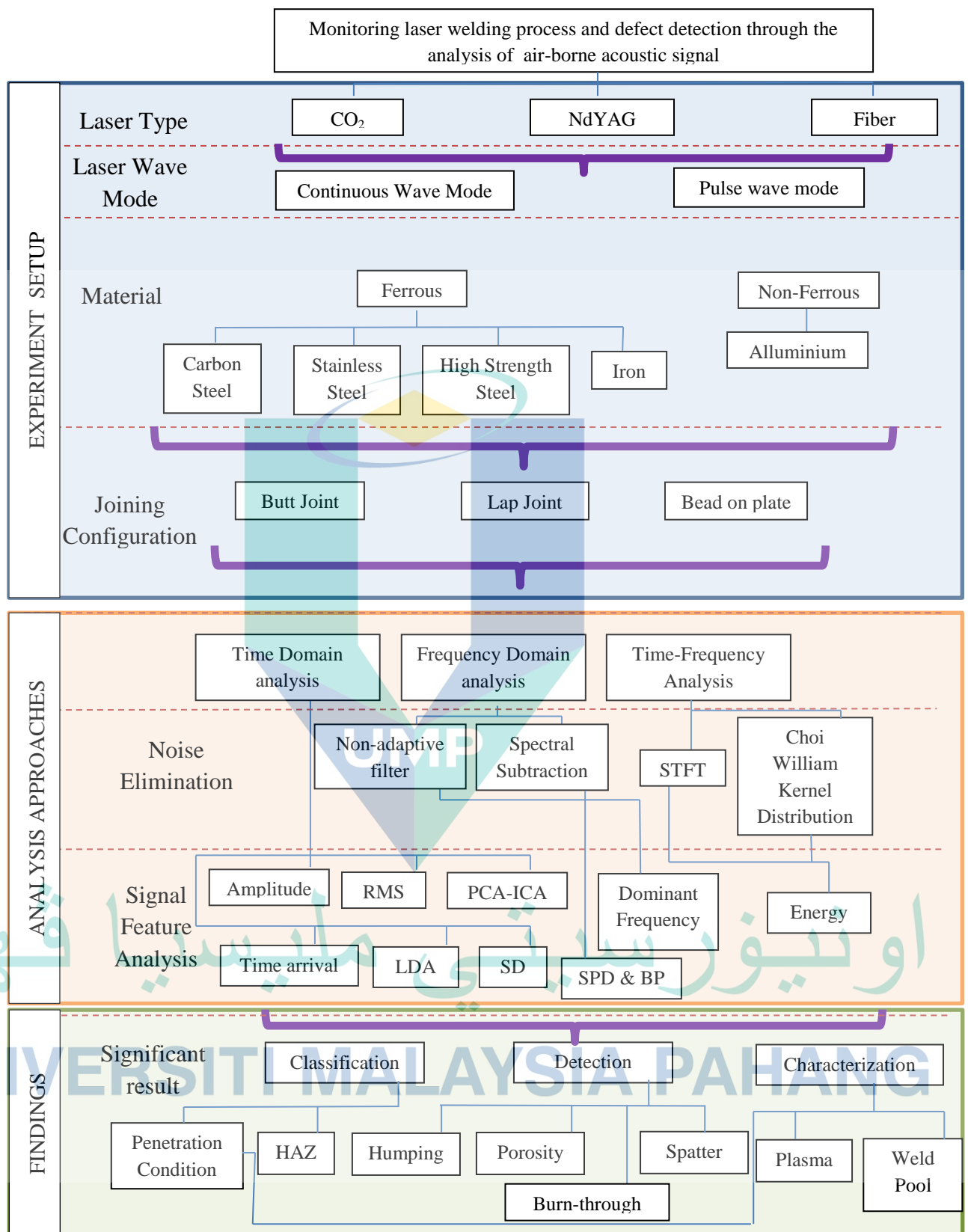
Figure 2.33   Summary of studies related to the analysis of airborne acoustic signal for laser welding monitoring

Based on the literatures discussed in Figure 2.33, it could be summarized that the sound method for laser weld process monitoring has been explored in a diversity of laser welding types, laser mode, workpiece material, and the joining design. The analysis approach also varied to achieve their different goals that contribute to knowledge. Nowadays, industries demand greater process control to achieve quality assurance, making the development of monitoring methods essential. Therefore, this knowledge is essential to expand or enhance the sound method's capability for monitoring the laser welding process before it is ready for commercialization

In modern manufacturing nowadays, the customer requirement trend started to change, and the criteria needed in the production line also change accordingly. Zhou, K. et al., (2015), stated that Industry 4.0 tends to achieve more intelligent manufacturing processes through the construction of Cyber-Physical Production Systems (CPPS), and the implementation of smart factories. In constructing CPPS, the integration of process control and monitoring system are one of the essential factors. Based on the literature summary, it was learned that the capability of acoustic method for the online monitoring purpose has been widely explored in various laser welding mode, laser type, material as well as the joining design. As a result, numerous defects were detected, classified, and characterized by the acquired sound signal analysis during the laser welding process. All of these studies were important and significantly contributed to the knowledge in developing a robust process monitoring system.

Basically, there are still many rooms for improvement before an acoustic method could be established in industrial applications, and Figure 2.34 illustrates the focus given in this study. In this particular study, attention was given to the weld penetration condition. The severity of incomplete penetration is not much different from the other types of defects if it has existed in the welded joint. According to some earlier studies (Boulton, C. F., 1976; Lawrence, F. & Munse, W., 1973; Singh, P. J. et al., 2002), the spot where the incomplete penetration exists is possibly being a crack initiation point, which consequently reduces the fatigue life of the weld joint. This is the reason why this study tries to focus on this angle.
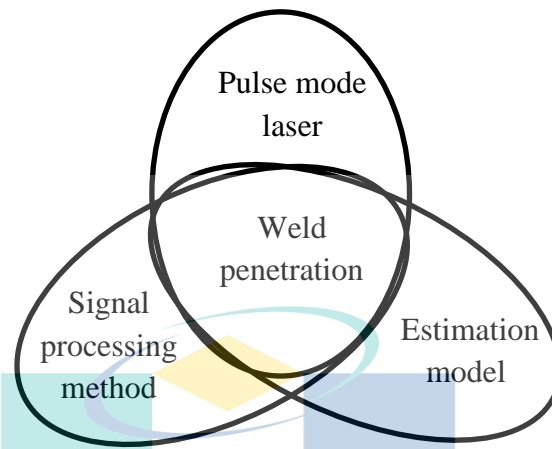
Figure 2.34   Research focus

Most of the previous works reported in Figure 2.33 were emphasized on the continuous mode (CW) laser. It was perceived that lack of attempt is made to understand the emitted sound behavior during pulse mode (PW) laser welding and how it could be correlated with the weld penetration condition. Based on the previous studies, it could be summarized that the dynamic of the plasma plume might change when the laser energy penetrates deeper inside the material. This has resulted in a significant change of sound feature trend in the case of CW laser as it emitting a stationary random signal. However, the question that might arise among scholars is how the characteristic of sound changes with the deeper penetration in the pulse-mode process. Due to the reason that the pulse-mode laser welding could emit a non-stationary random acoustic signal, extracting the information with respect to the weld penetration might be challenging. Therefore, it is also important to look into this matter.

On another angle, previous studies have demonstrated the use of time-domain, frequency-domain, and time-frequency analysis to find the sound feature which gave a significant trend with the change in weld penetration (Duley, W. W. & Mao, Y. L., 1994; Farson, D. et al., 1998; Farson, D. F. et al., 1999; Huang, W. & Kovacevic, R., 2009, 2011; Sun, A. et al., 2000). Apart from the penetration condition, studies also revealed that these analyses were able to be used to monitor another type of defects (Ao, S. et al., 2010; Duley, W. W. & Mao, Y. L., 1994; Gu, H. & Duley, W. W., 1996;

Lee, C. J. et al., 2015; Luo, Z. et al., 2016; Sun, A. et al., 2000). Even though these studies were promising, the influence of noise during the acquisition process remains as a problem. Due to this reason, a method such as bandpass filter (Duley, W. W. & Mao, Y. L., 1994; Lee, C. J. et al., 2015), spectral subtraction (Huang, W. & Kovacevic, R., 2009, 2011), Short-time Fourier Transform (Farson, D. et al., 1996), and William Choi Kernel Distribution (Sun, A. et al., 2001) have been used to improve the results. As the pulse-mode process might emitting a sound signal with different behavior, it is crucial to understand what type of noise filtering method is suitable. Therefore, much space for a research exploration is still available to better understand this matter. This is why the exploration of the signal processing method for noise elimination and feature extraction is also emphasized in this work.

In an earlier discussion, it has been explained that most of the studies related to the use of the sound method in monitoring the weld penetration look into how the trend of signal features could be used to classify the penetration condition. For example, the statistical feature was extracted from the acquired sound signal, and analyze to classify whether the weld joint was half-penetrated or fully penetrated. Basically, it is important to characterize the size of penetration instead of qualitatively evaluates its condition. This is because the severity of weld penetration was also high, even if it is incomplete in a minimal length. Huang, W. & Kovacevic, R., (2011) have put an effort to develop the weld depth estimation model from the analysis of sound in case of continuous mode laser welding. Basically, this finding has opened a way to achieve a great process control in industry 4.0 as the process could be controlled directly after getting the estimated weld depth from the sound measurement system. However, before it could be established, it is important to learn how the weld depth estimation model differently performed for the various types of laser welding processes, including the laser mode. Therefore, in this study, the weld depth estimation model was also developed.

CHAPTER 3

METHODOLOGY

3.1   Introduction

Figure 3.1 depicts the overall of methodology for the study. The entire process started with the specimen preparation. Then, the experiment was designed by carry out the preliminary experiment. Basically, the preliminary experiment was conducted to determine the optimum values for the constant parameters that were set in this study. Moreover, the optimum ranges for the independent parameters were also obtained from the preliminary experiment. This part of work was crucial because it explained how the experiment was designed in this study. Therefore some related results were also presented in this part.

The process continued with experimental work. In Section 3.4 and Section 3.5, the method of experiment and data acquisition setup, respectively, was explained in detail before the method of sampling and macrographic imaging was further elaborated in Section 3.6. After the experiment and sampling process, the signal was analyzed by extracting its features. The method of feature extraction from the acquired sound signal was explained in Section 3.7. At the same time, another feature extraction algorithm was developed in this study and the development process was detailed out in Section 3.8. To evaluate the significance of the extracted features, feature selection analysis was carried out and the method for this analysis was elaborated in Section 3.9. In the final part, the method of estimation model development was explained in detail.
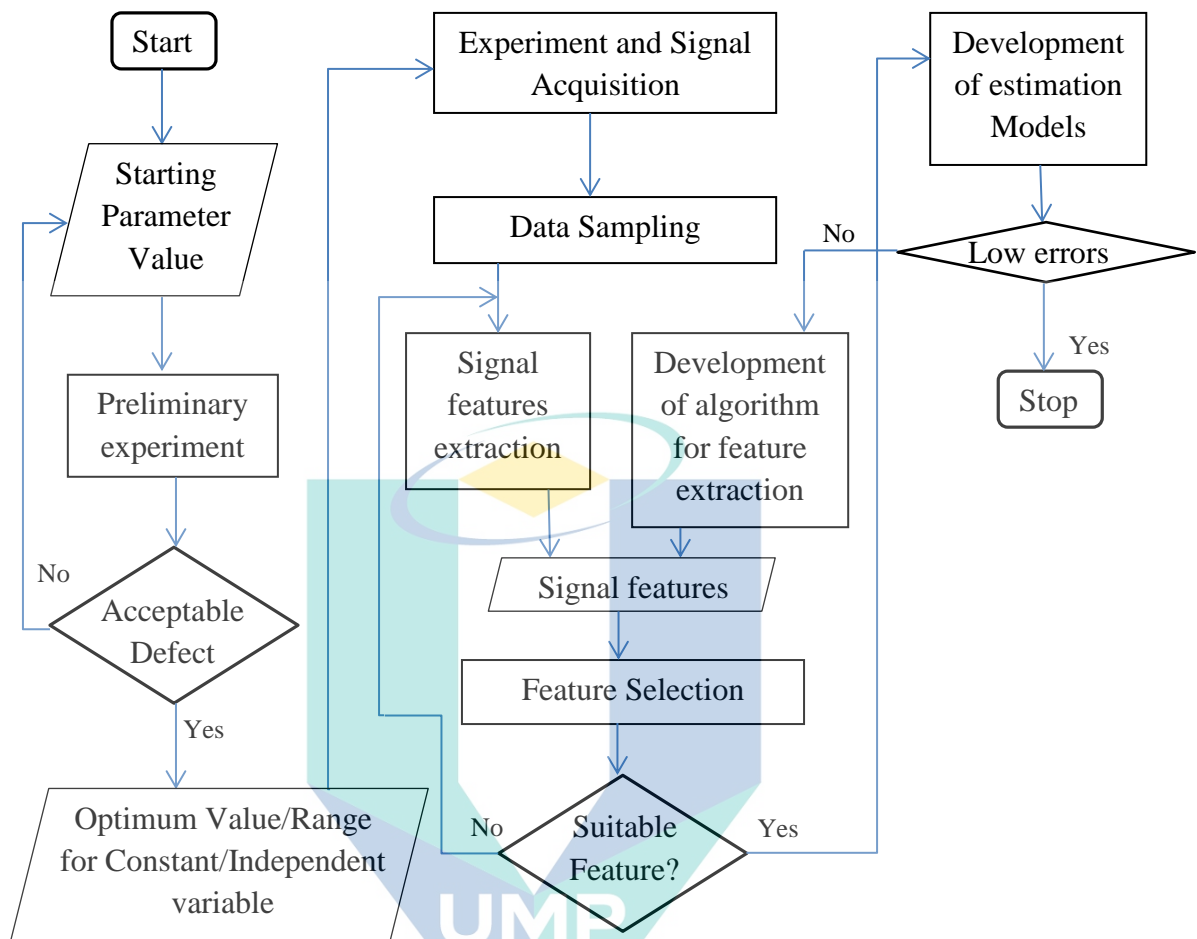
Figure 3.1   Process flow of the entire work in this study

3.2   Specimen Preparation

In this study, a 22MnB5 boron steel plate with a thickness of 1.8 mm and chemical composition as shown in Table 3.1 was used in the experiment. The selection was made because of its increasing demand for TWB fabrication in the automotive sector (Vaissiere, L. et al., 2002). The detail on the result of spectroscopy analysis was shown in Appendix B.

Table 3.1   Chemical Composition of 22MnB5 Boron Steel

Composition	Manufacturer Salzgitter FlachStahl (Max %)	Spectrometry Result (Average %)
C	0.19 ~ 0.25	0.249
Si	0.4	0.235
Mn	1.10 ~ 1.4	1.15
P	0.025	0.0092
S	0.015	0.003
Al	0.08	0.0765
N	0.01	0.005
Cr	0.03	0.147
B	0.0008 ~ 0.005	0.0028
Fe	Bal.	98.0

Before the experiment work, the specimen was cut into a size of 40 mm by 25 mm using the shear cutting method. Basically, the length of this specimen was decided according to the clamping jig size. Meanwhile, the width of specimen was set to 25 mm to give enough distance for the occurrence of inconsistent weld geometry due to the low absorptivity of laser beam initially cause by high temperature gradient, before the laser absorptivity becomes stable (Su, J. et al., 2019).

As shown in Figure 3.2, the surface of the specimen was ground using 240 grit sand paper. It was done to create a slightly rough surface, which could possibly reduce the amount of back-reflected laser and simultaneously increase laser energy absorptivity during the energy coupling process (Bergström, D., 2008; Kelkar, G., 2008). On the other hand, the side of the specimen was ground by the surface grinding process. It was performed to remove the shear cutting mark. Moreover, it was also done to ensure that the edge surface of the specimen was flat enough to obtain nearly zero gaps for butt joint welding in the experiment. Figure 3.3 shown the side view of the test specimen used in this study after underwent the surface grounding process.
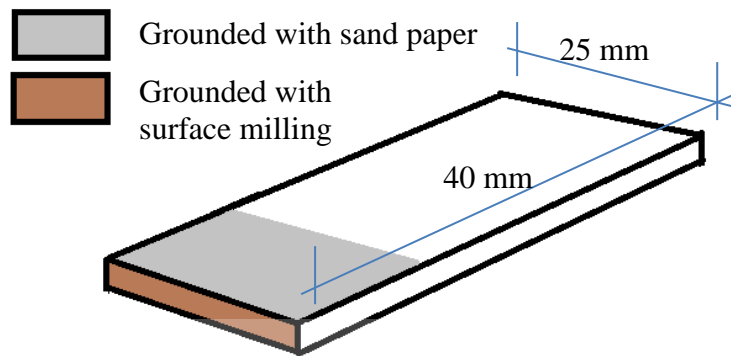
Figure 3.2   Illustration of the single-side of the test specimen

| (a) | (b) |
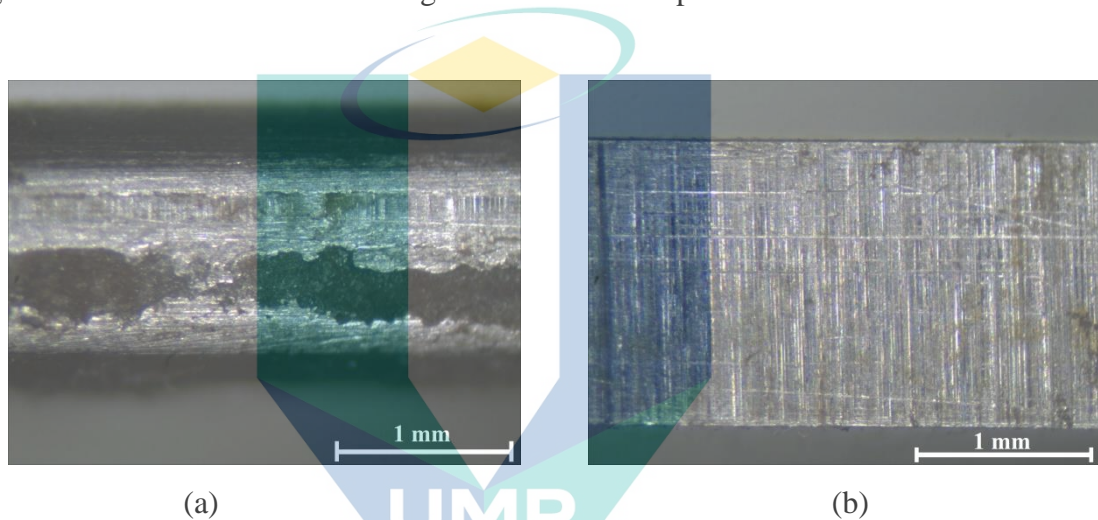
Figure 3.3   Image of the side surface of the specimen (a) Shear cutting mark before surface grounded (b) After surface grounding process.

3.3   Design of Experiment

Unlike continuous mode (CW), pulse mode (PW) laser welding involves more parameters. For this reason, focal length, weld speed, pulse repetition rate, and gas flowrate were set to be constant in this study. Meanwhile, laser peak power and pulse duration were set to be varied in their level. Both parameters were chosen as it have been proven to be significantly influenced the weld penetration in laser welding process (Assuncao, E. & Williams, S., 2013; Assuncao, E. et al., 2012). In order to identify the optimum value or range for these parameters, the preliminary experiment has been done. This part of work is crucial as it explained how the experiment was designed in this study. Therefore, important results from the preliminary experiment will be elaborated in this chapter to ensure that the selection of constant parameter values shown in Table 3.3 can be understood.

```
                    ┌──────────┐
                    │  Start   │
                    └────┬─────┘
                         │
                         ▼
              ┌─────────────────────┐
   ┌─────────▶│  Initial parameter  │
   │          │       values        │
   │          └─────────────────────┘
   │                     │
   │                     ▼
   │          ┌─────────────────────┐
   │  ┌──────▶│     Preliminary     │
   │  │       │     Experiment      │
   │  │       └─────────────────────┘
   │  │                  │
   │  │                  ▼
   │  │    No      ◇───────────◇
   │  └───────────◇  Acceptable  ◇
   │              ◇   defect?     ◇
   │               ◇───────────◇
   │                     │ Yes
   │                     ▼
   │          ┌─────────────────────┐
   │          │   Optimum range/    │
   │          │       values        │
   │          └─────────────────────┘
   │                     │
Iteration                ▼
   └───────────────┌──────────┐
                   │   Stop   │
                   └──────────┘
```
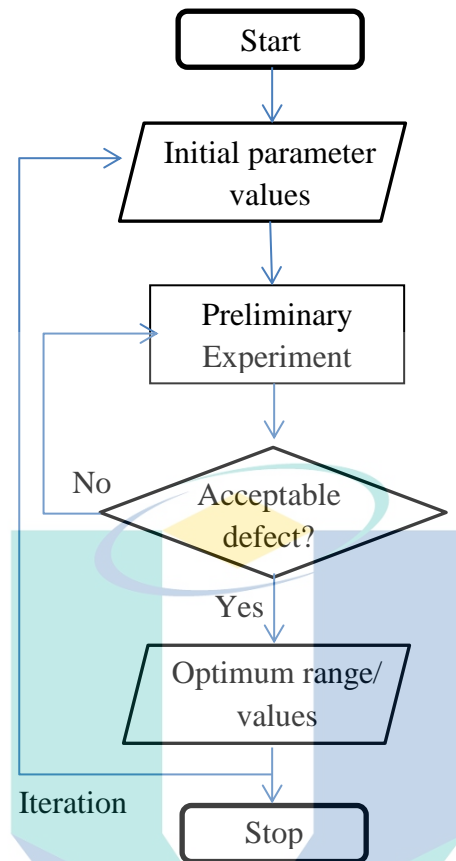
Figure 3.4   Process flow prior to the experiment setup

As illustrated in Figure 3.4, the bead-on-plate welding was performed with the initial values set for one selected parameter while the others were set to be constant. After the welding process completed, the quality of weld was check at the end of test. Defect such as crack and large underfill were the criteria to be determine in this study. If these defect occurred, the process will be repeated with increasing level of the tested parameter. This step iterates until the weld joint was free from crack and large underfill. ISO 13919-1 standard suggest that the underfill must be less than 20% from the thickness of the welded component at an intermediate qualitative level, and 10% at stringent qualitative level to avoid the degradation on the strength (Pakmanesh, M. R. & Shamanian, M., 2018). Hence the acceptable underfill size considered in this study was referred to this value. After the optimal value was identified, the process was repeated for other weld parameters. Beside the other constant parameters, the beam angle was also set in a stationary position. Specifically, it was set at 5° to avoid reflected laser beam from damaging both the lens and laser head (Farson, D. F. et al., 1999).

3.3.1   Focal Position

As briefly described in Section 3.3, the focal length was set in a fixed position in this study. The decision was made because the focal position will affect the laser beam size, which will simultaneously influence the laser energy density and cause several types of defects to occur at some point (Kaplan, A. F. H. & Powell, J., 2011). Bead on plate weld was performed in a wide range of focal length, laser peak power, and laser pulse duration in order to determine the optimum focal position. In this set of test, the laser peak power and pulse duration were set to 1200 W and 2 ms, respectively. This value was set to avoid burn-though defect in case of welding process at the focused point because excessive heat input tends to occur at this condition (Akman, E. et al., 2009; Katayama, S., 2013; Luo, Z. et al., 2016). Meanwhile, the argon gas flow rate was set to 15 L/min. This value was initially set to reduce the occurrence of undercut to the result (Dawes, C., 1992).

| (a) | (b) | (c) |
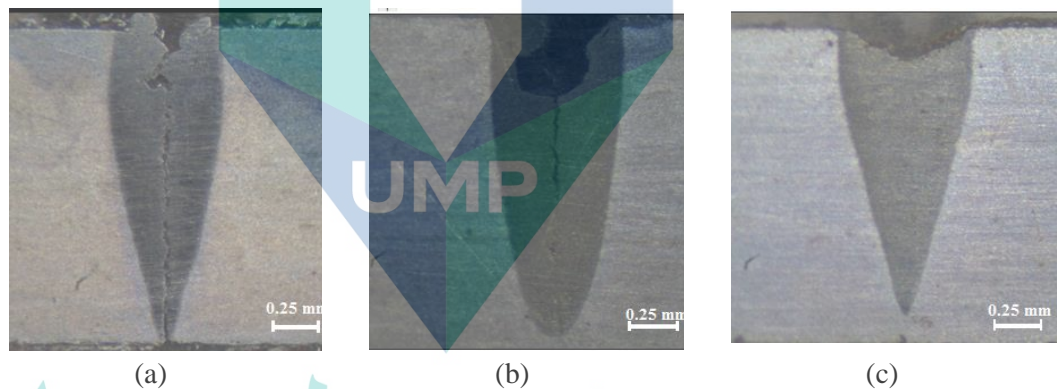
Figure 3.5   Images of weld cross section area at the process with different focal position (a) 0 mm (b) -5 mm (c) +5 mm

Figure 3.5 depicts the selected cross-section images of the welded specimen obtained from preliminary experiment. Based on Figure 3.5(a), it is clear that even though full penetration can be achieved as low as 60% of the maximum allowable laser peak power at the focus point, the quality of weld is unsatisfactory due to the occurrence of crack and a large amount of underfill. A similar pattern was observed during the welding process at -5 mm defocused position in Figure 3.5(b). In contrast, a good quality weld was recorded at +5 mm defocused position. This finding suggested that the optimum focal length for the experiment in this study was +5mm.

3.3.2   Weld Speed

Besides focal length, the weld speed was also set to be constant, and its optimum value for this study was obtained from the preliminary experiment. The reason behind this decision was due to the fact that the process with lower speeds commonly suffers from excessive heat input, which can lead to the occurrence of top concavity (Li, S. et al., 2015; Westerbaan, D. et al., 2014).

In investigating the optimum speed under the circumstances of the controlled experiment in this study, the maximum allowable speed at the lowest weld spot diameter was calculated using Equation 2.5. The lowest spot diameter was taken at the process with peak power and pulse duration of 1000 W and 1 ms, respectively. The lowest spot diameter was needed in the calculation to make sure that the pulse overlap of the welded joint does not less than its minimum allowable value during the real experiment. The minimum allowable pulse overlap was set to 80% according to Chmelíčková, H. & Šebestová, H.,(2012). Figure 3.6(a) shows that the spot size is 0.38 mm under the aforementioned process. Based on the calculation, the speed must not exceed 1.52 mm/s in order to obtain more than 80% pulse overlap for a hermitic seam.

On the other hand, the effect of weld speed of lower than 1.5 mm/s was also investigated in the preliminary experiment. Figure 3.6 (b) to (d) shows the cross-section image of weld bead at 1 mm/s, 1.25 mm/s and 1.5 mm/s process speed. During the test, the peak power and pulse duration was set to 1200 W and 2 ms, respectively. Based on the Figure 3.6, the quality of the weld bead surface seemed to reduce as the speed decreased. Larger underfill has been detected for lower speed due to the existence of large amount of spatter. Therefore, in this study, 1.5 mm/s was identified to be the optimum speed.
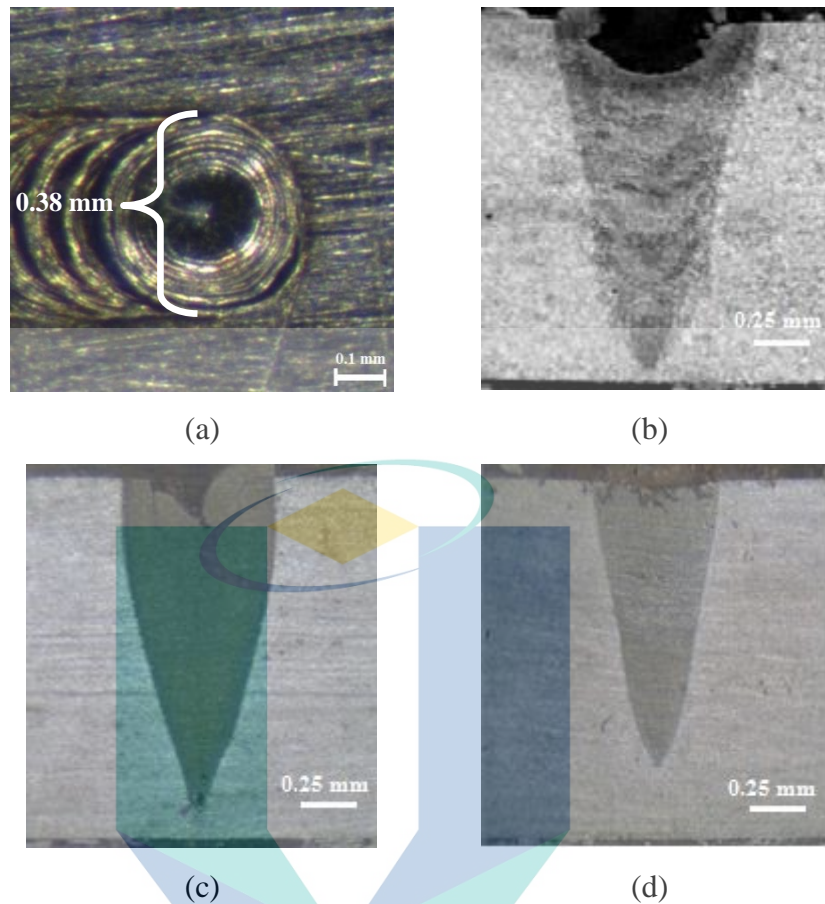
Figure 3.6   Minimum weld spot size and cross sectional image of weld quality at different speed (a) Weld spot size at 1000 W and 1 ms (b) Weld quality at speed of 1 mm/s (b) Weld quality at speed of 1.25 mm/s (c) Weld quality at speed of 1.5 mm/s

3.3.3   Pulse Repetition Rate

As the welding speed was set to be fixed in this study, the optimum PRR value was determined based on the trend of pulse overlap at the smallest spot diameter that could be obtained in this study. The reason was same with what have been explained in section 3.3.2, whereas it was done to ensure that the pulse overlap obtained from the real experiment was not less than 80% (Chmelíčková, H. & Šebestová, H., 2012). Moreover, this value was also found to be suitable to suppress the amount of porosity, as the pulse overlap needs to be set above 75% to reduce this type of defect (Gao, X.-L. et al., 2014).
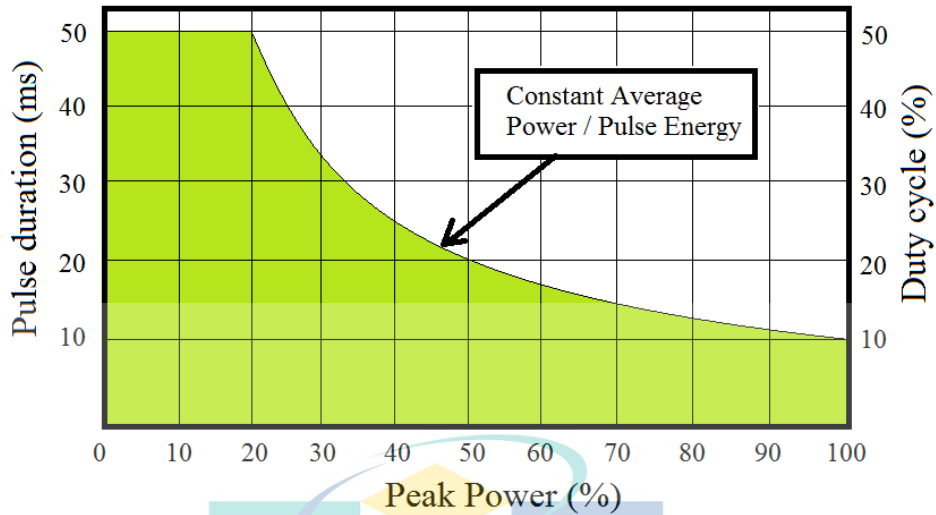
Figure 3.7   Laser Machine Specification

Source: IPG Photonics Manuals (2010)
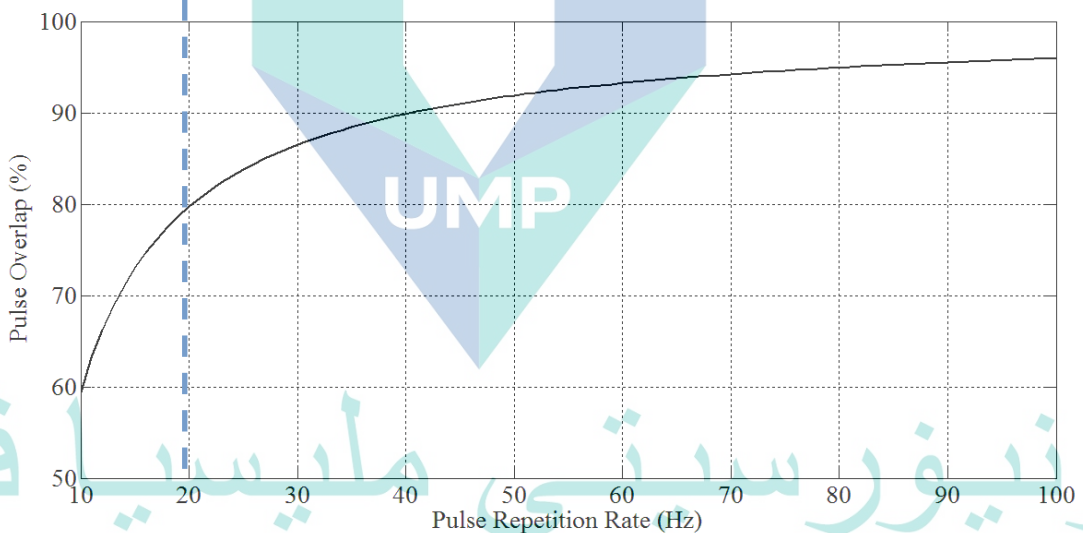
Figure 3.8   Variation of pulse overlap percentage according to the laser spot weld experiment with 1000 W Peak power and 1 ms pulse duration.

According to the specification chart shown in Figure 3.7, the pulse duration must not exceed 10 ms to allow the laser peak power to be extended to its maximum capability. As the lowest pulse duration could be set at 1 ms, the spot diameter was determined from the process with laser peak power and pulse duration of 1000 W and 1 ms, respectively. Figure 3.6(a) revealed that the spot diameter is 0.38 mm under this process condition. Based on this size, the variation in pulse overlap with different PRR

values is depicted in Figure 3.8. According to the figure, it is evident that the value of PRR must be at least 20 Hz in order to achieve more than 80% pulse overlap.

3.3.4 Argon Gas Flowrate

In the next part of the preliminary experiment, bead-on-plate PW laser welding was done with different gas flow rates. Specifically, pure argon gas was selected as it is an inert gas that does not react with metal during the process (Faerber, M., 1995), and the flow rate was set to be varied from 5 L/min to 25 L/min. As explained in Section 2.5, an inappropriate amount of shielding gas will cause spatter during the process, thus affecting weld quality (Li, S. C. et al., 2014). Therefore, the evaluation of result was made based on the amount of spatter (in response to the variation in gas flow rate).

Figure 3.9 represents the images of weld bead from the laser welding process with different shielding gas flow rates. By assuming that the spatter formation rate is constant along the process, the image was consistently zoomed for comparison. The spatter amount was qualitatively evaluated from the existence of a molten metal splattering mark within the set area. Based on the top view of the captured image, the amount of spatter was significantly reduced starting from the gas flow rate of 20 L/min.
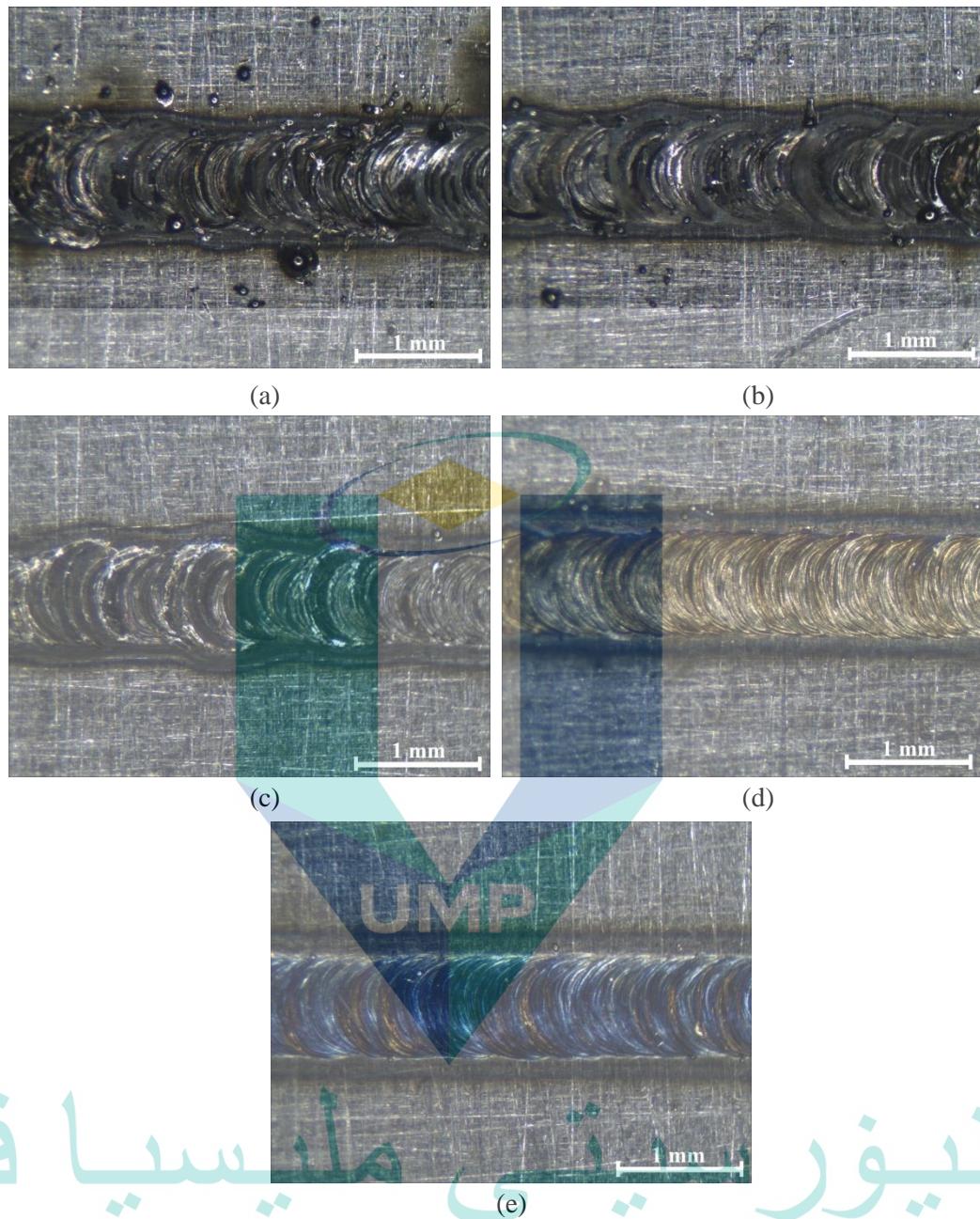
Figure 3.9   Weld bead image of weld sample produced from the process with different amount of gas flowrate (a) 5 L/min (b) 10 L/min (c) 15 L/min (d) 20 L/min (e) 25 L/min

3.3.5   Laser Peak Power and Pulse Duration Limit

On another set of preliminary experiment, a bead-on-plate weld was carried out to find out the highest value of pulse duration that can be set in the experiment. As shown in Figure 3.7, the laser peak power and pulse duration can be set to different levels up to the maximum capability. However, the combination of both parameters

must comply with the duty cycle value, which was shown in Equation 2.4. Based on Figure 3.7, the maximum limit of laser peak power can be reduced by increasing the laser pulse duration. Therefore, in this preliminary experiment, the tests were done by varying both laser peak power and pulse duration until full penetration was reached. This was done to identify the limit of pulse duration level in which full penetration could not be achieved even though the highest possible laser peak power was set.
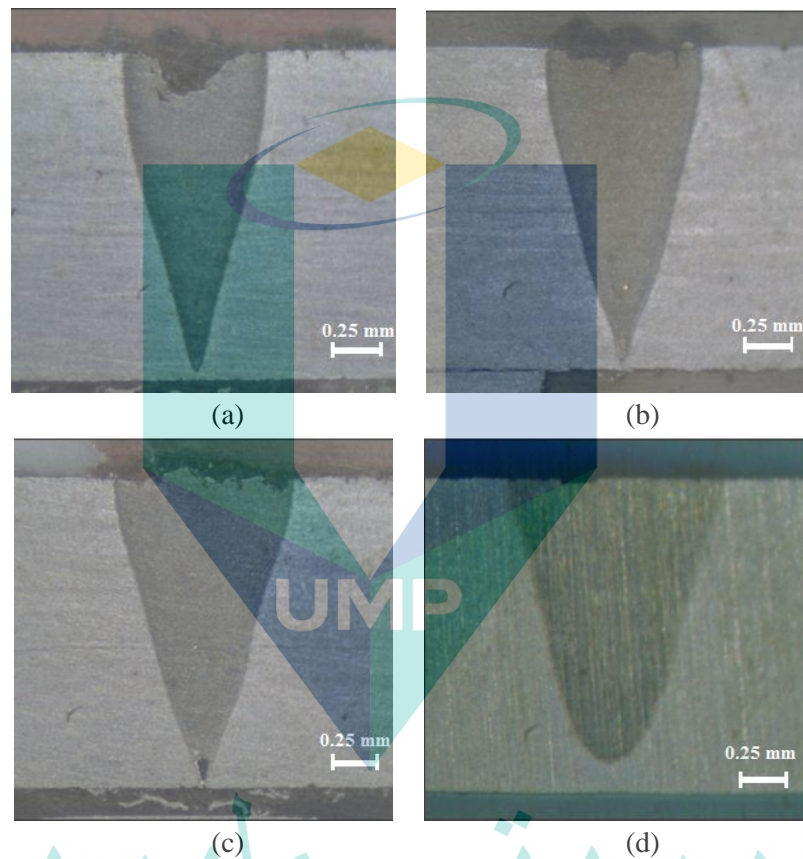
Figure 3.10   Cross-section images of bead-on-plate laser weld experiment with a variation of laser peak power and laser pulse duration (a) 1800 W and 2 ms (b) 1600 W and 4 ms (c) 1400W and 6ms (d) 1300W and 7 ms

Figure 3.10 shows the selected results from the four sets of experiments. Based on Figure 3.10(a), full penetration was achieved at laser peak power of 1800 W and pulse duration of 2 ms. However, at pulse duration of 4 ms, a lower laser peak power was needed to achieve full penetration, as shown in Figure 3.10(b). In this case, full penetration was achieved when the laser peak power was set to 1600 W. Meanwhile, as shown in Figure 3.10(c), at 6 ms laser pulse duration, only 1400 W laser peak power was needed to penetrate the workpiece fully. Unfortunately, at pulse duration of 7 ms, a

full penetration weld could not be obtained because the highest laser peak power could only be set at 1300 W before the machine was cut off at 1400 W laser peak power due to inappropriate duty cycle. Figure 3.10(d) depicts the cross-section image of the workpiece welded at laser peak power of 1300 W. These results show that the maximum pulse duration can be set in the real experiment was 6 ms. Meanwhile, there was no upper boundary for the laser peak power as it can be adjusted until full penetration weld achieved.

3.4 Experimental Setup

To establish the relation between the emitted sounds and weld depth, an experiment was set up according to Figure 3.11. The laser machine used in this experiment was IPG Photonics fiber laser, which can emit a laser at a wavelength of 1.06 µm. The average power for this particular laser welding machine is 200 W, but in the PW mode, the peak power can reach up to 2 kW.
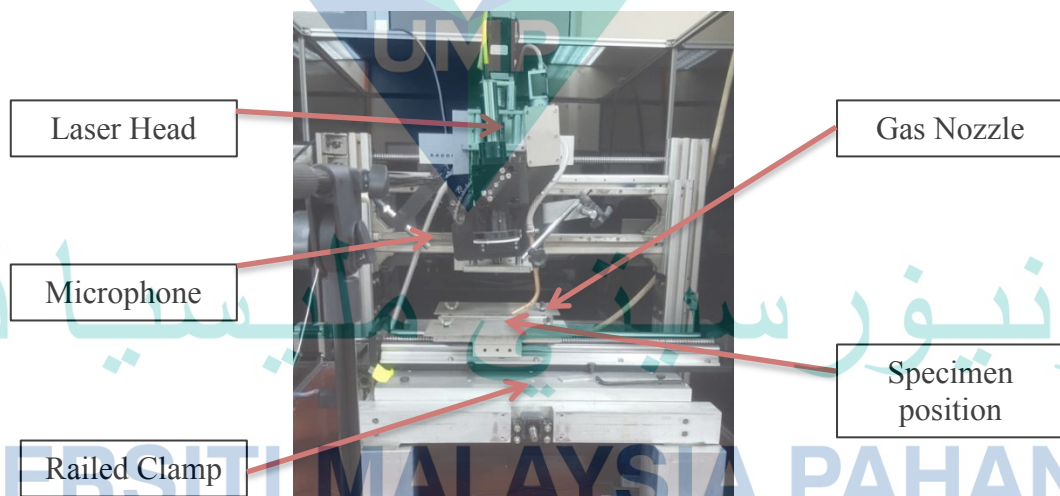
Figure 3.11   Experiment Setup

In this research, the levels of peak power and pulse duration were varied. Several literature lines also proved that these parameters have a major influence on weld geometry (Assuncao, E. & Williams, S., 2013; Assuncao, E. et al., 2012; Nath, A. K. et al., 2002; Ready, J. F. & Farson, D. F., 2001). Based on the preliminary test result, the varied levels of peak power and pulse duration were set as shown in Table 3.2. Basically, to collect all data for the development of an estimation model, each

experiment was repeated three times. Meanwhile, for the validation process, another set of experiment was conducted using the same set of parameters shown in Table 3.2

In the preliminary experiment, it was revealed that in the case of 2 ms pulse duration, a full penetration weld could be achieved at laser peak power of 1800 W. This was the reason why the upper boundary of laser peak power was set to 90% from its maximum limit in Table 3.2. Meanwhile, the laser pulse duration was set up to 6 ms because the maximum allowable laser peak power that could be set at 7 ms pulse duration was insufficient for a full penetration weld. These have been explained in detail in Section 3.3.5.

Table 3.2   Parameter variation for the experiment

Pulse duration (ms)	Laser Peak Power (W)	Pulse duration (ms)	Laser Peak Power (W)	Pulse duration (ms)	Laser Peak Power (W)
	600		600		600
	800		800		800
	1000		1000		1000
2	1200	4	1200	6	1200
	1400		1400		1400
	1600		1600		1600
	1800		1800		1800

On the other hand, other parameters were set to be constant during the entire process, as summarized from the preliminary experiment in Table 3.3. Based on the table, the focal angle was fixed at 5°. Meanwhile, the weld speed, argon gas flow rate, and pulse repetition rate were set to 1.5 mm/s, 20 L/min, and 20 Hz, respectively. These values were summarized from the preliminary experiment result elaborated in Section 3.3.

Table 3.3   Constant parameters for the entire experiments

Parameters	Value
Focal Angle	5^0
Weld Speed	1.5 mm/s
Pure Argon Gas Flowrate	20 L/min
Pulse Repetition Rate	20 Hz

3.5 Data Acquisition setup

In order to acquire the sound signal that emerges from the laser welding process, the data acquisition system is needed. Fundamentally, the data acquisition system consists of a sensor, an analog-to-digital converter, and also a digital signal analyzer, as illustrated in Figure 3.12 (Arbel, A. F., 1984). In this study, PCB piezotronics free-field microphone with TEDS preamplifier was used as a sensor. The sensitivity response over the operating frequency of this type of microphone can be referred from Table 3.4.
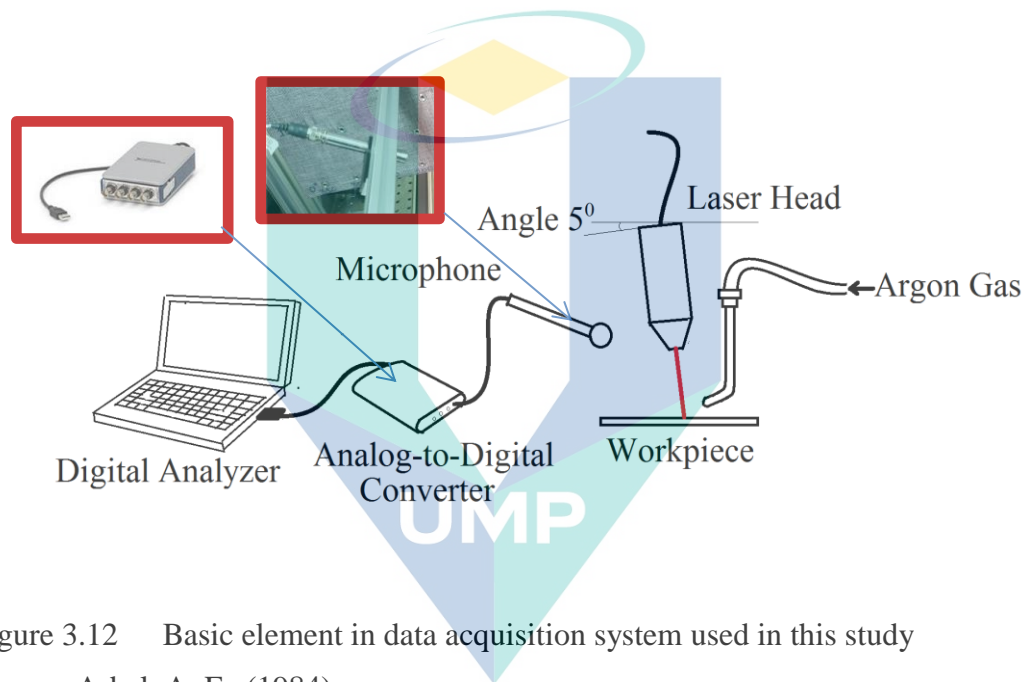
Figure 3.12   Basic element in data acquisition system used in this study

Source: Arbel, A. F., (1984)

Table 3.4   PCB 378B02 Microphone Specification

Specification	
Nominal Microphone Diameter	1/2" inches
Frequency Response Characteristic (at 0° incidence)	Free-Field
Sensitivity	50 mV/Pa
Inherent Noise	15.5 dB(A) re 20 µPa
Dynamic Range (3% Distortion Limit)	137 dB re 20 µPa
TEDS Compliant	Yes
Temperature Range (Operating)	-40 to +80 °C

 Source: PCB Piezotronics, (2016)

In this experiment, the microphone was attached in a fixed position to secure its distance from the laser-focused spot. The distance was set to 25 cm, whereas the angle was set to 30° from the horizontal plane. The decision was made based on the result from the signal-to-noise ratio (SNR) mapping around the laser machine, as depicted in Figure 3.13. On the other hand, this location was also found close to the previously reported works (Farson, D. F. & Kim, K. R., 1999; Huang, W. & Kovacevic, R., 2011). Basically, the mapping in the figure was obtained from the measurement through the concept of a roving microphone and laser welding process with peak power and pulse duration of 800 W and 2 ms, respectively.

(a)　　　　　　　　　　　　　　　　(b)
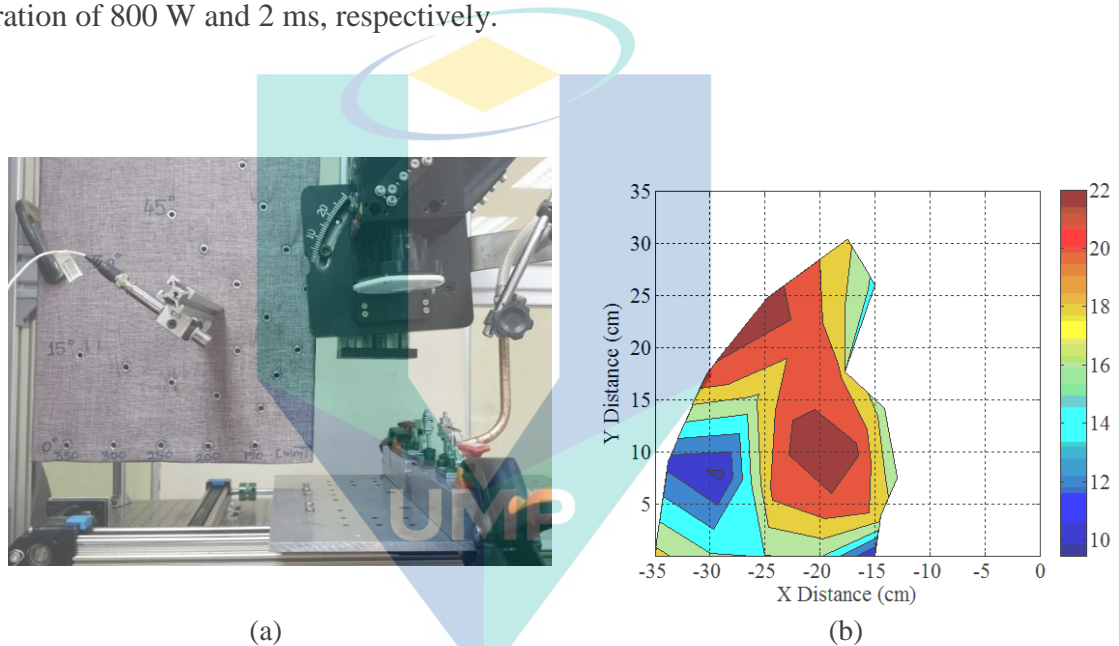
Figure 3.13　　Signal-to-noise ratio mapping test (a) test setup (b) signal-to-noise ratio mapping surround the laser weld machine

Once the microphone acquired the analog sound signal from the welding process, the signal was sent to an analog-to-digital converter for discretization and digitization processes. The National Instruments DAQ NI 9234 analog-to-digital converter was used for this purpose and its specifications are shown in Table 3.5. Based on Figure 3.14, the sound was initially acquired at the operating range of the microphone. Then, the signal was filtered from 20 Hz to 12.8 kHz using a bandpass digital filter. In this study, Butterworth filter has been applied to avoid the ripple effect as could occur in Chebyshev type (Bakshi, S. et al., 2019; Rabbi, N. F., 2021). Meanwhile, the filter order has been set to 8. This was done to sharpen the transition

region between passband to stopband in order to reduce the leakage (Kamen, E. W. & Heck, B. S., 2006).

The selection of this bandwidth was made because several literatures associated with the study of sound signals that emerged from laser welding of steel proved that the information with respect to penetration status lies within this range (Duley, W. W. & Mao, Y. L., 1994; Farson, D. et al., 1996; Huang, W. & Kovacevic, R., 2009). Moreover, the down-sampling process was done with a rate of 25,600 samples per second before the analysis was preceded. It was done to reduce the processing time, mainly in the frequency-based analysis.
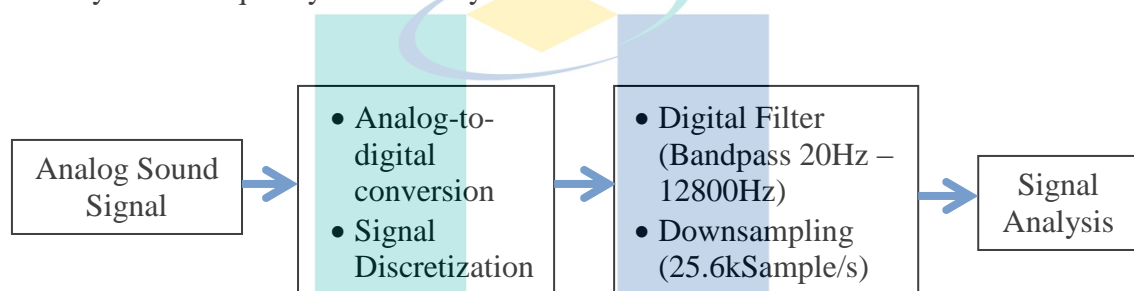
Figure 3.14   Signal processing flow prior to analysis stage

Table 3.5   National Instrument Analog-to-digital converter 9234

Specification	Value
Minimum Sampling Rate	1.652kS/s
Maximum Sampling Rate	51.2 kS/s
Input Range	±5V
Alias-free bandwidth	0.45fs

3.6   Data Collection

3.6.1   Data Sampling

As mentioned previously, the test parameters were set according to Table 3.2, and each experiment was repeated three times. For each specimen, the weld penetration data and sound signal were measured at five different locations, as depicted in Figure 3.15. It was done to ensure the consistency of penetration data which could be varies along the weld bead due to factors such as non-linear response of the process and machine persistency (Dawes, C., 1992; Lee, S. et al., 2014). As a result, there were 15

samples from all repeated sets of experiments, which gave a total of 195 samples from the entire experiment. In the previous study, Huang, W. & Kovacevic, R., (2011) successfully developed the predictive model to estimate the weld depth during CW laser welding process with 28 data samples. Therefore, the number of sample used in this study was predicted to be enough to obtain the reliable model.
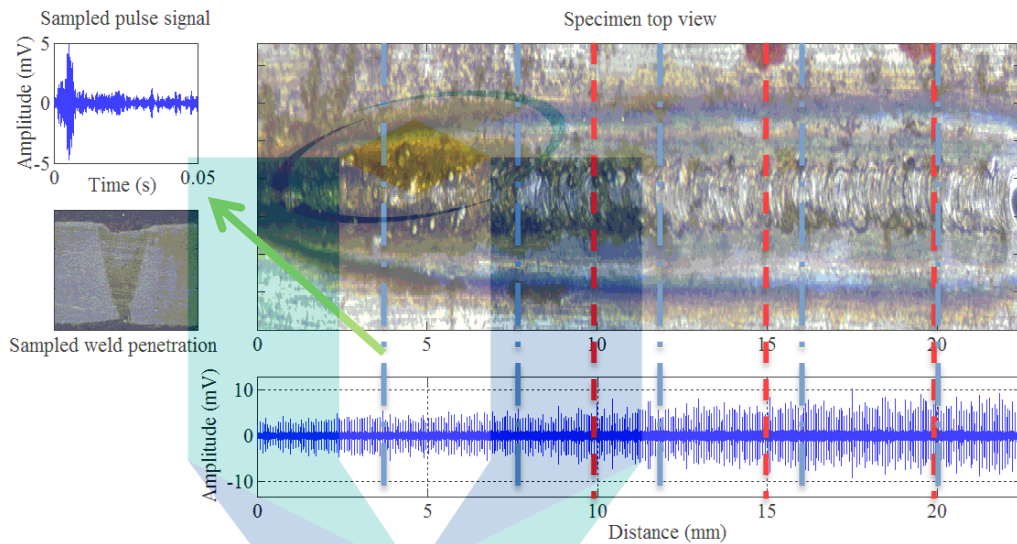
Figure 3.15   Data sampling from specimen

As explained in section 3.4, another set of experiments was conducted for model validation purposes. Unlike the 195 training samples, the penetration depth sample was taken at three different locations, as represented by the red line in Figure 3.15. This resulted in a total of 39 samples for weld depth estimation model validation. Basically, the different sampling locations provided some variations in the validation process as compared to the training dataset.

3.6.2   Macro graphic imaging

As explained previously, data sampling was done at different locations, and the depth of penetration was measured at a selected point on the specimen. In order to obtain the penetration data, each specimen was cut at the selected location using a sectioning cut-off machine. This cutting method was selected to achieve a precise cutting and avoid the heat effect (Lopes, J. C. et al., 2020).

After this process, the specimen was mounted using the cold mount technique before the polishing work was done. In this study, the polishing process was done using sandpaper by stepping up the grit level from 220 to 1000 as suggested in ASTM E3-11. Next, the etching process was carried out to reveal the fusion zone to measure penetration. The mounted specimen was dipped for several seconds into Nital solution with 3% nitric acid before it was cleaned using distilled water during the etching process. This procedure was based on the suggestion in ASTM E340-95. Meanwhile, the selection of etchant was made based on the previous studies which demonstrate the ability of the Nital solution to enhance the microstructural appearance in steel (Liu, Q. et al., 2018; Masoumi, M. et al., 2018). In the final step, the macro-imaging process and weld penetration measurement were logged using a microscope.

3.7 Feature Extraction Analysis

Commonly, the sound was characterized by its features trend to understand the mutual relation between the produced sound and the process condition. In this work, features were extracted from time-domain, frequency-domain, and time-frequency analyses. The feature trend extracted from these analyses was investigated before developing an algorithm for another feature extraction. In this section, the method of feature extraction will be explained in detail.

3.7.1 Time-domain feature extraction

In this work, mean absolute deviation (MAD), standard deviation (SD), and kurtosis shown by Equations 2.20 to 2.22 were extracted. The selection of these features was made because of their ability to give a significant correlation with weld condition in the case of laser and arc welding processes (Farson, D. et al., 1998; Fidali, M., 2018; Huang, W. & Kovacevic, R., 2009; Zhang, Z., Chen, H., et al., 2015).

Apart from those features, the L-scale and L-kurtosis were also extracted. Both features were determined based on the L-moment concept which has been explained in section 2.7.3. Several scholars have proven that this method was able to suppress the effect of sampling variability and outliers (Bao, W. et al., 2020; Gao, Q. et al., 2021; Hosking, J. R. M., 1990; Liu, H. & Shi, Z., 2020; Liu, S. et al., 2018). This was the reason of why these features were also investigated in this study.

The L-scale and L-kurtosis were determined by the L-moment ratio shown in Equation 2.24 and Equation 2.26, respectively. Meanwhile, the 1st, 2nd and 4th order L-moments which were represented as L_1, L_2 and L_4 in both equation were obtained by expanding the equation 2.23. The results of the equation 2.23 expansions were given in equation 3.1 to 3.3

$$L_1 = \frac{1}{n}\sum_{j=1}^{n} x_j \qquad\qquad 3.1$$

$$L_2 = 2\left(\frac{1}{n}\sum_{j=2}^{n} x_j\left[\frac{j-1}{n-1}\right]\right) - \left(\frac{1}{n}\sum_{j=1}^{n} x_j\right) \qquad\qquad 3.2$$

$$L_4 = 20\left(\frac{1}{n}\sum_{j=4}^{n} x_j\left[\frac{(j-1)(j-2)(j-3)}{(n-1)(n-2)(n-3)}\right]\right) - 30\left(\frac{1}{n}\sum_{j=3}^{n} x_j\left[\frac{(j-1)(j-2)}{(n-1)(n-2)}\right]\right) + 12\left(\frac{1}{n}\sum_{j=2}^{n} x_j\left[\frac{(j-1)}{(n-1)}\right]\right) - \left(\frac{1}{n}\sum_{j=1}^{n} x_j\right)$$
$$3.3$$

3.7.2 Frequency-domain feature extraction

In the frequency-domain approach, the bandpower was extracted from the power spectrum density of time-domain acoustic signal, as shown in Equation 3.4 (Jerbic, A. B. et al., 2015).

$$Band\ power = \sum_{f_i}^{f_f} PSD_{xi}(f) \qquad\qquad 3.4$$

In more detail, the bandpower was determined within the dominant frequency range from the first band, f_i, until the last band, f_f. In this study, f_i and f_f were set to 5960 Hz and 6440 Hz, respectively. These limits were set based on the interquartile range of the dominant frequencies of all the acquired sounds from the entire experiment.

The idea of using bandpower in this study was based on the previous finding, which proved that this type of feature can be used to develop the weld depth estimation model with reasonable errors (Huang, W. & Kovacevic, R., 2011). As these features were tested in the case of CW welding in previous work, the significant contribution of bandpower in PW laser welding was investigated in this study.

3.7.3   Time-Frequency features extraction

Besides the time- and frequency-domain analyses, the feature trend from time-frequency analysis was also investigated in this work. As discussed in Chapter 2, the time-frequency analysis of the acquired sound was revealed to be significant in monitoring weld penetration condition (Farson, D. et al., 1996) and detecting porosity (Sun, A. et al., 2001) during the laser welding process. This was the reason of the selection of time-frequency features in this study.

In this study, a feature of the time-frequency signal was extracted via the synchrosqueezed wavelet transform, which was recently developed (Daubechies, I. et al., 2011; Iatsenko, D. et al., 2015). Basically, synchrosqueezing provides a more concentrated representation in time-frequency space. It was done by joining the wavelet coefficients, $W_x(\omega, t)$ which was obtained from the equation 2.31, corresponding to the same phase velocity into one synchrosqueezed wavelet coefficient. The process began by extracting the instantaneous frequency, as described in Equation 3.5.

$$v_W(\omega, t) = \frac{\partial}{\partial t} \arg[W_x(\omega, t)] = Im\left[W_x^{-1}(\omega, t) \frac{\partial W_x(\omega, t)}{\partial t}\right] \qquad 3.5$$

Then, the synchrosqueezed wavelet coefficients were obtained from Equation 3.6,

$$T_x(\omega, t) = C_\varphi^{-1} \int_0^\infty \delta(\omega - v_W(\widetilde{\omega}, t)) W_x(\widetilde{\omega}, t) \frac{\partial \widetilde{\omega}}{\widetilde{\omega}} \qquad 3.6$$

whereas $C\varphi$ was acquired from Equation 3.7

$$C_\varphi = \frac{1}{2} \int_0^\infty \hat{\varphi}^*(\omega) \frac{\partial \omega}{\omega} \qquad 3.7$$

In this study, the feature for the wavelet analyses were presented in cumulative form in which all coefficients from the variation in time (but at a specific frequency) were accumulated together, as shown in Equation 3.8. In the equation, t_1 represents the time corresponding to the first data point, while t_N represents the time for the last data point from each signal.

$$CSqWC(\omega) = \sum_{t_1}^{t_N} T_x(\omega, t) \qquad 3.8$$

Meanwhile, to extract the feature, the sum of $CSqWC(\omega)$ along the specific frequency range was calculated, as shown in Equation 3.9. The summation only considered the frequency region, where the amplitude at the corresponding frequency exceeded the threshold λ.

$$CSqWC_{sum} = \sum_{\omega_i \leq \lambda \leq \omega_f} CSqWC(\omega) \qquad 3.9$$

As shown in Equation 3.10, the threshold was determined according to the maximum value of the cumulative synchrosqueezed wavelet coefficient (CSqWC) and the signal-to-noise ratio (SNR).

$$\lambda = max[CSqWC(\omega)]\left[\frac{1}{SNR}\right] \qquad 3.10$$

3.8   Development of algorithm for feature extraction.

In this work, the algorithm for feature extraction was developed by adopting the multi-lag phase space (MPLS) method. The reason behind the selection of this method was because of it have been claimed to be sensitive in detecting any shift in both amplitude and frequency (Digulescu, A. et al., 2019; Rosu, G. et al., 2018). Moreover, the algorithm was also simple, fast and less complex (Bernard, C. et al., 2014). However, to specifically implement this method for this work, several challenges were identified. Therefore, some modifications were made to the original algorithm to increase the capability of this method.

The entire modified MLPS algorithm was summarize in the flowchart in Figure 3.16. Based on the flowchart, the process begins with the acquisition of the time-series signal as an input to the entire program. This signal can be represented by Equation 3.11, where *i* and *n* are the *ith* sample and the total number of samples, respectively.

$$x = x_1, x_2, x_3, ..., x_{ti}, x_{tn} \qquad 3.11$$
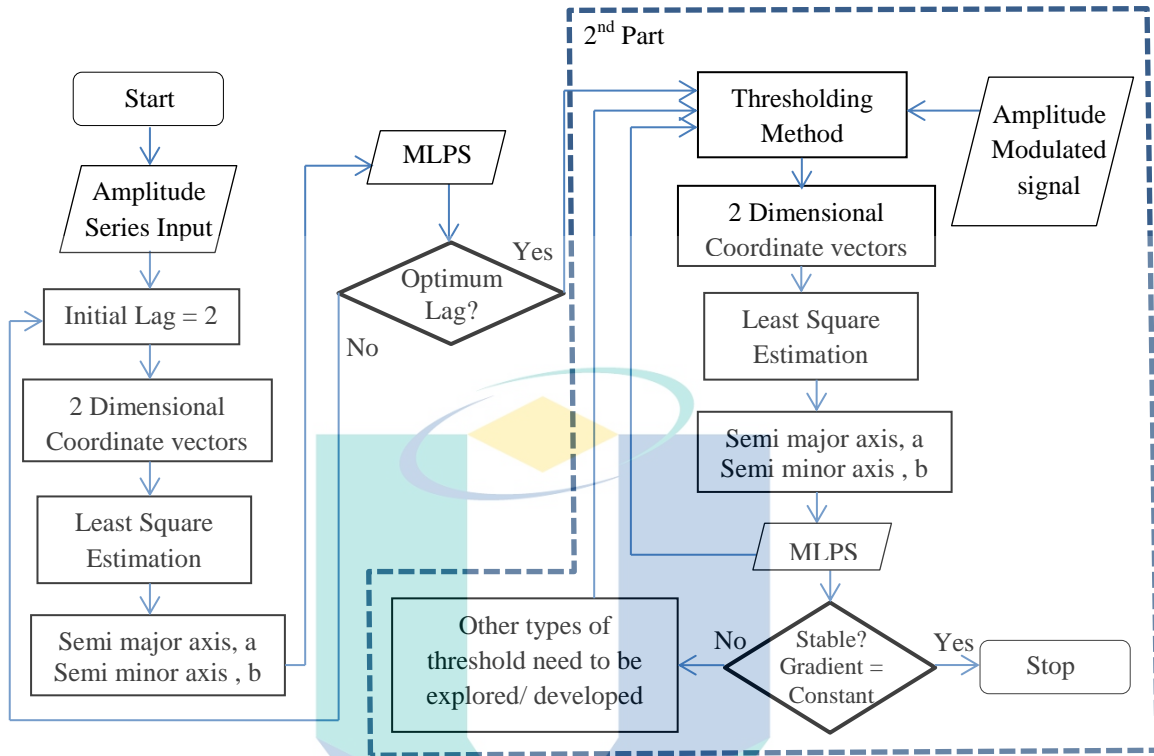
Figure 3.16   Flowchart of the modified MLPS algorithm development

In the next process, initial lag value was set to proceed with the signal division and MLPS computation. Specifically, the initial lag value was set to 2. Moreover, the signal division was done by dividing the signal into M_{th} dimension of coordinate vectors. In this particular study, only 2 dimensional coordinate vectors were considered. This was due to reduce the complexity and processing time of the entire analysis (Digulescu, A. et al., 2016). The obtained coordinate vector from this process was represent in equation 3.12 where v_j, m, τ and $\overrightarrow{M}$ are the phase space vector, dimension of phase space, lag between the sample, and total dimension of phase space, respectively (Bernard, C. et al., 2014).

$$\overrightarrow{v_j} = \sum_{k=1}^{m} x[j + (k-1)\tau] \qquad j = \overrightarrow{1, M}, M = n - (m-1)\tau \qquad 3.12$$

Basically, plotting this vector in the phase space gives a trajectory of the system, as shown in Figure 3.17(b). From this plot, the ellipsoidal model was computed based on Equation 3.13.
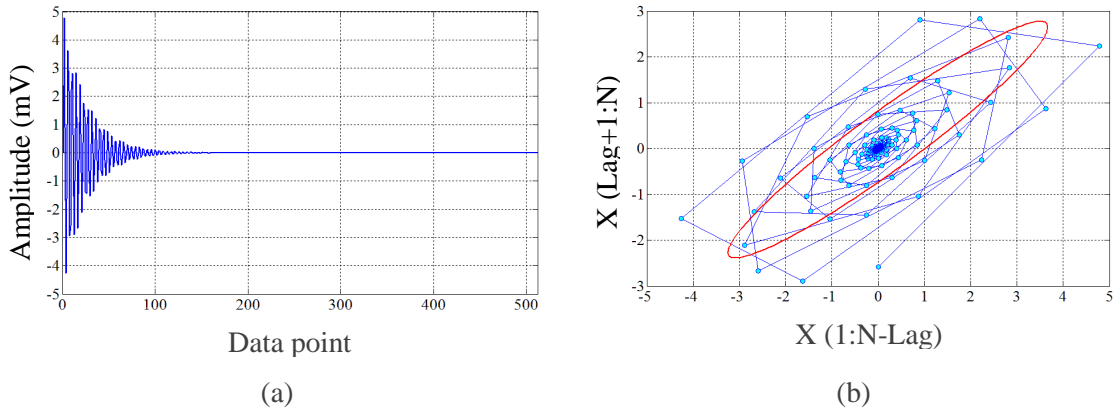
Figure 3.17   Fundamental concept of multi-lag phase space from a transient signal (a) example of transient signal (b) multi-lag phase space with a lag of sixteen data points

$$S = \sum_{j=1}^{m}[F(x_j y_j)]^2 \qquad where \quad F(x,y) = \Gamma^2 + \Lambda^2 + 1 \qquad 3.13$$

The least squares estimation method was applied to determine $1/\sqrt{\Lambda}$ and $1/\sqrt{\Gamma}$ in equation 3.13. As a result, the value of semi-major axis a and semi-minor axis b was obtained to determine the MPLS, which was the area of ellipsoidal. According to the flowchart in Figure 3.16, this process was iterated by increasing the lag number by the scale of 2 until the maximum MLPS value was achieved.

The second part in the flowchart in Figure 3.16 was the vital part as this is the point where the modification of the original MLPS algorithm was done. As explained earlier, the phase space was obtained from the ellipsoidal fitting using the least squares estimation method. Based on the phase space plot in Figure 3.17(b), it is clear that the amount of data point scattered at the center of the ellipsoid in the phase space plot influences the least squares estimation process. Consequently, the smaller values of both semi-minor and semi-major axes were obtained, resulting in a smaller ellipsoid area. Therefore, the modification was done to optimize the fitted ellipsoid size in the phase space. This is important because the peak of the transient sound signal acquired from PW laser welding is located around the maximum and minimum points in the phase space.

Based on the 2nd part of the flowchart in Figure 3.16, the modification was done by adding the thresholding method into the process. In this study, Sqtwolog, Rigrsure,

and Minimaxi thresholding methods shown in equation 2.13, 2.18, and 2.19 was used. The use of these types of thresholding techniques was due to its simplicity and good denoising effect (He, C. et al., 2015). On the other hand, (Verma, N. & Verma, A. K., (2012) claimed that SURE method was giving the poor performance in case of high signal-to-noise ratio signals such as in transient signal. Therefore, Heursure method was not considered in this study.

Besides the aforementioned thresholding method, other thresholding method was also proposed in this study. Specifically, this method was developed on the basis of the crest factor (CF) in a statistical study. In the analysis of a waveform, CF is a parameter that measures how extreme the peak is in the signal. This parameter can be obtained from Equation 3.14 (Jones, M., 2013)

$$Crest\ Factor = \frac{|x_{max}|}{rms\ (x)} \qquad 3.14$$

In this study, by adopting the CF theory, the localized CF was determined using Equation 3.15. By determining the localized crest factor, CF_{loc}, the local region, where the amplitude point was above the signal energy average, was able to be identified. This can offer an adaptive way to de-noise a signal as the value depends on the ratio between local peak and the overall energy.

$$CF_{loc} = \frac{|x_i|}{rms\ (x)} \qquad 3.15$$

In this research, the transient part in the time-domain signal was significant as it contained valuable information with respect to the weld condition. Due to this reason, the hard thresholding method was implemented by eliminating the part of the signal that recorded CF_{loc} of less than 2.

$$\lambda_{CF} = x(CF_{loc\ i} > 2) \qquad 3.16$$

Specifically, the selection of this value was made on the basis of z-score. As depicted in Figure 3.18, in transient-type signal, most of the noise amplitudes illustrated in red-shaded area were scattered within the 95% confidence interval of the amplitude distribution. Meanwhile, z-score value at 95% confident interval is approximately close

to 2 (Hazra, A., 2017). By comparing the z-score in Equation 3.17 and Crest Factor in Equation 3.14, it was notable that the Crest Factor only ignored the mean, μ in its equation. Considering that the signal acquired in this study had an approximately zero-mean, the CF was assumed to be equal to z-score.

$$Z-score = \frac{x_i - \mu}{\sigma} \qquad 3.17$$
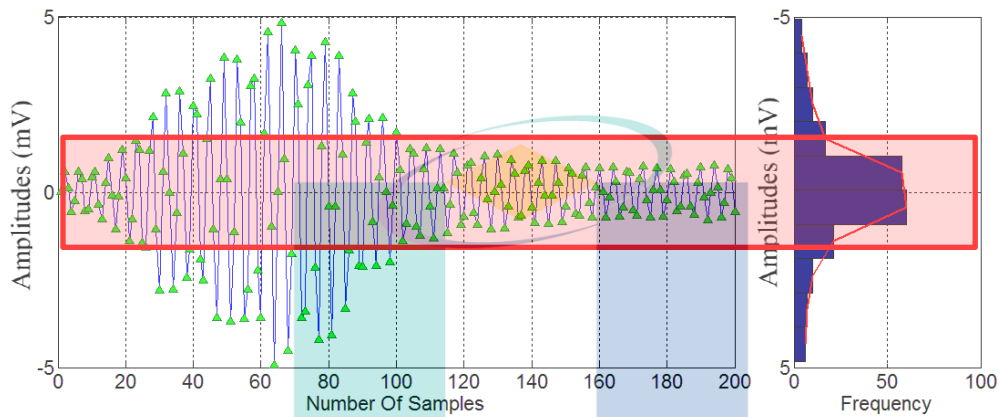
Figure 3.18   Noise amplitude distribution in transient signal

In order to select the best thresholding method, the MLPS value was computed using the simulated signal. The simulated signal was basically the amplitude-modulated transient signal in which its amplitude was increase from 4.6 to 5 with an increment of 0.01. The selection criterion was the stability of the MLPS value with respect to the change of simulated signal amplitude. In order to determine the stability of the threshold, the gradient of the MLPS must be constant. This is because the constant gradient indicates the constant rate of change of MLPS value in response to the uniform increment of the signal amplitude.

3.9   Feature Selection Analysis

Among all type of extracted sound features explained in section 3.8, only several number of feature might be suitable for predictive model. In order to identify the suitable signal features for the prediction model, the stepwise regression was done in this study. This is essential to ensure the generated model is not underfit or overfit and takes the shortest processing time for training (Babyak, M. A., 2004).

In principle, stepwise regression was carried out by finding the relation between predictive variables, which gives a better fit to the response or output (Efroymson, M., 1960). As illustrated in Figure 3.19, the algorithm automatically finds a linear, cross-relation, or higher order relation of variables that are more significant to the response, and the process iterates until the criteria reach the desired value.
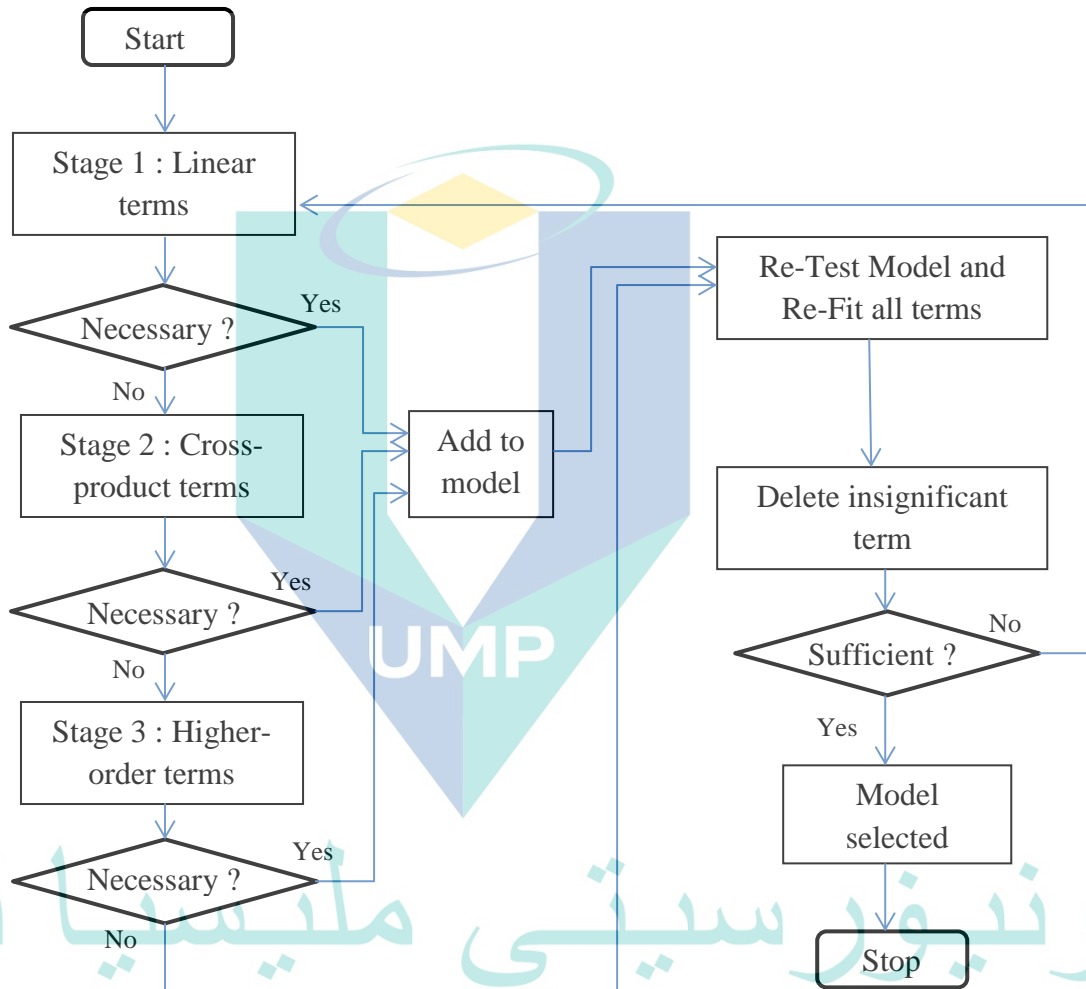
Figure 3.19   Flow chart of stepwise regression analysis
Source: Efroymson, M., (1960)

In this particular work, the backward-selection process was selected. The iteration started by considering all sound features and eventually rejecting features that were insignificant to the overall regression model. The rejection of features was done based on the absolute value of t-stats. Theoretically, a t-stat is obtained from the t-test, which measures the significance of each regression coefficient from each predictive

variable individually. It was determined from Equation 3.18, where $\hat{\beta}$ and $s.e(\hat{\beta})$ are the regression coefficient and standard error, respectively.

$$t_{\hat{\beta}} = \frac{\hat{\beta}}{s.e(\hat{\beta})} \qquad 3.18$$

Fundamentally, t-stats is the measure of the likelihood that the actual is not equal to zero, which indicates the significance of the predictive variable in the regression model (Montgomery, D. C. et al., 2012). Therefore, the selection of predictive variables in stepwise regression analysis was made based on the larger absolute value of t-stats. Meanwhile, the iteration stopping criterion was the root-mean-square error of the overall model, which considered all selected features.

3.10 Development of Depth of Penetration Estimation Model

3.10.1 Multiple Linear Regression Method

In this study, the development of weld depth estimation model involved several predictive variables from both sound features and weld parameters. Through multiple linear regression (MLR) method, the weld depth estimation model was generated using a general model shown in Equation 3.19 (Olive, D. J., 2017).

$$DOP = \beta_0 + \beta_1 x_1 + \beta_2 x_2 + \cdots + \beta_n x_n \qquad 3.19$$

In Equation 3.19, n is a series of predictive variables from both sound features and weld parameters selected based on the feature selection analysis result. β_0 is the intercept of multi-dimensional surface, while β_n is a series of partial regression coefficients. These coefficients were obtained from the least squares estimation method (Montgomery, D. C. & Runger, G. C., 2014) as shown in equation 2.33 to 2.35.

3.10.2 Artificial Neural Network Method

Apart from the MLR method, this study also applied the artificial neural network (ANN) method to develop the estimation model. Similar with the MLR method, it involves *n* input parameters, which have been analyzed to train the neural model. The overall process flow is illustrated in Figure 3.20.
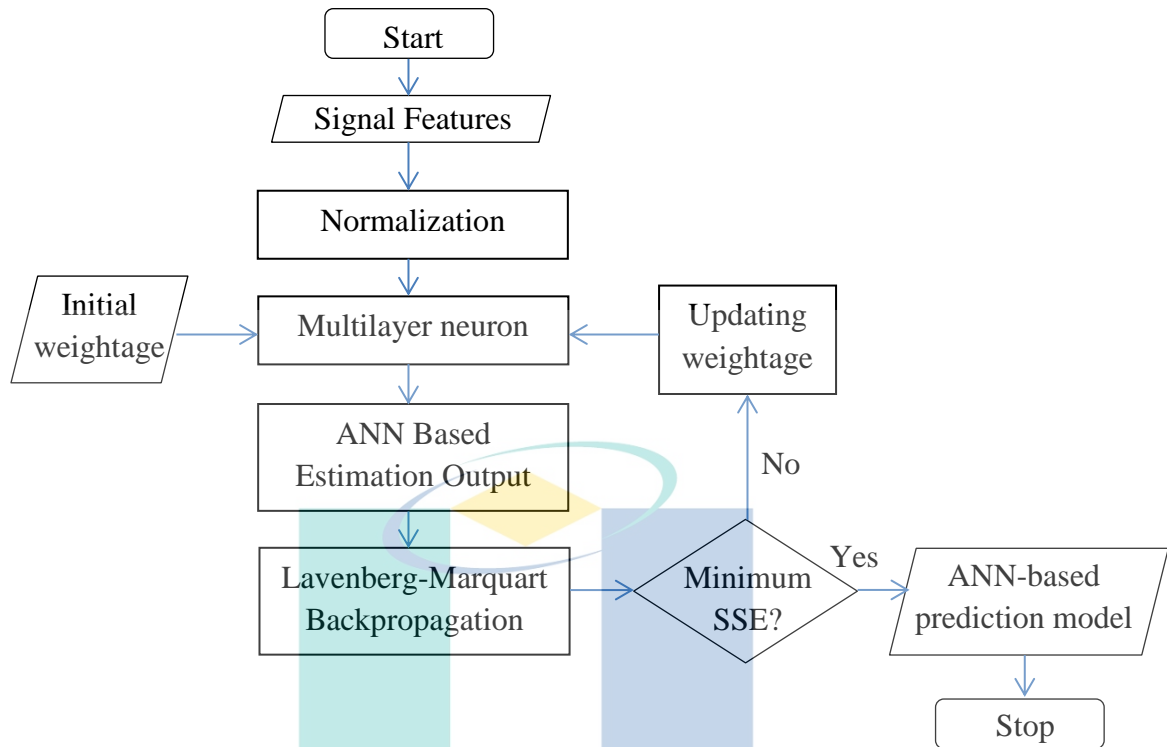
Figure 3.20   Neural Network model development process flow

According to the flowchart in Figure 3.20, prior to the neural model development, all the input and output data were normalized. This pre-processing technique is important to ensure that the difference in each input range value does not affect the entire trend learning (Gupta, A. et al.; Huang, W. & Kovacevic, R., 2011; Zhang, T. & You, X., 2015). In this particular study, the min-max technique was implemented due to its advantages in offering less time, and space and algorithm complexities (Chen, L. et al., 2018). Through this technique, both inputs and output were normalized to ensure they ranged from -1 to 1. This was done using Equation 2.38 as explained in Section 2.7.4.

After the normalization process, multilayer neuron was formed. In this study, three layers, which consisted of input, hidden, and output layers, were used. Meanwhile, the selected transfer functions for the hidden and output layers were tansig and pure linear, respectively. The number of neurons in the hidden layer was varied from 5 to 25 to investigate their effects on the estimation error. In the neural model development, 70% out of the 195 samples were randomly selected for training, and 15% each for model validation and testing. The network was trained using the Levenberg-Marquardt backpropagation method by following the computational process as shown from

99

equation 2.39 to 2.41. The use of this method was due to its adaptive behavior (Marquardt, D. W., 1963).

3.11 Methodology Summary

As a summary, the overall work which inclusive of several important stages was illustrated in Figure 3.21. The first stage of the entire work involved specimen preparation for the experiment. Then, a preliminary experiment was done to determine the range of weld parameter level and the optimum values for some constant parameters. Experiment work was carried out in the next stage, and the signal acquisition process was executed simultaneously. Thereafter, data collection and feature extraction analysis were done before feature selection analyses were performed. Finally, work comprising the estimation model development and model validation process was conducted.
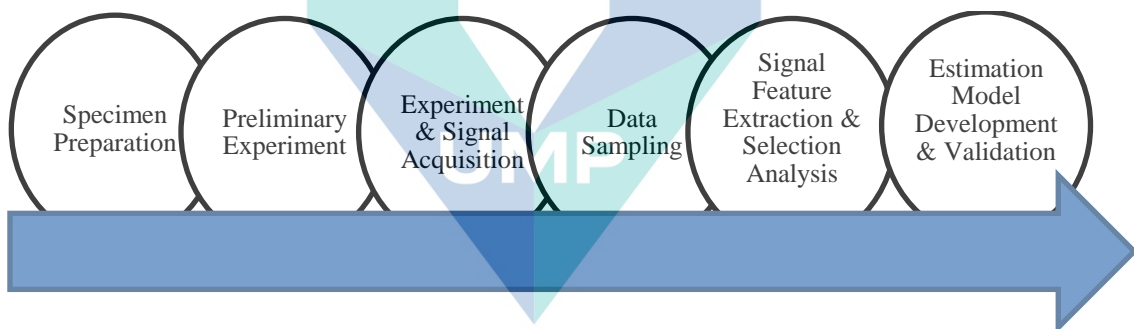
Figure 3.21   Process flow of the entire work.

CHAPTER 4

RESULTS AND DISCUSSION

4.1   Introduction

The first objective of this work aims to investigate the behavior of the acquired sound from PW laser welding. Previously, much work was done to gain a deeper comprehension of how the emerged sound signal from laser welding can characterize the penetration condition. However, studies involving PW laser welding in the aforesaid research were lacking in number until recently. As non-stationary random sound signal can emerge from this type of laser welding process according to its physical mechanism, it is essential to investigate how the sound captured from this process can characterize weld penetration. Therefore, in the first part of this chapter, the trend of time series and frequency spectrum acquired from the process with different peak power levels and pulse durations will be presented and discussed in detail.

Apart from the need for comprehensive information on sound behavior from the PW laser process, there are other obstacles in applying the sound methods in weld condition monitoring. Basically, the major drawback of the acoustic methods is the influence of noise that emerges from harsh surroundings, making it difficult to characterize the sound features according to the weld condition. Therefore, the development of both noise elimination and feature extraction methods either simultaneously or implicitly, is important to improve the efficiency of the methods. In the second part of this chapter, the work will be highlighted on the development of an algorithm for noise elimination and feature extraction. The significance of the features extracted from the developed algorithm will be discussed based on the results of feature selection analysis.

In the last part of this chapter, the focus of discussion will be more toward the results from work related to the weld penetration estimation model development. Basically, the work associated with the model development based on the sound feature or predictive variable trend learning will be presented and discussed in detail. This part

will reflect the final objective of this work. Moreover, the efficiency of the developed estimated model and the result from the validation experiment will be discussed.

4.2   Effect of Peak Power and Pulse duration to Weld Penetration

Chapter 3 explained that a test was carried out with variation in laser peak power and pulse duration, as shown in Table 3.2. Figure 4.1 depicts the selected cross-section image of the welded sample from each weld parameter setup. According to the figure, it was found that there was no joining that occurred at the laser peak power of 600 W for the case of 2 ms and 4 ms pulse durations. Meanwhile, the weld joint reached full penetration when the peak power was set to 1600W, 1400 W and 1200W for the process with pulse durations of 2 ms, 4 ms and 6 ms.

Based on the results, to achieve full penetration, the amount of pulse duration influenced the limit of peak power. Smaller pulse durations needed higher laser peak power levels to achieve full penetration weld. Apart from inducing penetration depth, the amount of pulse duration also affected the width of the fusion zone. On the other hand, at a constant pulse duration, higher peak power levels gave deeper penetrations. The variation of weld penetration with different laser peak power levels and pulse durations was plotted in Figure 4.2.
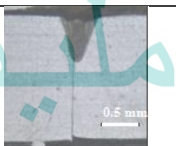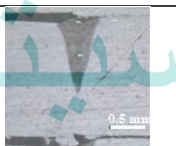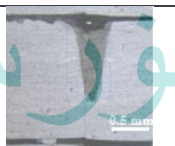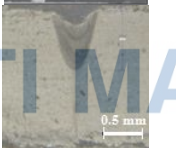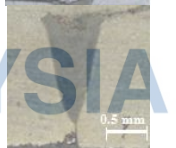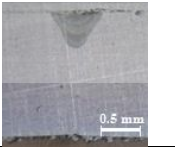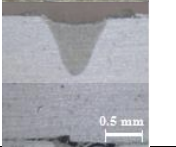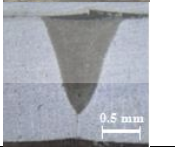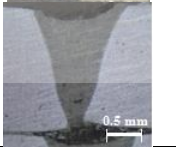
Pulse	Peak Power (W)					
duration	600	800	1000	1200	1400	1600
2 ms	Not Joined					
4 ms	Not Joined					-
6 ms					-	-

Figure 4.1   Selected cross-section image of the welded sample from each of the weld parameter setup

102
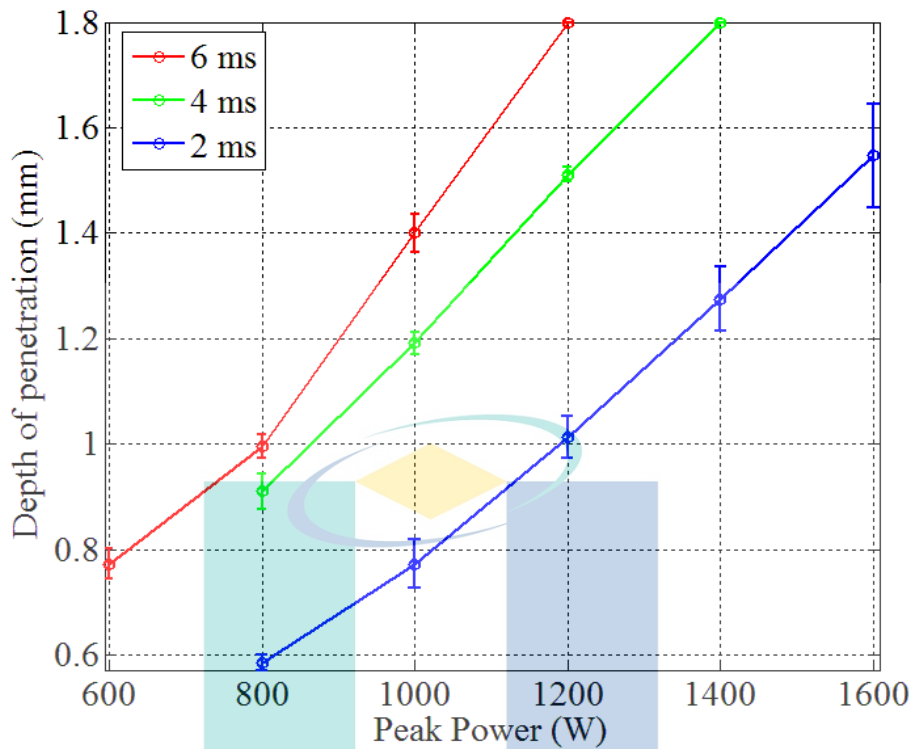
Figure 4.2   Weld depth variations from different peak power and pulse duration

In this study, laser beam energy density leaned wholly on laser peak power and pulse duration due to the fixed focal position on the entire experiment. Results presented previously showed that laser peak power and pulse duration greatly influenced the penetration depth. This trend shows good agreement with what has been explained in the previous chapter. Based on the theoretical explanation in Chapter 2, it can be summarized that establishing coupling and melting is strongly related to the amount of absorbed laser energy. Higher laser beam energy densities allow deeper penetrations (Bergström, D., 2008; Kelkar, G., 2008). On the other hand, (Yaakob, K. et al., (2017) in their study, revealed the similar finding whereas the weld penetration was reported to be influence by both peak power and pulse duration.

4.3   Effect of the Peak Power and Pulse duration to the characteristic of the Acquired Sound Signal

Besides the variation in weld penetration, it is also important to observe the characteristics of the sound signal acquired from the PW laser welding and how it reacts with the variation in welding parameters. This is essential to gain a deeper

understanding of how the sound characteristic dynamically changes with the change in penetration depth before the estimation model is developed later on. In this section, the characteristics of time and frequency domains of the acquired sound signal will be presented. Moreover, the trend of the sound pressure level (SPL) against the variation in peak power and pulse duration will be elaborated in detail.

Similar to the trend in this study, earlier studies explained that peak amplitude that appeared in the acquired sound signal could indicate the formation of a plasma plume (Hoffman, J. et al., 2002; Lewis, G. & Dixon, R., 1985; Szymanski, Z. et al., 2000). A higher number of peaks indicate a larger amount of plasma plume formation, which is directly related to the laser pulse duration and peak power. With regard to the effect of peak power variation in Figure 4.3, an increasing trend of sound pressure amplitudes was displayed in this study. However, the amplitude increment rate was quite weak, making it slightly challenging to characterize the sound amplitude in response to peak power increment. For example, by comparing the acquired sound at peak power levels of 600 W and 800 W, it was found that the overall amplitudes of both signals were nearly 3 Pa. In contrast, a different trend was noted when the sound pulses acquired from the welding process with peak power levels of 1000 W and 1200 W were compared. When the laser welding process was performed with a peak power of 1000 W, the overall amplitude of sound pulse approached 4 Pa, and only several points surpassed the value. Sound amplitudes that exceeded 4 Pa were increased during the welding process with a peak power of 1200 W. On the other hand, comparison between the signals from the process with different laser pulse duration in Figure 4.4 showed that both amplitudes and duration of the sound pulse increase as the pulse duration increased.
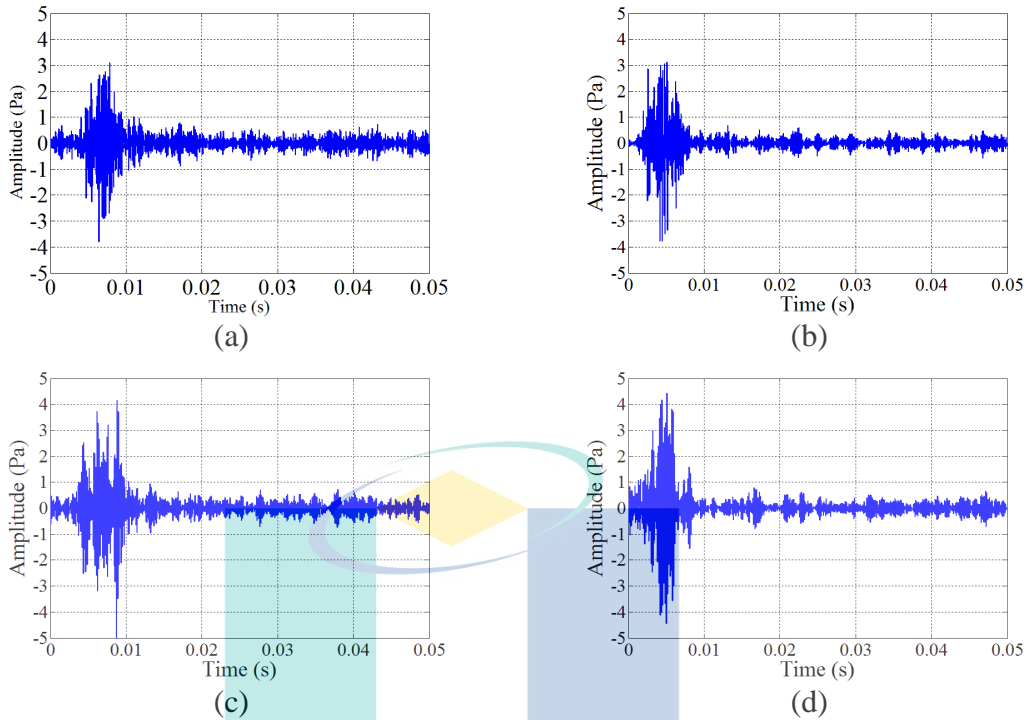
Figure 4.3   Sound signal acquired from laser pulse at 6 ms pulse duration and peak power of (a) 600W (b) 800 W (c) 1000 W (d) 1200W
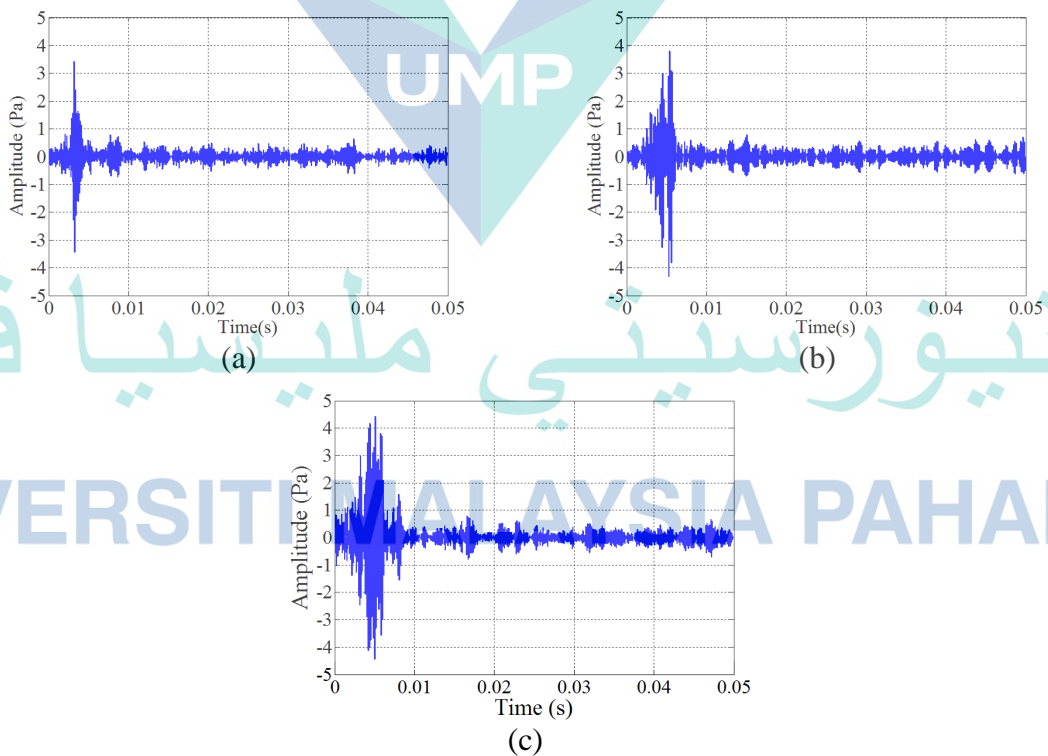
Figure 4.4   Sound signal acquired from laser pulse with peak power of 1200 W and pulse duration of (a) 2 ms (b) 4 ms (d) 6 ms

Earlier studies involving the CW process claimed that the loudest acoustic signal could be captured at deeper penetrations. This phenomenon was found to be closely related to the amount of laser peak power given during the process. As the peak power increased, the vapor flow behavior also changed, and led to different behaviors of the emitted sound (Farson, D. et al., 1998; Farson, D. F. & Kim, K. R., 1999) Compared to the above findings, in this study, a weaker sound amplitude increment was found in PW as the peak power level increased.
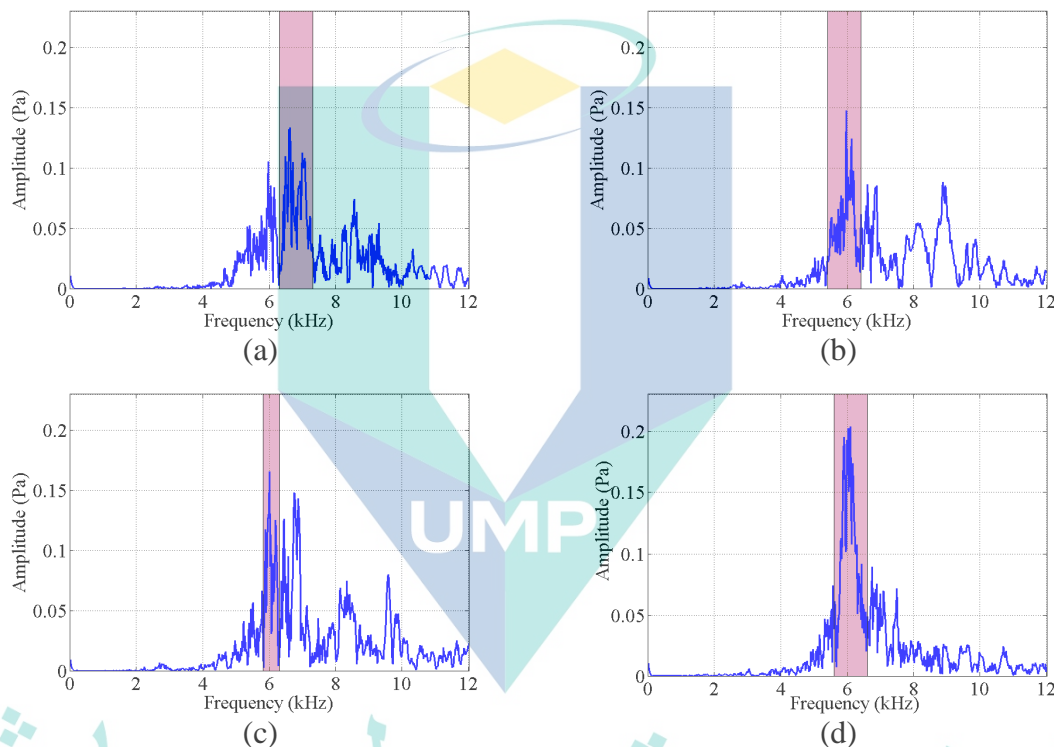
Figure 4.5   Frequency spectrum of the sound pulse from the welding process at 6 ms pulse duration and peak power of (a) 600 W (b) 800 W (c) 1000 W (d) 1200 W

In terms of frequency spectrum trend, the dominant frequency was found to record an indistinguishable pattern with respect to the change in peak power. As depicted in Figure 4.5, the dominant frequency was determined by the frequency at peak amplitude in the red shaded area. The frequency spectrum of the acquired sound from the process with laser peak power of 600 W, 800 W, 1000 W and 1200 W are illustrated in Figure 4.5. Based on the resulted trend, the spectrum from the process with a laser peak power of 600 W displayed a dominant frequency at 6620 Hz. As the

laser peak power increased from 800 W to 1200 W, a dominant frequency was recorded at 5960 Hz, 6000 Hz, and 6080 Hz, respectively.
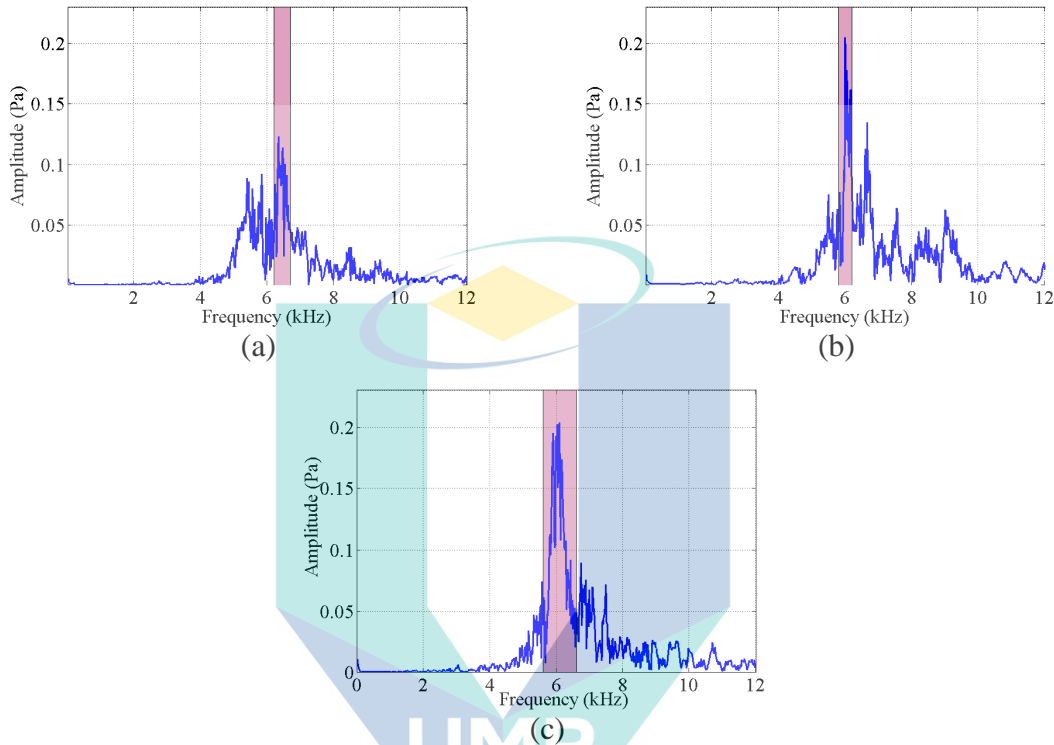
Figure 4.6   Frequency spectrum of a sound pulse from the welding process at 1200 W laser peak power and pulse duration of (a) 2 ms (b) 4 ms (c) 6 ms

In another perspective, the effect of the laser pulse duration on the trend of sound frequency spectrum is depicted in Figure 4.6. Based on the presented results, the trend could not be clearly established. As observed in Figure 4.6(a), the dominant frequency during the laser pulse duration of 2 ms was recorded at 6340 Hz. Meanwhile, the dominant frequency in the case of 4 ms and 6 ms laser pulse durations was recorded at 6000 Hz and 6180 Hz, correspondingly.

To get a clear picture of the overall trend, the dominant frequency of all 195 sampled signals from the entire experiment was illustrated in a boxplot (Figure 4.7). Based on the boxplot, for the case of 2 ms pulse duration (Figure 4.7(a)), the dominant frequency varied between 5800 Hz to 6900 Hz at a peak power of 800 W. In contrast, a smaller range was recorded at a peak power of 1000W, and the dominant frequencies were recorded between 5760 Hz and 6600 Hz. Moreover, the dominant frequencies

were recorded from 5780 Hz to 6900 Hz, 5760 Hz to 6580 Hz, and 5780 Hz to 6580 Hz as the peak power increased from 1200 W to 1400 W, and 1600 W, respectively.
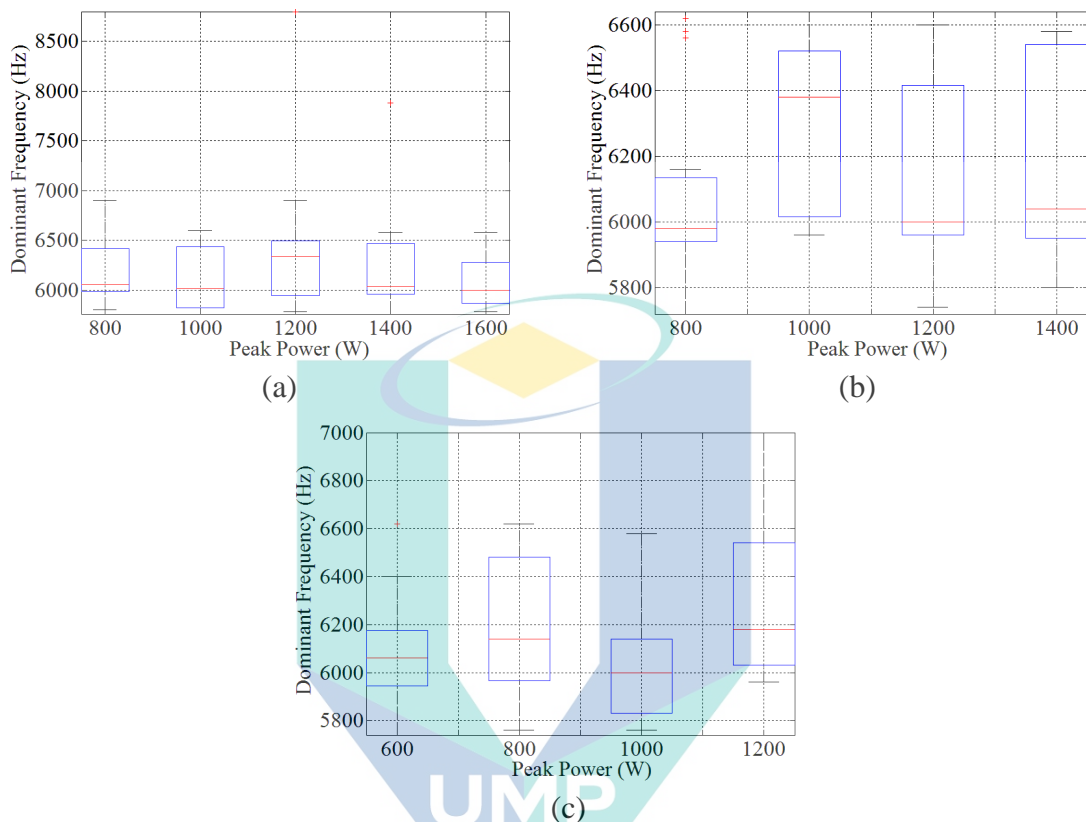
Figure 4.7   Boxplot of the overall variation of the dominant frequencies recorded during the process at different amount of laser peak power and pulse duration (a) 2 ms (b) 4 ms (c) 6 ms

As the same trend was recorded (Figure 4.7(b) and Figure 4.7(c)), it can be summarized that the dominant frequency does not significantly respond to the change in the level of both peak power and pulse duration. Because of the depth of penetration influence by both laser peak power and pulse duration, the overall trend of the dominant frequencies with respect to the changed on the weld penetration was shown in Figure 4.8. Based on the result, it was clear that the dominant frequencies were not related to the change in the depth of penetration.
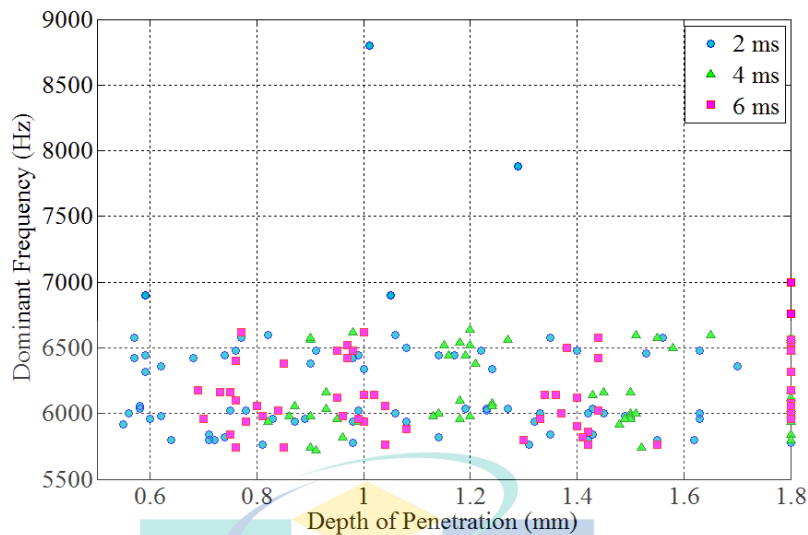
Figure 4.8   The dominant frequencies for all the acquired signal from the entire experiment

Basically, the indistinct trend of sound frequency recorded in this study showed good agreement with past studies. Chapter 2 explained that the frequency of the acquired sound was influenced by the dynamic characteristics of plasma plume during the welding process. A significant number of previous work explained that the keyhole formed from the plasma plume pressure could oscillate from 600 Hz to 7000 Hz (Duley, W. W. & Mao, Y. L., 1994; Huang, W. & Kovacevic, R., 2009, 2011; Klein, T. et al., 1994). Klein, T. et al., (1994) revealed that the oscillation frequency was subjected to the mode of oscillation or Eigen-frequencies. Additionally, some studies suggest that the increasing level of laser peak power, which simultaneously increases the depth of penetration, will boost the amplitudes of sound energy instead of shifting the frequency value (Duley, W. W. & Mao, Y. L., 1994; Farson, D. et al., 1998; Farson, D. et al., 1996).

Based on the trend from the results depicted in Figure 4.3 and Figure 4.4, it can be summarized that the acquired pulse sound recorded a change in its pattern when the laser welding process is performed with different levels of pulse duration. However, it was difficult to characterize the overall sound amplitude trend for the change in laser peak power. Due to this reason, the trend of sound pressure level (SPL) of each sound pulse sampled from the process with varied levels of peak power and pulse duration was plotted in Figure 4.9. Based on the plot, it was noted that the SPL only increased

slightly when the level of laser peak power increased, especially at pulse duration of 2 ms.
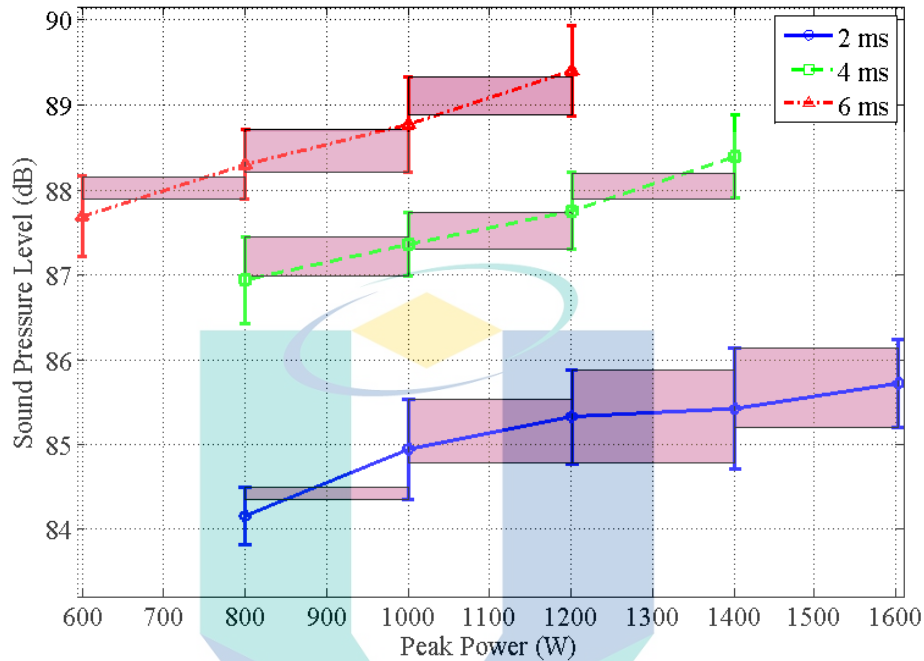
Figure 4.9   Sound pressure level variation from the process with increasing laser peak power and pulse duration.

On the other hand, the range of SPL at any respective peak power and pulse duration was quite large. Consequently, some of the SPL from different laser peak power values fell within the same range. For example, at 800 W laser peak power and 2 ms pulse duration, all sound pressure levels from different experiments were recorded between 83.73 dB and 84.59 dB. Meanwhile, when the laser peak power was increased to 1000 W, the SPL was recorded between 84.41 dB and 85.95 dB. This recorded information redundancy from 84.41 dB to 84.59 dB, as illustrated in the red shaded area. Based on the figure, the redundant information was quite large (i.e., from 1000 W to 1200 W laser peak power). This could cause difficulties in distinguishing the SPL values from different laser peak power levels. As a result, it was quite challenging to characterize the weld penetration from the SPL of pulse sound. In contrast, the SPL at different values of pulse duration recorded a distinct pattern. This can be clearly observed when comparing the SPL at a constant peak power.

4.4   The trend of sound features from the process with variation level of weld parameters

In Section 4.3, the difficulties in distinguishing the SPL from different peak power levels have been revealed. Since the peak power significantly influences the weld depth, this trend has caused difficulties in characterizing the weld penetration from the acquired sound pulse. To address this issue, suitable sound features that can give a strong mutual relationship with penetration depth are needed. Therefore, it is crucial to find an appropriate algorithm to extract these features. As explained in Chapter 1, one of the aims of this work is to develop an algorithm for sound feature extraction. Therefore, the result related to this matter will be presented in this section.

Commonly, to understand the mutual relation between the produced sound and the process condition, the sound was characterized by the trend of its features. In the sound signal analysis, features are extracted from the statistical analysis of sound amplitude distribution, frequency-domain analysis, and time-frequency analysis. In this study, the trend of features extracted from those analyses was investigated before developing the algorithm for feature extraction.

4.4.1   Time-domain feature

As explained in Section 3.7.1, the trend of mean absolute deviation (MAD), standard deviation (SD), kurtosis, L-Cv and L-kurtosis was analyzed in this study. Figure 4.10 illustrates the trend of MAD, SD, kurtosis, L-Cv and L-kurtosis from different values of laser peak power and pulse duration. In Section 3.6.1, it was mentioned that there was a total of 15 data points from each level of laser peak power and pulse duration. Therefore, all the features for specific peak power and pulse duration were plotted against their mean value and 95% confidence interval to observe the overall trend of all experiments.
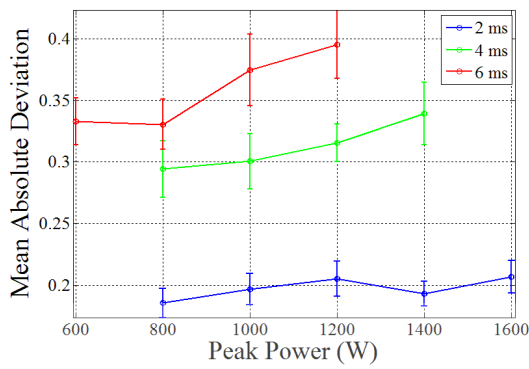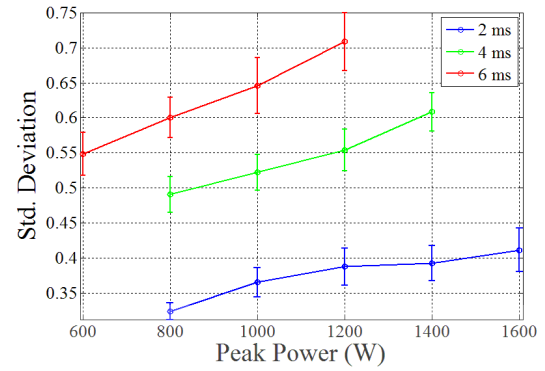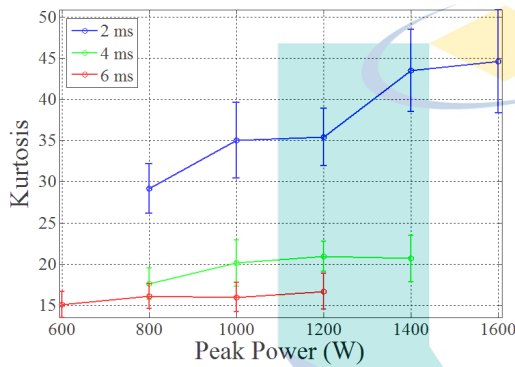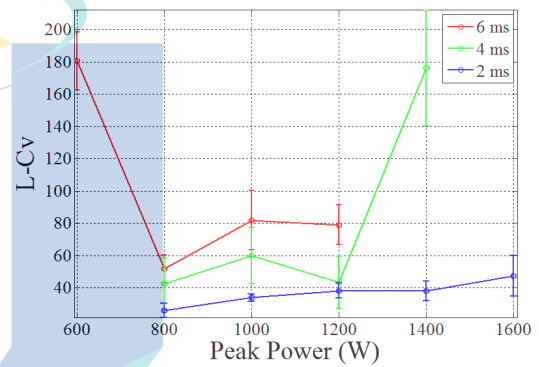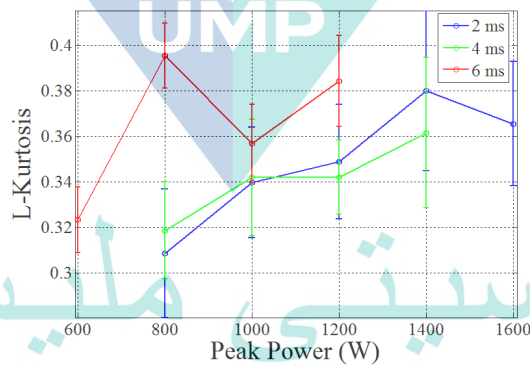
Figure 4.10　　Trend of sound features at a different level of peak power and pulse duration (a) Mean Absolute Deviation (b) Standard Deviation (c) Kurtosis (d) L-Cv (e) L-Kurtosis.

Based on Figure 4.10(a), it can be clearly observed that the MAD shows a significant trend at different values of pulse duration. Higher MADs were recorded for larger pulse durations at a constant peak power. However, at a constant pulse duration, an inconsistent trend of MAD was recorded when the laser peak power level varied. For instance, at a pulse duration of 2 ms, the MAD rose up when the laser peak power

was increased from 800 W to 1200 W. However, the MAD value dropped once the laser peak power reached 1400 W and slightly increased as the laser peak power was further increased. On the other hand, the MAD of sound amplitudes was found to have a direct and linear relationship with the variation in laser peak power at a pulse duration of 4 ms. In contrast, at 6 ms pulse duration, an inconsistent trend of MAD occurred from 600 W to 800 W of laser peak power.

To explain this trend, the results presented in Figure 4.3 and Equation 2.20 need to be referred to. According to Equation 2.20, the model for calculating the MAD value represents the average of the deviation between the amplitudes of sound from its mean value. In the meantime, as observed in Figure 4.3, in most cases, the amplitudes of the sound signals only increased slightly with the change in peak power level. Therefore, this factor might be the reason for the fluctuating MAD trend on some levels of peak power.

Unlike MAD, the SD of the sound amplitudes in Figure 4.10(b) increased with increasing laser pulse duration and peak power. This trend was predictable from the amplitude distribution of all time-domain signals, as illustrated in Figure 4.11. According to Figure 4.11(b), the sound amplitude distribution disperses in a wider range for larger laser pulse durations at a constant laser peak power. Theoretically, SD is the dispersion measure of amplitude distributions (Montgomery, D. C. & Runger, G. C., 2010). Therefore, this might explain why the SD of sound amplitudes increased as the laser pulse duration increased. Compared to MAD, the variation in the SD of sound amplitudes for the change of laser peak power recorded a better linearity trend. This happened because SD is the measure of cumulative amplitude dispersion, while MAD calculates the average value. This is why the SD showed a clear trend with the variation of peak power even though the amplitudes in the time-domain signal shown in Figure 4.3 were difficult to be qualitatively characterized.
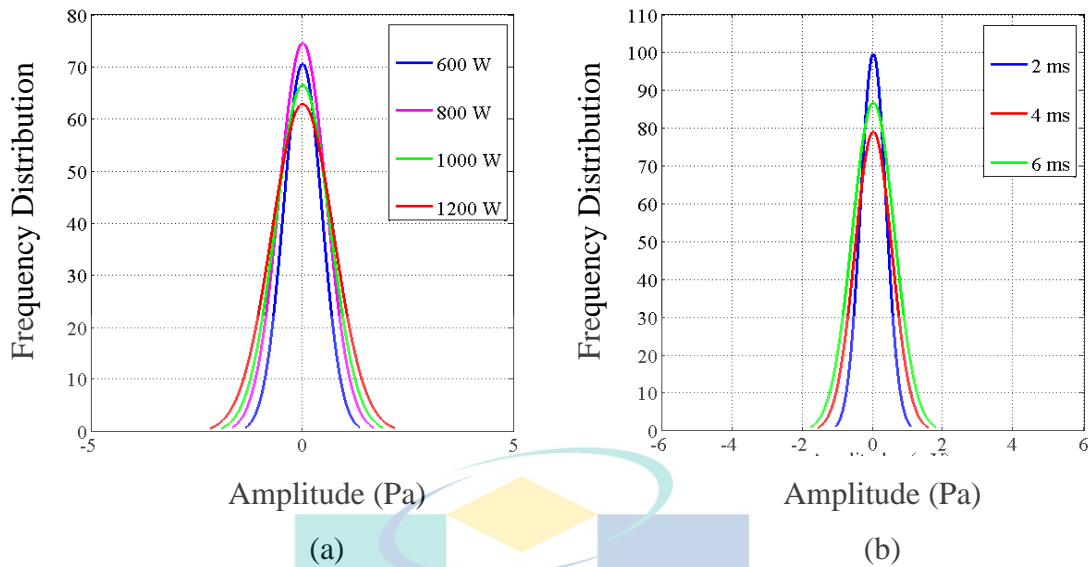
Figure 4.11   Sound amplitudes distribution acquired from the laser welding process with the variation of peak power and pulse duration (a) Process at a pulse duration of 6 ms and different levels of peak power (b) Process at a peak power of 1200W and different level of the pulse duration.

Apart from MAD and SD, sound amplitude kurtosis was also investigated in this study. In general, at a constant laser peak power, higher laser pulse durations give lower kurtosis values. Meanwhile, the trend was quite inconsistent for the case of different peak power levels. At 2 ms laser pulse duration, the kurtosis of sound amplitudes recorded a linear trend with respect to the change in laser peak power. However, the rate of change of kurtosis for the increment of the peak power was almost flat for the 4 ms and 6 ms pulse durations.

Basically, kurtosis is the measure of spikiness of the amplitude distribution (Baren, J. V. et al., 2012). According to the shape of sound amplitude distribution in Figure 4.11(b), it was found that the spikiness of sound amplitude distribution decreased as the pulse duration increased. This might explain why the kurtosis recorded larger values at lower laser pulse durations. In contrast, based on Figure 4.11(a), the spikiness of amplitude distribution from the different laser peak power levels was quite indistinguishable, which explained the trend in Figure 4.10(c).

Looking into the L-Cv and L-kurtosis of the acquired sound in Figure 4.10(d) and Figure 4.10(e), it was clear that both features recorded an inconsistent trend in most cases. However, L-kurtosis shown the smaller variation as compared to the Kurtosis

114

trend in Figure 4.10(c). This variation can be seen from the error bar in the figure, which was made based on 95% confidence interval. As explained in Chapter 2, the use of L moment gives more consistent and reliable trend even though there are outliers in the population (Hosking, J. R. M., 1990, 1992). This could possibly clarify the trend of the L-kurtosis features in Figure 4.10(e). Moreover, this finding was also align with the result from the previous study whereas the L-kurtosis trend was reported not too much influenced by the outliers (Liu, S. et al., 2018)

4.4.2 Frequency-domain features

As detailed out in Section 3.7.2, bandpower was extracted from the frequency spectrum of the acquired sound using Equation 3.4. The trends of bandpower are illustrated in Figure 4.12. According to the results, it can be summarized that bandpower can be used to quantitatively characterize the welding process from different laser pulse durations. In contrast, in the case of different peak power levels, the trend of both features recorded an indistinct trend, especially for the case of 2 ms laser pulse duration at peak power between 1000W and 1600W. Moreover, the average of band power was also detected to be drop at 800 W peak power and 6 ms pulse duration.
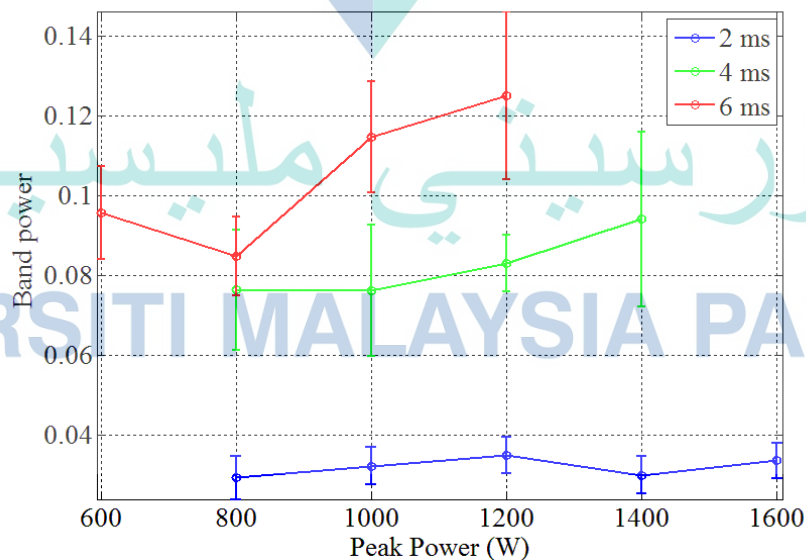
Figure 4.12   Trend of Band power at a different level of peak power and pulse duration.

The trend recorded in this study was quite different to the result that have been reported in the other studies (Huang, W. & Kovacevic, R., 2009, 2011) as the band power recorded distinct trend with respect to laser power. To investigate deeper, the power spectrum density plot of the time-domain signal in Figure 4.3 was depicted in Figure 4.13. Overall, it was clear that the amplitude was dominant within the frequency of 5000 Hz to 7000 Hz in all cases. However, the amplitude pattern at the dominant frequency from different peak power levels recorded an unclear trend. As the bandpower was computed based on the amplitude energy of the signal spectrum (Jerbic, A. B. et al., 2015), this phenomenon lead to the inconsistent bandpower trend at some point in Figure 4.12.
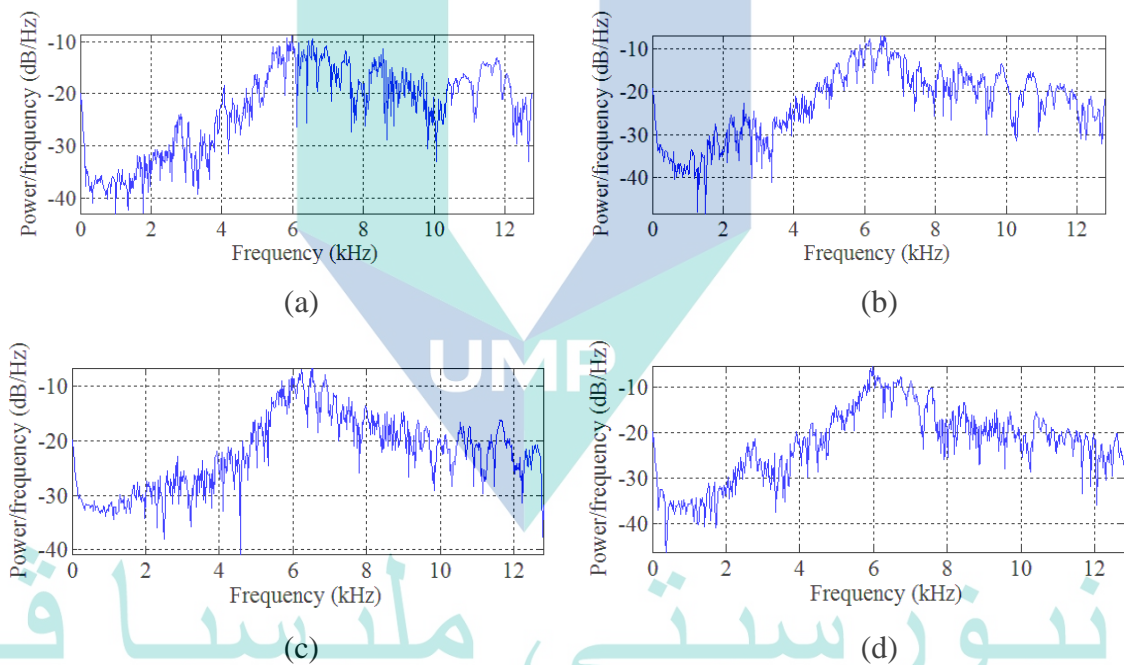
Figure 4.13   Power spectrum density of the acquired sound signal from laser welding with a pulse duration of 6 ms and peak power of (a) 600 W (b) 800 W (c) 1000 W (d) 1200W.

4.4.3   Time-Frequency features

For the time-frequency analysis, the sum of synchrosqueezed wavelet coefficient (CSqWC$_{sum}$) was extracted. The trends of CSqWC$_{sum}$ are illustrated in Figure 4.14. According to the results, it was noticeable that CSqWC$_{sum}$ from different laser pulse duration levels recorded a distinct trend similar to the bandpower.

Meanwhile, at each increment of the laser peak power, the value of CSqWC$_{sum}$ showed a weak linearity trend.
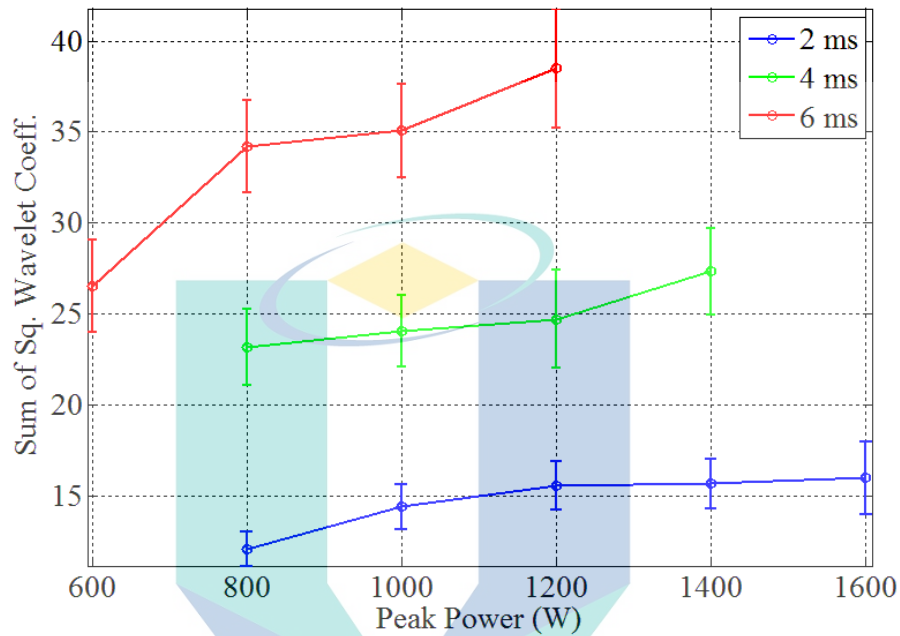
Figure 4.14   Trend of Sum Sq. Wavelet Coefficient at a different level of peak power and pulse duration

To understand deeper, the cumulative time-frequency plot of the time-domain signal is shown in Figure 4.15. This plot was obtained using Equation 3.8. Compared with the frequency-domain signal, the cumulative time-frequency signal plotted in Figure 4.15 gave a smoother pattern on its dominant amplitudes. This was due to the effect of squeezing, which resulted in the suppression of noise (Daubechies, I. et al., 2011; Iatsenko, D. et al., 2015) . However, only a slight change in its amplitude value was recorded as the laser peak power increased, which could explain the weak inclination trend in Figure 4.14. By comparing bandpower and CSqWC$_{sum,}$ it was clear that CSqWC$_{sum}$ offered more advantages in characterizing the signal in response to the change in peak power.
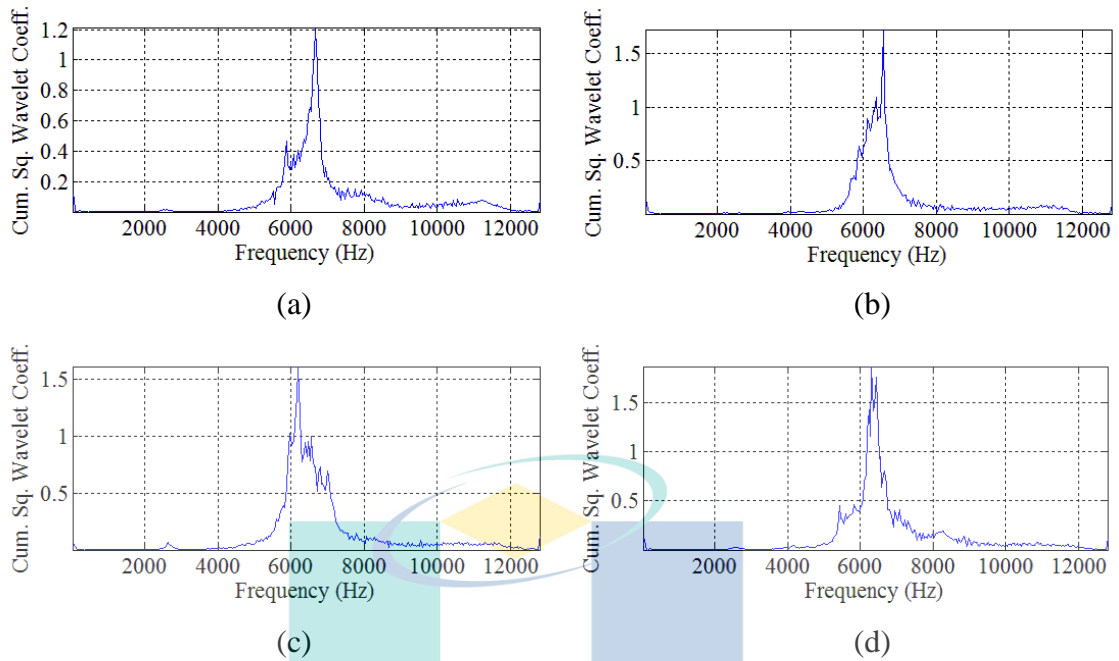
Figure 4.15   Cumulative synchrosqueezed wavelet coefficient for the pulse sound signal acquired during laser welding process with pulse duration of 6 ms and peak power of (a) 600 W (b) 800 W (c) 1000 W (d) 1200 W

4.5   Modified-MLPS algorithm for feature extraction.

In Section 3.8, it was explained that the development of an algorithm for another type of sound feature was done by adopting the MLPS method. To suit with the challenges related to PW process, the original MLPS algorithm was modified by adding the thresholding method to optimize the output. In this thesis, a simple thresholding method was preferred in order to reduce the complexity and processing time. Localized CF threshold was introduced and its performance was compared with the commonly used thresholding methods in wavelet analysis.

4.5.1   Thresholding Method for Noise Elimination

To compare the proposed thresholding method with the Sqtwolog, Rigrsure and Minimaxi, the amplitude modulation transient signal was simulated based on the result presented in Section 4.3. According to the result in Figure 4.8, most of the dominant frequencies were recorded approximately between 5960 Hz and 6440 Hz for the entire experiment. Despite the unclear dominant frequency trend, the amplitude recorded a distinct trend in response to weld parameter variation even though the rate of change

118

was quite low. Due to this reason, the amplitude-modulation transient signal was simulated based on Equation 4.1.

$$x(t) = f(t). A \sin 2\pi f t \qquad\qquad 4.1$$

In this equation, *f* represents the average of dominant frequency from the entire experiment, which was set at 6200 Hz, while the amplitude A was modulated from 4.5 mV to 5 mV with an increment of 0.01 mV. On the other hand, *f(t)* in Equation 4.33 represents the rise and decay rates of the transient signal. Basically, *f(t)* was obtained from the average normalized envelope of all the signals acquired from the laser welding process with different pulse durations, as depicted in Figure 4.16(a). Meanwhile, Figure 4.16(b) displays the normalized envelope of the sound signal from the process with laser pulse durations from 2 ms to 6 ms, which are from the lowest to the largest values used in the experiment.
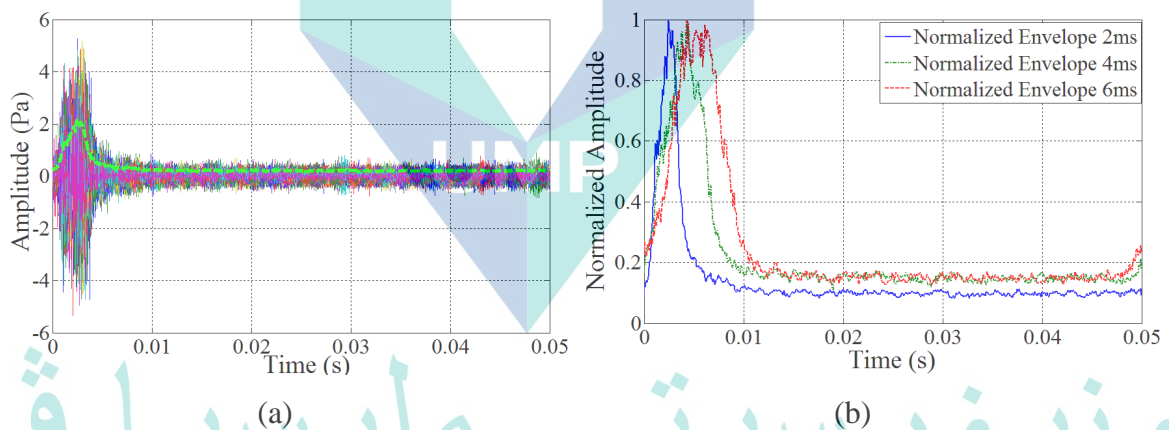
Figure 4.16   Process obtaining normalized enveloped from the acquired signal (a) Normalized enveloped obtained from all of the acquired sounds during the process at 2 ms pulse duration (b) Normalized envelop from the process with different laser pulse duration.

As explained earlier, the localized CF thresholding method was introduced in this study. It was applied in the MLPS algorithm, and the value was compared with the commonly used thresholding methods in wavelet analysis, as shown in Figure 4.17 and Figure 4.18. The overall trend showed that, in all cases, the MLPS value increased with increasing amplitude value. This trend proved the claim that MLPS is sensitive to the

change in amplitude (Bernard, C. et al., 2014; Digulescu, A. et al., 2019; Rosu, G. et al., 2018).
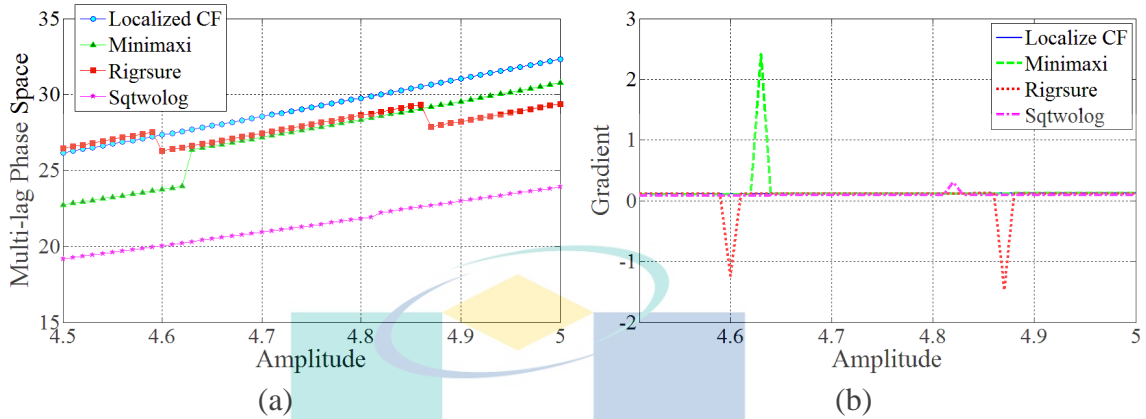
Figure 4.17   Multilag phase space variation results from different thresholding methods in case of the simulated signal for a 2 ms laser pulse duration process. (a) Multilag phase space from different signal amplitude and thresholding method (b) Gradient of Multilag phase space trend from the variation of the thresholding method

The impact of adopting different pre-processed thresholding methods was compared in Figure 4.17(a) and Figure 4.18(a). The results depicted in Figure 4.17(a) generally show that the trend of MLPS records different patterns for different types of thresholds. For instance, for the Rigrsure threshold method, it was found that the MLPS value increased with a consistent rate and dropped at a particular amplitude value. In contrast, a rapid increase of MLPS was found when the amplitude changed from 4.62 to 4.63 when the Minimaxi method was used. The use of the Sqtwolog threshold recorded a similar trend, but a slightly different increment trend was detected when the amplitude changed from 4.81 to 4.83.

Unlike these three thresholding methods, the increment of MLPS recorded a consistent trend when the proposed localized CF thresholding method was applied. This could be clearly observed when the change in the gradient of curve in Figure 4.17(a) was plotted in Figure 4.17(b). A similar trend was recorded for the 6 ms transient signal in Figure 4.18, while the MLPS value of the de-noised signal using the Minimaxi and Sqtwolog thresholding methods recorded an inconsistent linearity trend. Uniquely, the MLPS that was obtained after the signal underwent the Rigrsure

thresholding method was found to increase consistently like in the case of the localized CF thresholding method. However, a comparison between the Rigrsure and localized CF thresholding methods showed that the optimum value of MLPS could be obtained from the de-noised signal using the localized CF method.
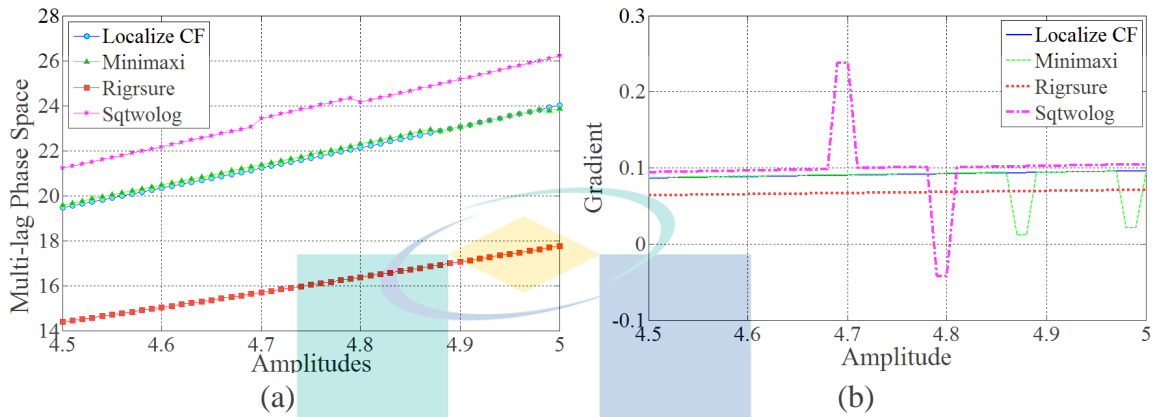
Figure 4.18   Multilag phase space variation results from different thresholding methods in case of the simulated signal for a 6 ms laser pulse duration process. (a) Multilag phase space from different signal amplitude and thresholding method (b) Gradient of Multilag phase space trend from the variation of the thresholding method

As briefly explained earlier, many studies that applied the common wavelet thresholding methods showed contradicting results, suggesting that the best thresholding method depends on several factors (Valencia, D. et al., 2016). Similar to the result in this study, the variation in the amplitude trend leads to the different results obtained from the common wavelet thresholding methods (Valencia, D. et al., 2016; Verma, N. & Verma, A. K., 2012). To explain this, the equations used to determine the threshold value from the Sqtwolog, Rigrsure and Minimaxi methods, as described in Equations 2.13, 2.18, and 2.19, need to be deeply understood. For example, the algorithms to determine the Sqtwolog and Minimaxi thresholds in Equation 2.13 and Equation 2.19, respectively, clearly showed that the value was closely related to the median of the signal amplitude distribution (Karthikeyan, P. et al., 2012; Verma, N. & Verma, A. K., 2012). In this simulation, small amplitude change might not affect the median value of the signal. However, small shift in amplitude might significantly affect the least square estimation which leads to the non-linear change of semi-minor and semi-major axis. In contrast, a deeper look into the Rigrsure algorithm in Equation 2.15

to 2.18 showed that the risk factor depended on the amplitude value (Raj, A. S. et al., 2016), which correspondingly led to an inconsistent trend. On the other hand, the localized CF algorithm promoted the evaluation of the threshold based on the ratio between the localized amplitude and overall energy of the signal. This might explain why the trend of MPLS was more consistent after applying the localized CF thresholding method
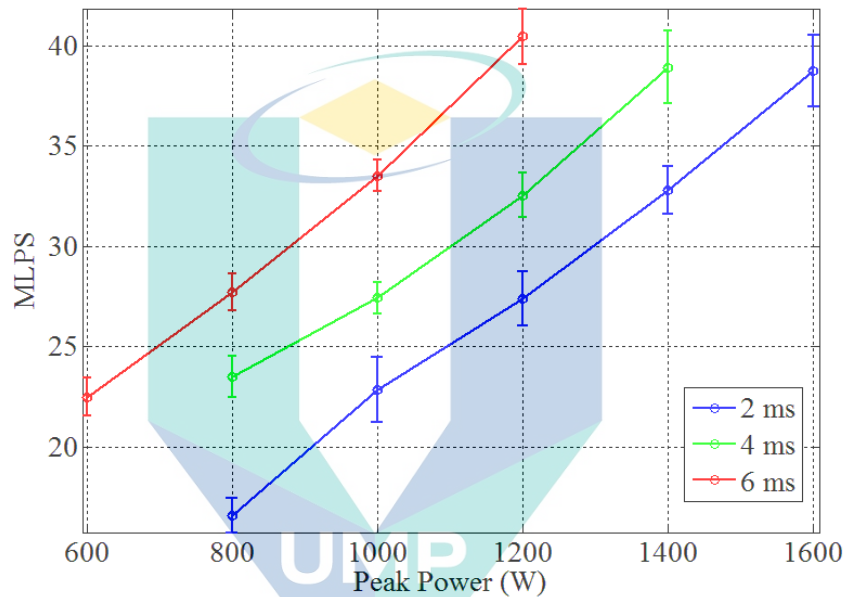
Figure 4.19   Multilag phase space variation from the process with different level of laser peak power and pulse duration

Based on the afore-discussed simulation results, the MLPS algorithm was modified by introducing the localized CF thresholding method. Figure 4.19 represents the trend of MLPS for all 195 signals from different peak power levels and laser pulse durations. The results clearly showed a distinguishable trend of MLPS for the change in peak power and laser pulse duration. Basically, this trend can be explained by the MLPS algorithm itself. As briefed in the previous section, the MLPS algorithm is sensitive to the change in amplitude and frequency (Bernard, C. et al., 2014; Digulescu, A. et al., 2016; Digulescu, A. et al., 2019). In principle, the small change in amplitude of the transient signal will influence the shape of ellipsoid and result in different values in its area. Meanwhile, the change in frequency may also affect the shape of phase space as the signal cycle period changes at different frequencies, which results in the same phenomena. As discussed previously (based on Figure 4.8) the frequency does

not change significantly change due to the variation in peak power. However, the SD trend presented in Figure 4.10(b) evidently showed a difference in the amplitude pattern of time-domain from the variation in peak power and laser pulse duration.

4.6   Feature Selection

In order to evaluate the significant correlation between all features discussed in Section 4.4 to 4.5 with the weld penetration, the stepwise regression analysis was conducted. As explained in Section 3.9, the analysis was done to select the significant features. Table 4.1 shows the results from the stepwise regression, which were reported by the iteration sequence. In the first iteration, the adjusted R-squared value for the overall regression model, which considered all eight sound features, was 0.861. In the second iteration, the L-Cv was eliminated from the regression model due to the small t-stat value. As explained in Section 3.9, t-stats measure the significance of each regression coefficient from each predictive variable (Montgomery, D. C. et al., 2012). As a result from the rejection of L-Cv, the adjusted R-squared value increased to 0.862. Even though the increment was too small, the regression model disregards of L-Cv yield better overall F-stats and P-value, which was recorded to be 173.93 and 2.49×10^{-78}, respectively. Higher F-stats and smaller p-value show the significance of the regression model (Montgomery, D. C. & Runger, G. C., 2010).

In the third iteration, the synchrosqueezed wavelet coefficient was rejected due to the second-lowest t-stat value. As reported in the table, the adjusted R-squared increased by a small amount, F-stats increased to 203.97, and P-value reduced to 1.69×10^{-79}. Eventually, the process continued and stopped at iteration 6, and only SD, L-kurtosis, and MLPS remained significant for the regression model. These results indicate that SD, L-kurtosis and MLPS recorded the strong correlation with the weld penetration and relevant to the estimation model. Aligned with previous study, the energy of the time domain signal which was commonly represented by SD or RMS was reported to show a significant relation with the weld penetration (Farson, D. et al., 1998). On the other hand, even though the use of L-kurtosis and MLPS have not been demonstrated specifically in laser welding application, this finding proved that its algorithm offer advantages when applied in PW laser welding process.

As reported in Figure 4.10, the L-kurtosis recorded indistinct trend with variation of peak power and pulse duration, compared to the SD and MLPS. However, the feature selection analysis results showed that the linear combination of those three features yielded better results. This was happen due to the small variation of L-kurtosis at the same process condition as compared to the traditional kurtosis which was too sensitive to the outliers. As previously explained in section 4.4.1, this trend emerged from the L-moment algorithm itself which suppressed the effect of outlier (Hosking, J. R. M., 1990, 1992). The recorded RMSE, adjusted R-squared, F-stats, and P-value for the final regression model were 0.144, 0.862, 403.9, and 2.07×10^{-82}, respectively.
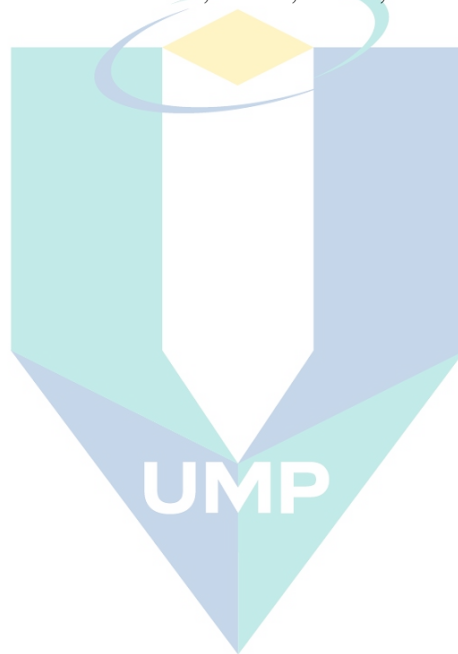
Table 4.1   Stepwise regression results

	In	Features	Beta	Std. Error	t-Stats	P-Value		In	Features	Beta	Std. Error	t-Stats	P-Value
	Yes	Mean Abs. Dev	-2.4471	2.2300	-1.0973	0.2739		Yes	Mean Abs. Dev	-3.0682	1.9077	-1.6083	0.1094
	Yes	Std. Dev.	1.7883	1.3425	1.3321	0.1845		Yes	Std. Dev.	2.0567	1.2556	1.6381	0.1031
	Yes	Kurtosis	-0.0030	0.0021	-1.4204	0.1572		Yes	Kurtosis	-0.0032	0.0021	-1.5163	0.1311
	Yes	L-Cv	0.0000	0.0001	0.1201	0.9046		No	L-Cv	-	-	-	-
Iteration 1	Yes	L-Kurtosis	-1.7850	0.8543	-2.0894	0.0380	Iteration 4	Yes	L-Kurtosis	-1.8410	0.8063	-2.2831	0.0235
	Yes	BandPower	-0.5825	0.9182	-0.6343	0.5266		No	BandPower	-	-	-	-
	Yes	Sq. WC	0.0005	0.0035	0.1517	0.8796		No	Sq. WC	-	-	-	-
	Yes	MLPS	0.0481	0.0028	16.9207	1.72E-39		Yes	MLPS	0.0477	0.0027	17.6682	6.95E-42
RMSE = 0.1438, Adj. R-Square = 0.8611, F-stats= 151.38, P-val = 3.39E-77							RMSE = 0.1428, Adj. R-Square = 0.8630, F-stats= 245.50, P-val = 1.23E-80						
	Yes	Mean Abs. Dev	-2.4297	2.2195	-1.0947	0.2750		Yes	Mean Abs. Dev	-2.3120	1.8476	-1.2514	0.2123
	Yes	Std. Dev.	1.7789	1.3367	1.3308	0.1849		Yes	Std. Dev.	1.8623	1.2533	1.4860	0.1389
	Yes	Kurtosis	-0.0030	0.0021	-1.4211	0.1570		No	Kurtosis	-	-	-	-
	No	L-Cv	-	-	-	-		No	L-Cv	-	-	-	-
Iteration 2	Yes	L-Kurtosis	-1.7767	0.8493	-2.0921	0.0378	Iteration 5	Yes	L-Kurtosis	-1.6594	0.8001	-2.0740	0.0394
	Yes	BandPower	-0.5692	0.9092	-0.6261	0.5320		No	BandPower	-	-	-	-
	Yes	Sq. WC	0.0005	0.0034	0.1398	0.8890		No	Sq. WC	-	-	-	-
	Yes	MLPS	0.0481	0.0028	16.9655	1.08E-39		Yes	MLPS	0.0456	0.0023	19.6230	1.43E-47
RMSE =0.1434, Adj. R-Square = 0.8618, F-stats= 173.93, P-val = 2.49E-78							RMSE = 0.1433, Adj. R-Square = 0.8621, F-stats= 304.22, P-val = 2.07E-81						
	Yes	Mean Abs. Dev	-2.3970	2.2013	-1.0889	0.2776		No	Mean Abs. Dev	-	-	-	-
	Yes	Std. Dev.	1.7878	1.3317	1.3426	0.1810		Yes	Std. Dev.	0.298623	0.0959	3.1140	0.00213
	Yes	Kurtosis	-0.0030	0.0021	-1.4180	0.1578		No	Kurtosis	-	-	-	-
	No	L-Cv	-	-	-	-		No	L-Cv	-	-	-	-
Iteration 3	Yes	L-Kurtosis	-1.7479	0.8218	-2.1270	0.0347	Iteration 6	Yes	L-Kurtosis	-0.69933	0.2273	-3.0768	0.0024
	Yes	BandPower	-0.5512	0.8977	-0.6141	0.5399		No	BandPower	-	0.7802	-1.3137	-
	No	Sq. WC	-	-	-	-		No	Sq. WC	-	0.0033	-0.3263	-
	Yes	MLPS	0.04805	0.00277	17.34786	7.05E-41		Yes	MLPS	0.0475	0.0017	27.7068	7.91E-69
RMSE = 0.1431, Adj. R-Square = 0.8625, F-stats= 203.97, P-val = 1.69E-79							RMSE = 0.1435, Adj. R-Square = 0.8617, F-stats= 403.91, P-val = 2.07E-82						
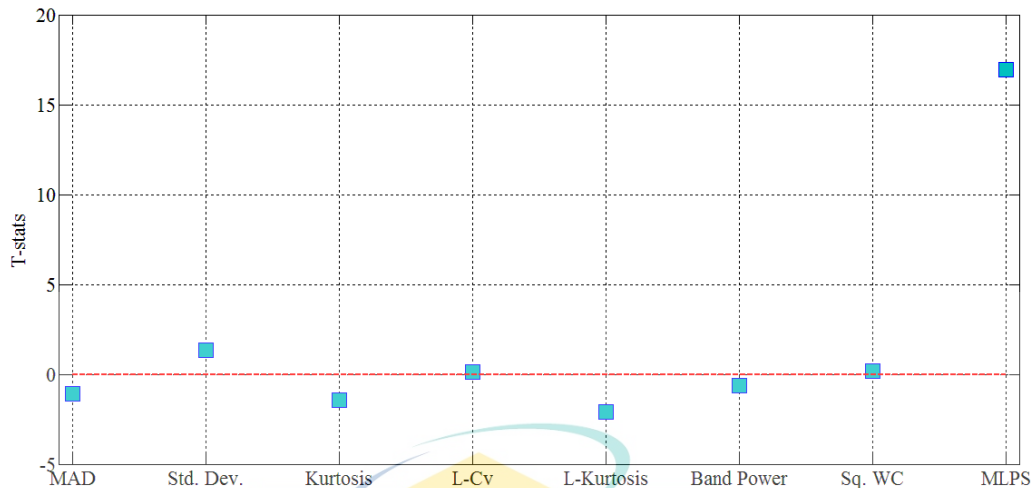
Figure 4.20   Deviation of t-stats of each feature from 0 for each sound features involved in the feature selection analysis

To investigate why the L-kurtosis was selected in the stepwise regression analysis instead of the normal kurtosis, the trend of t-stats of each sound features during the first iteration was plotted in Figure 4.20. As mentioned earlier, the selection of the predictive variables in the stepwise regression analysis was made based on the t-stat value. It is basically the ratio between the mean of the coefficient and its standard error. Meanwhile, standard error is defined as the average distance from the real data point to the estimated point in the regression line. This means that low standard error gives further t-stats value from zero.

Based on the calculated ratio shown in Figure 4.20, it is clear that the t-stats of the regression coefficient for L-kurtosis are much further from 0. This indicates that the regression coefficient for L-kurtosis estimated by the regression process is more significant, which has been theoretically explained by Montgomery et al.,(2012). Recalling that the deviation trend in Figure 4.10 was based on 95% confident interval, this indicates that the L-kurtosis recorded low deviation and less outliers as compared to the other rejected sound features from the stepwise regression analysis.

According to results of the stepwise regression analysis, the adjusted R-squared for the overall regression model (considering the best three sound features), was 0.862. Based on the general theory of regression, this value shows that the degree of correlation between sound features and weld penetration depth was quite strong

(Montgomery, D. C. & Runger, G. C., 2010). Despite the significant improvement in F-stats and P-value of the overall model, it is believed that it is essential to include the peak power and pulse duration as parts of the predictive variables in developing a predictive model for weld depth estimation. This is important to observe how the weld parameters can improve the degree of correlation between all predictive variables in the model with the output. In the previous work by Huang, W. & Kovacevic, R., (2009), when developing a characterization model, the weld parameters were included as predictive variables, which resulted in a significant amount of estimation errors. Therefore, both parameters were considered for forward selection in further stepwise regression analysis, whereas SD, L-kurtosis, and MLPS remained as the pre-selected predictive variables. According to the result in Table 4.2, the addition of pulse duration and peak power was significant to the final model. By considering both weld parameters, the F-stats and P-values increased to 580.81 and 1.23×10^{-112}, respectively.

Table 4.2   Additional step in stepwise regression analysis by considering weld parameters

	In	Features	Beta	Standard Error	t-Stats	P-Value
Iteration 7	No	Mean Abs. Dev	-	1.90819	-1.06615	0.28772
	Yes	Std. Dev.	0.4485	0.19491	2.30099	0.02248
	No	Kurtosis	-	0.00204	-1.21199	0.22703
	No	L-Cv	-	0.00007	-0.18285	0.85511
	Yes	L-Kurtosis	-0.7076	0.22762	-3.10860	0.00217
	No	BandPower	-	0.79134	-1.18631	0.23699
	No	Sq. WC	-	0.00362	0.00997	0.99205
	Yes	MLPS	0.0467	0.0020	23.9100	3.44E-59
	Yes	Pulse duration	-11.3757	12.8782	-0.8833	0.378175
	No	PeakPower	-	8.89E-05	15.1803	1.49E-34
RMSE = 0.1436, Adj. R-Square = 0.8615, F-stats= 302.77, P-val = 3.06E-81						
Iteration 8	No	Mean Abs. Dev	-	1.2770	-1.8276	0.0692
	Yes	Std. Dev.	0.6342	0.1318	4.8139	0.0000
	No	Kurtosis	-	0.0013	-3.7616	0.0002
	No	L-Cv	-	0.0000	-1.1741	0.2418
	Yes	L-Kurtosis	-0.8141	0.1534	-5.3086	0.0000
	No	BandPower	-	0.5323	-1.3407	0.1816
	No	Sq. WC	-	0.0024	-1.5195	0.1303
	Yes	MLPS	0.0014	0.0033	0.4185	6.76E-01
	Yes	Pulse duration	116.4430	12.0840	9.6361	3.96E-18
	Yes	PeakPower	0.00135	8.89E-05	15.1803	1.49E-34
RMSE =0.0966, Adj. R-Square = 0.9372, F-stats= 580.82, P-val = 1.23E-112						

127

4.7   The Weld Depth Estimation Model

4.7.1   Multiple Linear Regression Model

Based on the stepwise regression analysis, standard deviation (SD), L-kurtosis, multi-lag phase space (MLPS), peak power, and pulse duration were found to be significant predictive variables for the weld depth estimation model. Therefore, multiple linear regression (MLR) analysis was conducted on the 195 training data from each parameter or feature, which gave the regression equation (Equation 4.2). In the equation, DOP, SD, LK, MLPS, PD, and PP represent the depth of penetration, standard deviation, L-kurtosis, multi-lag phase space, laser pulse duration, and laser peak power, respectively. The adjusted R-squared value for this regression equation obtained from the training dataset was 0.9373, which showed a good fitting with the penetration depth. The mean and SD of the estimation errors were 7.49% and 5.12%, respectively.

$$DOP = 0.634SD - 0.814LK + 0.0014MLPS + 116.44PD + 0.0014PP - 0.7781 \qquad 4.2$$

By observing the regression coefficient in Equation 4.2, it was clear that the results were similar with the coefficients obtained from the final iteration of the stepwise regression in Table 4.2. This was because the algorithm in stepwise regression applied the MLR method and the process iterated until the best model was obtained.

4.7.2   Artificial Neural Network Model

Apart from the multiple linear regression (MLR) method, the weld depth estimation model was also developed via the artificial neural network (ANN) approach. As explained in Section 3.10.2, the model training was done using a three-layer network with a varied number of hidden neurons, i.e., from 5 to 25. Figure 4.21 depicts the variation in output errors from all 195 samples in the training set for the 5-5-1, 5-10-1, 5-15-1, 5-20-1, and 5-25-1 networks. Overall, it was noticeable that the highest average output error was recorded by the 5-5-1 network, at 4.35%. In descending order, it was followed by the 5-25-1, 5-15-1, and 5-10-1 networks, with an average output

error of 3.72%, 3.65%, and 3.5%, respectively. Meanwhile, the lowest output error was recorded by the 5-20-1 network, at 3.3%.
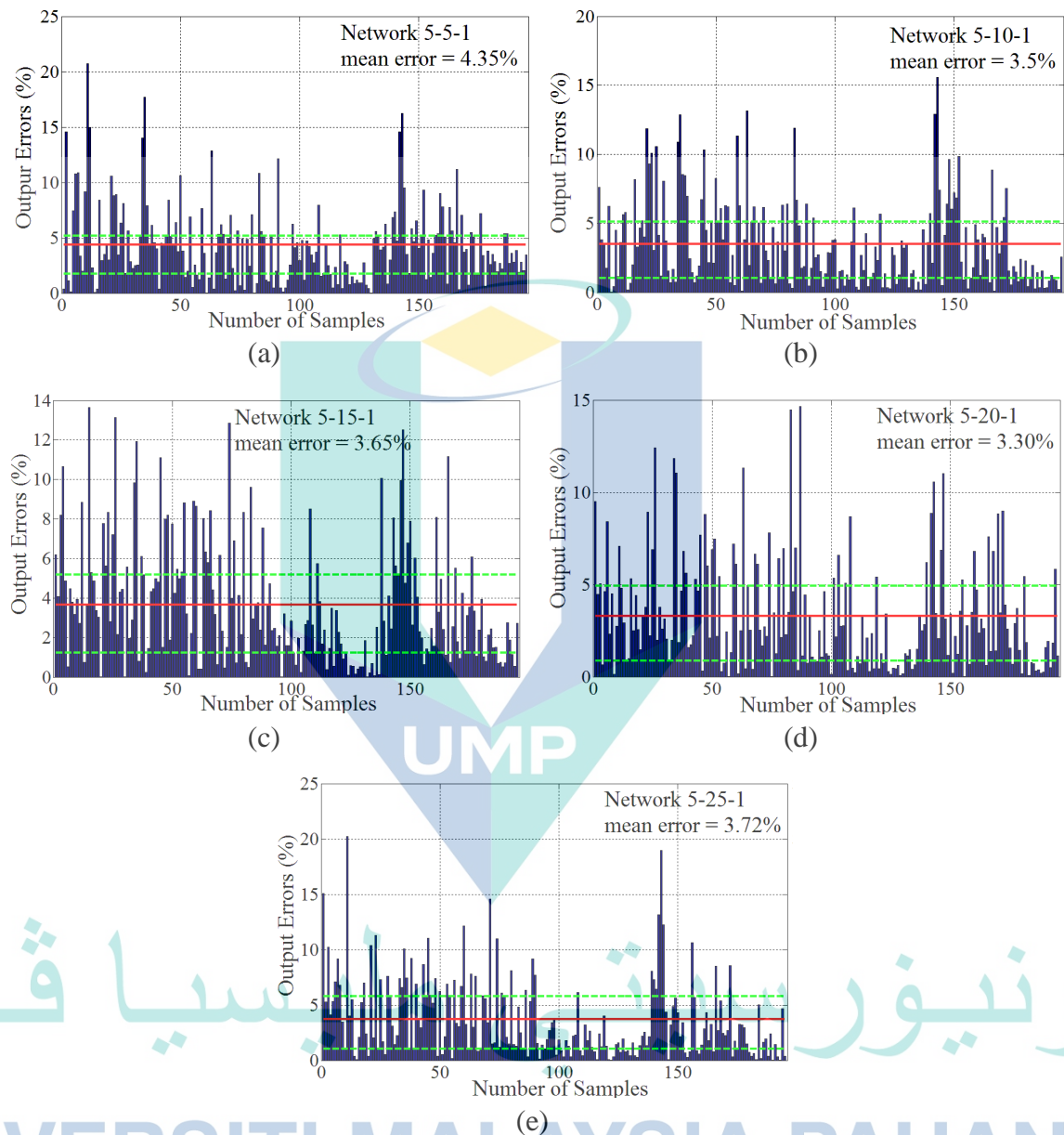
Figure 4.21   Variation of output errors from all 195 samples in training set for network (a)5-5-1 (b)5-10-1 (c)5-15-1 (d)5-20-1 (e)5-25-1

Since the average value was affected by the variation in output errors, the deviation of the recorded errors was also determined in this study. Based on the results, the lowest SD of errors was recorded by the 5-20-1 network. This was followed by the 5-15-1, 5-10-1, 5-5-1, and 5-25-1 networks (in ascending order). Based on the trend of both average and deviation of the output errors, it can be summarized that the number of hidden neurons does not significantly influence the output errors of the trained

model. However, a higher amount of neurons might affect the processing time. Considering these facts, the network with the lowest number of neurons, which could give the lowest average of error, was the 5-10-1 network.

4.8   Model Validation

In order to test both empirical models, a validation experiment was done. As explained before, for each experiment, three points were selected for the study, which gave a total of 39 weld penetration data points for model validation. In the meantime, 39 pulse sounds were also captured simultaneously, and all features stated in the estimation model were extracted to determine the estimated penetration depth.

4.8.1   Multiple Linear Regression Model Validation

Figure 4.22(a) depicts the estimated penetration depth determined from Equation 4.2 and the actual penetration measured from the validation experiment. The overall trend from the figure show that the estimated depth recorded different values compared to the actual penetration.

$$e = \frac{|DOP_{actual} - DOP_{estimated}|}{DOP_{actual}} \qquad 4.3$$

To get a clear picture of how the estimated depth deviates from its actual value, the estimation errors for each point were calculated using equation 4.3 and plotted in Figure 4.22(b). Based on the figure, it can be seen that the highest estimation error was 20.86%, while the lowest error is 0.203%. Overall, the calculated mean error was 7.13%, while the interquartile range of all analyzed estimation error was between 3.77 % to 10.05 %, which can be observed from the boxplot. As discussed in Section 2.7.4, in the work related to spot welding, the error of the developed MLR model was reported around the average of 5.29% (Zhao, D. et al., 2020). On another work associates with CW laser welding, the developed MLR models were recorded the average error between 6.44% and 10.07% (Huang, W. & Kovacevic, R., 2011). Hence, the average error recorded for the model developed in this study was expected to be acceptable as compared to the previous work.
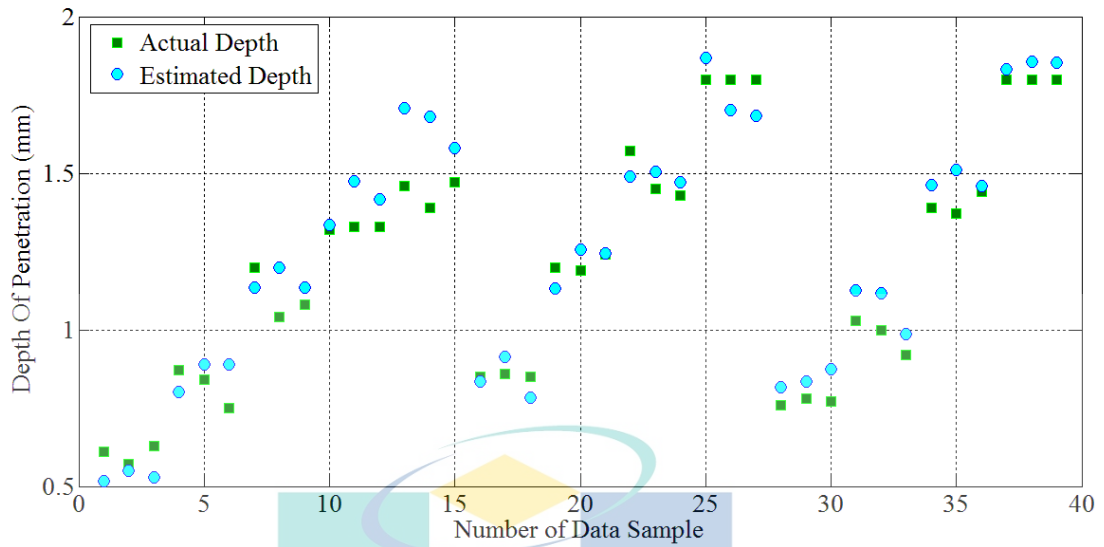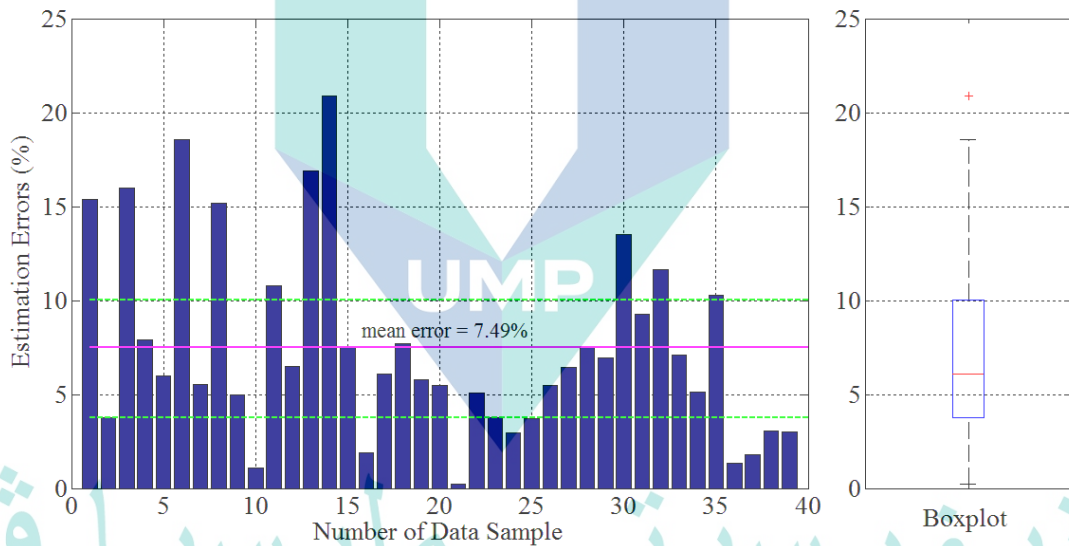
Figure 4.22 Estimated weld penetration from analysis of sound from validation experiment using multiple linear regression model (a) Actual and Estimated weld penetration (b) Estimation errors

4.8.2 Artificial Neural Network Model Validation

On another part of the work, five network models for weld depth estimation were successfully developed using the artificial neural network (ANN) method. To test the significance of these networks, the estimated weld depth was determined from these

networks using the same 39 data obtained from the validation experiment. Table 4.3 shows the variation in estimated depth and the actual penetration measured from the validation experiment.
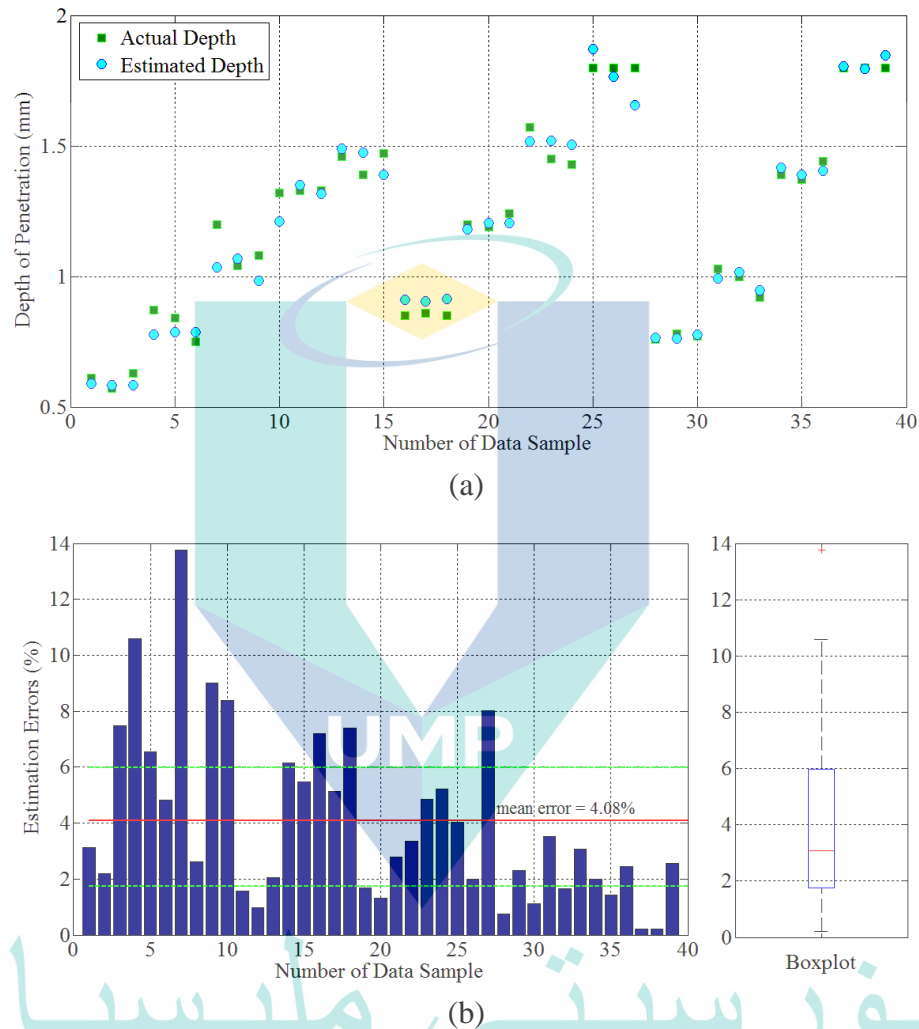
Figure 4.23   Estimated weld penetration from analysis of sound from validation experiment using network 5-10-1 (a) Actual and Estimated weld penetration (b) Estimation errors.

According to the results in Table 4.3, it was noticeable that the estimation errors were recorded from 0.21% to 13.76% for all networks. By comparing the mean of the estimation errors, the 5-10-1 network recorded the lowest value. On the other hand, the 5-5-1 network showed the lowest fluctuation of estimation errors, as the SD of errors recorded the lowest value. In order to see a clear picture, the estimated depth, which was calculated using the 5-10-1 network and the errors are plotted in Figure 4.23(a) and Figure 4.23(b), respectively. Based on both figures, it is clear that the estimated depth

of penetration is slightly different from the actual depth. In the case of the 5-10-1 network, the estimation errors varied from 1.75 % to 5.97 % according to its interquartile range. Meanwhile, the mean and SD of the estimation errors were recorded to be 4.08 % and 3.1 %, respectively, for this network.
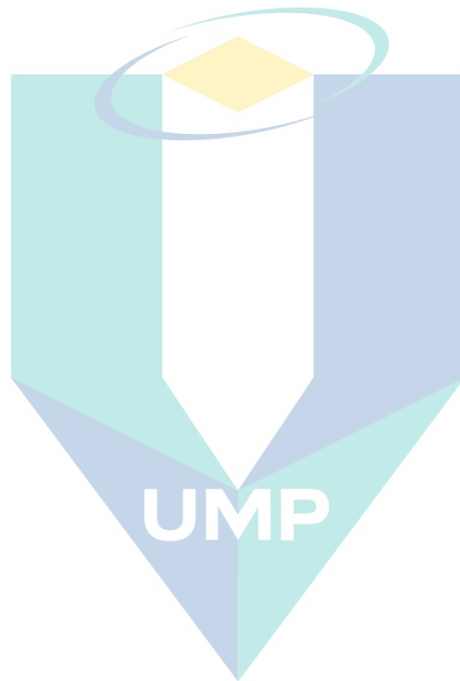
Table 4.3   Estimated weld depth penetration by using the developed neural model

Index	5-5-1			5-10-1			5-15-1			5-20-1			5-25-1		
	Est. Depth (mm)	Act. Depth (mm)	Est. Errors (%)	Est. Depth (mm)	Act. Depth (mm)	Est. Errors (%)	Est. Depth (mm)	Act. Depth (mm)	Est. Errors (%)	Est. Depth (mm)	Act. Depth (mm)	Est. Errors (%)	Est. Depth (mm)	Act. Depth (mm)	Est. Errors (%)
1	0.57	0.61	6.67	0.59	0.61	3.14	0.60	0.61	1.92	0.60	0.61	1.29	0.62	0.61	1.00
2	0.63	0.57	10.83	0.58	0.57	2.19	0.60	0.57	4.64	0.58	0.57	1.22	0.57	0.57	0.67
3	0.60	0.63	4.34	0.58	0.63	7.48	0.60	0.63	4.06	0.59	0.63	6.57	0.57	0.63	9.63
4	0.77	0.87	10.98	0.78	0.87	10.59	0.79	0.87	9.38	0.80	0.87	8.52	0.84	0.87	3.07
5	0.78	0.84	6.78	0.78	0.84	6.55	0.75	0.84	10.40	0.78	0.84	7.25	0.76	0.84	9.83
6	0.81	0.75	7.46	0.79	0.75	4.81	0.80	0.75	6.75	0.81	0.75	7.73	0.74	0.75	1.31
7	1.11	1.20	7.64	1.03	1.20	13.76	0.98	1.20	18.43	1.02	1.20	14.80	0.98	1.20	18.44
8	1.10	1.04	5.68	1.07	1.04	2.61	1.11	1.04	6.88	1.22	1.04	17.12	1.05	1.04	1.33
9	1.01	1.08	6.74	0.98	1.08	9.02	1.01	1.08	6.93	0.98	1.08	8.93	1.00	1.08	7.64
10	1.20	1.32	9.02	1.21	1.32	8.39	1.22	1.32	7.47	1.29	1.32	2.00	1.22	1.32	7.93
11	1.35	1.33	1.27	1.35	1.33	1.56	1.34	1.33	1.05	1.45	1.33	9.18	1.34	1.33	0.54
12	1.27	1.33	4.58	1.32	1.33	0.98	1.27	1.33	4.33	1.24	1.33	6.82	1.24	1.33	7.11
13	1.48	1.46	1.36	1.49	1.46	2.06	1.51	1.46	3.51	1.48	1.46	1.27	1.52	1.46	4.10
14	1.52	1.39	9.77	1.48	1.39	6.14	1.61	1.39	16.07	1.55	1.39	11.62	1.55	1.39	11.49
15	1.41	1.47	3.90	1.40	1.47	5.48	1.43	1.47	3.06	1.31	1.47	10.94	1.18	1.47	19.61
16	0.90	0.85	5.53	0.91	0.85	7.21	0.90	0.85	6.12	0.90	0.85	5.50	0.88	0.85	3.64
17	0.90	0.86	5.16	0.90	0.86	5.12	0.91	0.86	6.35	0.94	0.86	9.30	0.82	0.86	4.97
18	0.91	0.85	7.35	0.91	0.85	7.40	0.89	0.85	4.21	0.92	0.85	8.69	0.92	0.85	8.26
19	1.17	1.20	2.41	1.18	1.20	1.68	1.19	1.20	0.72	1.21	1.20	0.89	1.18	1.20	1.53
20	1.16	1.19	2.55	1.21	1.19	1.31	1.20	1.19	0.57	1.25	1.19	5.45	1.20	1.19	1.05
21	1.15	1.24	7.33	1.21	1.24	2.79	1.20	1.24	3.45	1.23	1.24	0.57	1.22	1.24	1.98
22	1.49	1.57	5.23	1.52	1.57	3.34	1.47	1.57	6.09	1.49	1.57	5.23	1.50	1.57	4.51
23	1.51	1.45	4.27	1.52	1.45	4.84	1.47	1.45	1.60	1.48	1.45	1.99	1.51	1.45	4.24
24	1.46	1.43	2.41	1.50	1.43	5.21	1.51	1.43	5.63	1.53	1.43	7.02	1.52	1.43	6.58
25	1.82	1.80	1.20	1.87	1.80	4.02	1.76	1.80	2.23	1.87	1.80	3.67	1.81	1.80	0.51
26	1.68	1.80	6.87	1.76	1.80	1.99	1.80	1.80	0.10	1.78	1.80	1.32	1.79	1.80	0.38
27	1.63	1.80	9.59	1.66	1.80	8.03	1.80	1.80	0.27	1.70	1.80	5.58	1.93	1.80	6.97
28	0.80	0.76	4.88	0.77	0.76	0.74	0.73	0.76	3.48	0.76	0.76	0.17	0.80	0.76	4.74
29	0.81	0.78	4.23	0.76	0.78	2.30	0.81	0.78	3.66	0.81	0.78	3.64	0.78	0.78	0.33
30	0.80	0.77	3.78	0.78	0.77	1.12	0.72	0.77	7.00	0.76	0.77	1.85	0.80	0.77	4.10
31	1.01	1.03	1.51	0.99	1.03	3.51	1.03	1.03	0.35	0.98	1.03	4.79	1.02	1.03	0.77
32	0.98	1.00	1.81	1.02	1.00	1.65	1.09	1.00	8.74	1.08	1.00	7.77	1.13	1.00	12.57
33	0.97	0.92	5.41	0.95	0.92	3.07	0.79	0.92	13.40	1.12	0.92	21.36	0.88	0.92	0.04
34	1.37	1.39	1.33	1.42	1.39	2.00	1.38	1.39	0.96	1.42	1.39	1.92	1.38	1.39	0.93
35	1.40	1.37	2.11	1.39	1.37	1.43	1.35	1.37	1.51	1.40	1.37	2.48	1.38	1.37	0.82
36	1.37	1.44	5.11	1.40	1.44	2.44	1.37	1.44	5.08	1.43	1.44	0.88	1.43	1.44	1.03
37	1.76	1.80	2.30	1.80	1.80	0.21	1.77	1.80	1.86	1.78	1.80	0.96	1.79	1.80	0.49
38	1.76	1.80	2.24	1.80	1.80	0.22	1.79	1.80	0.30	1.76	1.80	2.44	1.87	1.80	3.74
39	1.78	1.80	1.00	1.85	1.80	2.56	1.75	1.80	2.61	1.74	1.80	3.38	1.77	1.80	1.75
	Mean Errors		4.94	Mean Errors		4.08	Mean Errors		4.92	Mean Errors		5.69	Mean Errors		4.71
	Std. Dev. Errors		2.85	Std. Dev. Errors		3.10	Std. Dev. Errors		4.30	Std. Dev. Errors		4.82	Std. Dev. Errors		4.77

UNIVERSITI MALAYSIA PAHANG

4.8.3 Estimation Models Comparison

According to the ANN analysis results, it can be summarized that this method is better in developing the weld penetration estimation model than the MLR method. This is because the network model developed from ANN is more accurate and precise, owing to its lower mean and SD of estimation errors. Compared with the estimation model developed via the MLR method, all five network models gave lower values of mean and SD of errors.

In order to show a clear comparison, the estimated depth from the MLR and ANN models was shown in Figure 4.24. Considering the 5-10-1 network as the best network among the five models developed from the ANN analysis, only the results from this model were compared with the results from the MLR model. Figure 4.24(a) depicts the estimated depth from the MLR model in Equation 4.2 and the 5-10-1 network model in the case of the PW process with peak power and pulse duration of 1000 W and 2 ms, respectively. The estimated weld depth from the MLR model was offset further from the actual depth compared to the estimated depth from the 5-10-1 model. A quantitative comparison was made from the results shown in Figure 4.22 and Figure 4.23, and the results depicted in Figure 4.24 were taken from this point of experiment. Based on the sixth point in the validation experiment, the actual depth was 0.75 mm. Meanwhile, the estimated depth for both the MLR and 5-10-1 network models was 0.89 mm and 0.79 mm, respectively.

| (a) | (b) |

Figure 4.24   Cross sectional images of the actual and estimated depth obtained from both MLR and ANN model (a) 2 ms 1000 W (b) 4 ms 1400 W

On the other hand, a comparison in terms of efficiency of both models in the case of the process with 1400 W peak power and 4 ms pulse duration is illustrated in Figure 4.24(b). A similar trend was also recorded in which the estimated depth from the 5-10-1 network model was closer to the actual depth.

In Chapter 3, it was explained that the weld depth estimation model was developed by learning the sound feature and weld parameter trend. The sound feature was obtained from the sampled signal at the described location in Figure 3.15. In order to see the significance of the developed models, the ability of these models in estimating the weld depth for the entire process was also tested.

To test both estimation models on the whole process, another two sets of validation experiment were done. One experiment was conducted with 1200 W peak power and 4 ms pulse duration, while the other was carried out with 600 W peak power and 6 ms pulse duration. Both MLR and the 5-10-1 network models were used to estimate the depth from the acquired sound along these experiments. To compare the estimated depth with the actual ones, the specimen was cut in longitudinal direction and the comparison is illustrated in Figure 4.25.

(a)

(b)
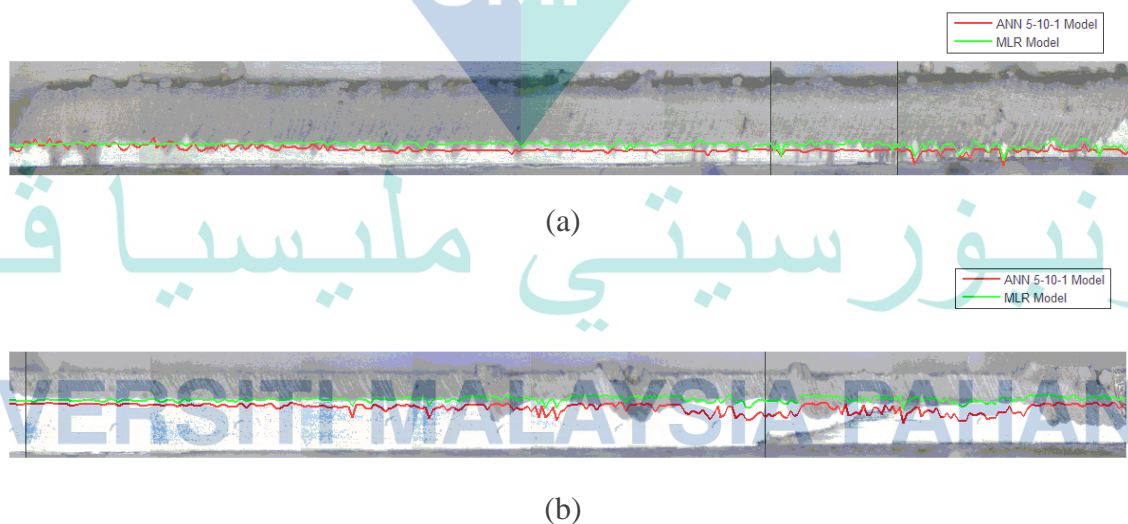
Figure 4.25   Longitudinal image of the actual and estimated depth from the process with (a) 1200 W, 4 ms (b) 600 W, 6 ms

Overall, the estimated depth from both models showed an almost consistent value along the process. However, in the case of the process with 600 W peak power and 6 ms pulse duration, irregularities could be noticed at certain locations and a deeper

actual penetration occurred at a particular spot. Despite the larger penetration, a significant amount of underfill on top of the weld bead was also observed. Past evidence proved that the presence of a large underfill would affect the behavior of the acquired sound signal. However, in this study, the experiment was designed by minimizing the amount of defect. This has been explained in detail in Chapter 3. Therefore, the estimation models were developed by learning the trend of acoustic signal with less-influence from defect-source sound element. This might be the reason why the estimated depths from both models were far from the actual values. In general, the estimated depth from the 5-10-1 model was closer to the actual depth than the estimated depth from the MLR model.

4.9   Results summary

In the beginning of this chapter, the characteristics of sound acquired from the PW laser welding with variation in laser peak power and pulse duration were investigated. The results revealed that all the acquired sounds showed a transient pattern, and the duration of transient was directly related to the change in laser pulse duration. Meanwhile, the overall amplitude was found to be slightly increased as the laser peak power level increased. On the other hand, the dominant frequency recorded an indistinct pattern, which showed that the frequency did not significantly change with the variation in laser peak power and pulse duration. This part of the work suggests the importance of feature extraction analysis in characterizing the signal from the process with different laser weld parameters that affect weld penetration.

Extensively, commonly used signal features were extracted from the analysis of time-domain, frequency-domain, and time-frequency representations of the acquired sound. This was carried out to understand how these features can be used to characterize a sound from different process parameters. In more detail, mean absolute deviation (MAD), standard deviation (SD), kurtosis, L-Cv, L-kurtosis, bandpower, and cumulative synchrosqueezed wavelet coefficient (CSqWC) were extracted from the previously mentioned analyses. Among the features, SD recorded the best linear trend in response to the change in the involved weld parameters even though the correlation seemed relatively weak. This trend verified the importance of exploring other signal processing methods for feature extraction when dealing with a signal acquired from the PW process.

137

In response to the previous matter, the use of the multi-lag phase space (MPLS) algorithm was explored. Based on the simulation results, the drawbacks of using the MLPS method were identified. The result revealed that noise from the signal affected the fitting process and reduced the MLPS value accordingly. Due to this reason, the original algorithm of the MLPS method was modified by adding the thresholding method to suppress the effect of noise. The localized crest factor (CF) thresholding method was introduced, and the significance of this method in optimizing the MLPS value was presented. Using the modified algorithm, the MLPS was extracted from the acquired sound signal from the process with various laser peak power levels and pulse durations. The results showed an improvement in the linearity trend as compared to other features.

Apart from identifying the features that sensitively responded to the change in weld parameters, the importance of developing a model to estimate the weld penetration was also emphasized. Prior to developing the model, the significant features that were strongly related to the change in weld penetration were identified from the feature selection analysis. Results from the feature selection analysis revealed that the SD, L-kurtosis, and MLPS of the acquired sound were strongly related to the weld penetration. Better correlations were obtained when the laser peak power and pulse duration were also considered. Two models were developed by learning the trend of SD, L- kurtosis, MLPS, laser peak power, and laser pulse duration using the multiple linear regression (MLR) and artificial neural network (ANN) methods. The validation analysis showed that both models could estimate the weld penetration with an average error of less than 8%. A comparison between both models showed that the model developed using the ANN method was more accurate and precise. Hence, the use of ANN model was suggested to be significant if the selection between both models need to be made in order to develop the monitoring system in future.

In summary, the results from this study evidently show the need for an extensive study of the signal processing algorithm for the case of PW laser welding. Despite a higher signal-to-noise ratio (SNR) sound emitted from the PW laser welding, the results from this study also prove that the influence of noise remains a major challenge. The signal processing algorithm developed in this study was found significant to address this issue. Moreover, it might also play a role in extending the options for analyzing the

sound signals acquired from the variation in laser welding process. On the other hand, the estimation models developed from this work prove the possibility of using the acoustic methods to quantitatively monitor weld penetration during PW laser welding on an online basis. This could promote the advancement of the feedback control system in the future.
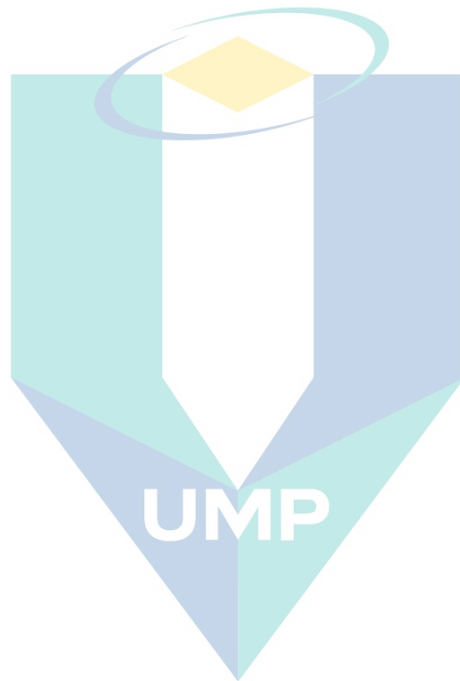
CHAPTER 5

CONCLUSION

5.1   Introduction

One of the objectives in this study was to investigate the characteristic of the acquired sound signal from the PW process. The results showed that transient-type signal occurred, and weak amplitude increment was recorded as the laser peak power increased. Consequently, most of the statistical features used in this study failed to characterize the signal based on the penetration condition. Besides that, the dominant frequency of the acquired signal spectrum was recorded between 5960 Hz and 6440 Hz without a distinguishable trend with respect to the change in weld parameters. This finding suggests the need to develop new algorithm for extracting sound features that sensitively respond to the change in weld penetration, as well as suppressing the noise.

The second objective of study was to develop an algorithm for extracting the sound features and simultaneously eliminating noise. In this study, the feature extraction algorithm was developed by adopting the recently introduced MLPS method. Modification on the MLPS method was done by embedding new thresholding technique into its original algorithm. The results showed that this modification significantly optimized the value of MLPS. Furthermore, the feature selection analysis revealed that this feature was give significant correlation with the weld penetration. This finding contributes to the options for analyzing the sound signal acquired from the wide variation in laser welding process. This is important to enhance the capability of the acoustic method as an online monitoring technique.

The last aim of this study was to develop the prediction model that capable of estimating the weld penetration during PW process. Two models were developed in this study using MLR and ANN methods. Validation experiment showed that both models were significantly able to estimate the weld depth with less than 8% of error. Comparing both models, the ANN prediction model recorded the lowest average of estimation error and SD error. These findings show that it is possible to quantitatively

characterize the weld penetration from PW laser welding with a suitable feature extraction algorithm and model development approaches.

Overall, the results in this study suggest that in the case of PW welding, the sound was emitted with different behaviors which give a different challenge to analyze the signal and develop the prediction model. With an appropriate algorithm for signal processing, the capability of the acoustic methods to monitor the weld penetration could be extended into the PW process. Aligned with the criteria of Industry 4.0, which also emphasize the importance of a monitoring system, this study gives an alternative solution for developing a system that is not limited to the monitoring process only, but also makes a quantitative assessment on the weld penetration condition.

5.2   Recommendation

Since this study was limited to the scope set initially, it is essential to extend this study on several angles. It is vital to improve the capability and flexibility of the acoustic methods in monitoring the laser welding process, covering wide variation in laser machine and process. Basically, in this study, future work recommendations were made based on two significant angles, namely process variation and system expansion.

Looking into the angle of process variation,

a)   It was learned that the process could vary based on the types of material. As previously explained, boron steel grade 22MnB5 was used in this study. Earlier studies suggest that the variation in the types of steel does not produce any significant difference in sound behavior because sound is mainly influenced by the plasma plume and molten metal density, which is closely related to the major chemical element (iron (Fe)). However, other types of material, such as magnesium, aluminum, titanium, and so forth may give different responses as the major element in the chemical composition is different. Moreover, other studies revealed that some of the materials could not reach the stability of process easily due to several factors. This might influence the dynamic behavior of the emerged sound, which is vital to look into.

b)   Besides that, the process can also be varied from the laser machine and weld configurations. In this study, the thickness of the material was 1.8 mm. To extend the robustness of the acoustic methods, it is essential to look into the

response of sound from a higher power PW laser when welding a thicker material because the empirical model developed in this study could only estimate weld penetration up to 1.8 mm. Moreover, the behavior of the plasma plume might be dynamically changed due to the deeper weld penetration.

c)   Moreover, it is important to investigate the formation of sound from a higher average power laser machine. Studies evidently show that a higher laser intensity tends to produce a fusion zone with a higher aspect ratio. However, the process stability is difficult to be achieved, and it is significant if the capability of the acoustic methods can be investigated under these circumstances.

d)   On the other hand, other weld configurations, such as lap joints can experience a different challenge. This will lead to different behaviors in molten metal and keyhole dynamics, which may introduce defects in different manners. Therefore, it is important to extend the study to all these variations to look into how the acquired sound responds to the penetration condition and other types of defects.

e)   In the preliminary experiment, it was explained that the experiment was designed to achieve weld joint with a minimal occurrence of defect. However, the effect of heat input is not within the scope of study because the main aim is to assess the penetration condition. Theoretically, heat input affects the mechanical properties of weld joint. Therefore, it is significant if the study can look into the characteristics of sound from different heat inputs in the future.

Meanwhile, by looking into the potential of system expansion, several recommendations were made:

a)   As initially explained, this work focused on modifying the MLPS method by adding a simple and fast processing thresholding method. A comparison was made with commonly used thresholding methods in the wavelet analysis. It is significant to extend the comparison study by looking into another type of de-noising method. This is to ensure the robustness of this framework for a wide variety of laser welding applications, which are not limited to the scope of experiment set in this study.

b)   On the other hand, it was explained that the selection of threshold limit for the proposed de-noising method was 2, which was twice the average signal energy.

Even though the stability of this threshold limit toward the small changes in the amplitude of the sound signal has been proven, it will be significant if the study can be extended to find the optimum value of this type of threshold. This part of extensive work is also important to ensure that this method is applicable under the circumstances outside the scope of this study.

As previously explained, the framework developed in this study offers an alternative in developing a monitoring system on a real-time basis. Since manufacturing process automation is in high demand lately, it is essential to look into how this study can contribute to the development of a control system. This is important to address the future needs in the era of industrial revolution.
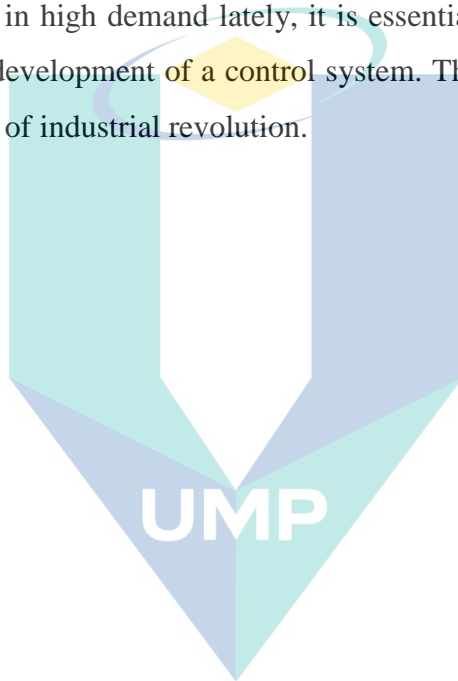
REFERENCES

Abbasi, M. , Ketabchi, M., Shakeri, H. R. , & Shafaat, M. A. (2011). Obtaining high formability of IF-galvanized steel tailor welded blanks by applying optimum CO2 laser welding parameters. *International journal of materials research, 102*(10), 1295-1302. doi: doi:10.3139/146.110580

Abbasi, Z., Yuhas, D., Zhang, L., Basantes, A. D. C., Tehrani, N. N., Ozevin, D., & Indacochea, E. (2018). The Detection of Burn-Through Weld Defects Using Noncontact Ultrasonics *Materials, 11*(1), 128.

Akman, E., Demir, A., Canel, T., & Sınmazçelik, T. (2009). Laser welding of Ti6Al4V titanium alloys. *Journal of Materials Processing Technology, 209*(8), 3705-3713. doi: https://doi.org/10.1016/j.jmatprotec.2008.08.026

Ali, M. (1999). *In-process quality monitoring of laser welds using multi-sensor measurements.* The Ohio State University.

Amara, E. H., & Fabbro, R. (2010). Modeling of humps formation during deep-penetration laser welding. *Applied Physics A, 101*(1), 111-116. doi: 10.1007/s00339-010-5768-z

Ao, S., Luo, Z., Feng, M., & Yan, F. (2015). Simulation and experimental analysis of acoustic signal characteristics in laser welding. *The International Journal of Advanced Manufacturing Technology, 81*(1), 277-287. doi: 10.1007/s00170-015-7164-5

Ao, S., Luo, Z., Nan, Z., & Rui, W. (2010, 18-20 Dec. 2010). *Blind Source Separation Based on Principal Component Analysis-Independent Component Analysis for Acoustic Signal During Laser Welding Process.* Paper presented at the 2010 International Conference on Digital Manufacturing & Automation.

Arbel, Arie F. (1984). *Analog signal processing and instrumentation*: CUP Archive.

Assuncao, E., & Williams, S. (2013). Comparison of continuous wave and pulsed wave laser welding effects. *Optics and Lasers in Engineering, 51*(6), 674-680. doi: https://doi.org/10.1016/j.optlaseng.2013.01.007

Assuncao, Eurico, Williams, Stewart, & Yapp, David. (2012). Interaction time and beam diameter effects on the conduction mode limit. *Optics and Lasers in Engineering, 50*(6), 823-828. doi: https://doi.org/10.1016/j.optlaseng.2012.02.001

Babyak, Michael A. (2004). What You See May Not Be What You Get: A Brief, Nontechnical Introduction to Overfitting in Regression-Type Models. *Psychosomatic medicine, 66*(3), 411-421.

Bakshi, S., Javid, I., Rajoriya, M., Naz, S., Gupta, P., Sahni, M., & Singh, M. (2019, 18-19 Oct. 2019). *Designand Comparison Between IIR Butterwoth and Chebyshev Digital Filters Using Matlab.* Paper presented at the 2019 International Conference on Computing, Communication, and Intelligent Systems (ICCCIS).

Bandyopadhyay, K., Panda, S. K., & Saha, P. (2016). Optimization of Fiber Laser Welding of DP980 Steels Using RSM to Improve Weld Properties for Formability. *Journal of Materials Engineering and Performance, 25*(6), 2462-2477. doi: 10.1007/s11665-016-2071-y

Bao, W., Tu, X., Hu, C., & Li, F. . (2020). Envelope Spectrum L-Kurtosis and Its Application for Fault Detection of Rolling Element Bearings. *IEEE Transactions on Instrumentation and Measurement, 69*(5), 1993-2002. doi: 10.1109/TIM.2019.2917982

Barbarino, S., Grasso, F., Guerriera, G., Musumeci, F., Scordino, A., & Triglia, A. (1982). Surface roughness effect on optical absorptivity of metals. *Applied Physics A, 29*(2), 77-80. doi: 10.1007/BF00632430

Baren, John Van , Van Baren, Phillip, & Jenison, MI. (2012). The fatigue damage spectrum and kurtosis control. *Sound and Vibration, 46*(10), 10.

Bastuck, M., Herrmann, H. G., Wolter, B., Bottger, D., & Zinn, P. C. (2016). *AkuProLas: Acoustic Inline Process Monitoring for Laser Welding Applications.* Paper presented at the World Conference on Nondestructive Testing (19): WCNDT 2016.

Berger, P., Hügel, H., & Graf, T. (2011). Understanding Pore Formation in Laser Beam Welding. *Physics Procedia, 12*, 241-247. doi: https://doi.org/10.1016/j.phpro.2011.03.031

Bergström, D. (2008). *The absorption of laser light by rough metal surfaces.* (2008:08 Doctoral thesis, comprehensive summary), Luleå tekniska universitet, Luleå. Retrieved from http://urn.kb.se/resolve?urn=urn:nbn:se:ltu:diva-26182 DiVA database.

Bergström, D., Powell, J., & Kaplan, A. F. H. (2007). The absorptance of steels to Nd:YLF and Nd:YAG laser light at room temperature. *Applied Surface Science, 253*(11), 5017-5028. doi: https://doi.org/10.1016/j.apsusc.2006.11.018

Bernard, C., Petrut, T., Vasile, G., & Ioana, C. (2014, 1-5 Sept. 2014). *Multi-lag phase space representations for transient signals characterization.* Paper presented at the 2014 22nd European Signal Processing Conference (EUSIPCO).

Berto, F., Campagnolo, A., Chebat, F., Cincera, M., & Santini, M. (2016). Fatigue strength of steel rollers with failure occurring at the weld root based on the local strain energy values: modelling and fatigue assessment. *International Journal of Fatigue, 82*, 643-657. doi: https://doi.org/10.1016/j.ijfatigue.2015.09.023

Bertrand, P., Smurov, I., & Grevey, D. (2000). Application of near infrared pyrometry for continuous Nd:YAG laser welding of stainless steel. *Applied Surface Science, 168*(1), 182-185. doi: https://doi.org/10.1016/S0169-4332(00)00586-9

Bhadra, Rakesh, Biswas, Pankaj, & Ravi Sankar, M. (2015). A Literature Review on CO2 Laser Welding. In Shrikrishna N. Joshi & Uday Shanker Dixit (Eds.), *Lasers Based Manufacturing: 5th International and 26th All India Manufacturing Technology, Design and Research Conference, AIMTDR 2014* (pp. 381-398). New Delhi: Springer India.

Bindusri, M., & Rao, S. K. (2019). Sunspot data denoising using wavelet. *Int. J. Innov. Technol. Explor. Eng., 8*(4), 230-236.

Bishop, C. M. (2006). *Pattern recognition and machine learning*: springer.

Böllinghaus, T., Gumenyuk, A., & Quiroz, V. (2011). Short Term Metallurgy and Hot Cracking During Laser Beam Welding of Austenitic Stainless Steels. In Thomas Böllinghaus, John Lippold, & Carl E. Cross (Eds.), *Hot Cracking Phenomena in Welds III* (pp. 103-129). Berlin, Heidelberg: Springer Berlin Heidelberg.

Boulton, C. F. (1976). Fatigue life predictions of welded specimens containing lack of penetration defects at ambient and elevated temperatures. *International Journal of Pressure Vessels and Piping, 4*(3), 171-195. doi: https://doi.org/10.1016/0308-0161(76)90020-X

Caprio, L., Demir, A., & Previtali, B. (2018). Comparative study between CW and PW emissions in selective laser melting. *Journal of Laser Applications, 30*(3), 032305. doi: 10.2351/1.5040631

Carrolo, V. S. (2010). Laser welding distortions on thin plates. *Technical university of Lisbon, department of mechanical engineering. Lisbon:[viitattu 18.6. 2014]. Konetekniikan pro gradu-tutkielman artikkeli.*

Chang, B., Blackburn, J., Allen, C., & Hilton, P. (2016). Studies on the spatter behaviour when welding AA5083 with a Yb-fibre laser. *The International Journal of Advanced Manufacturing Technology, 84*(9), 1769-1776. doi: 10.1007/s00170-015-7863-y

Chelladurai, A. M., Gopal, K. A., Murugan, S., Venugopal, S., & Jayakumar, T. (2015). Energy Transfer Modes in Pulsed Laser Seam Welding. *Materials and Manufacturing Processes, 30*(2), 162-168. doi: 10.1080/10426914.2014.965829

Chen, C., Xiao, R., Chen, H., Lv, N., & Chen, S. (2020). Prediction of welding quality characteristics during pulsed GTAW process of aluminum alloy by multisensory fusion and hybrid network model. *Journal of Manufacturing Processes*. doi: https://doi.org/10.1016/j.jmapro.2020.08.028

Chen, L., Reeve, J., Zhang, L., Huang, S., Wang, X., & Chen, J. (2018). GMPR: A robust normalization method for zero-inflated count data with application to microbiome sequencing data. *PeerJ, 6*, e4600.

Chen, M., Xu, J., Xin, L., Zhao, Z., Wu, F., Ma, S., & Zhang, Y. (2017). Effect of keyhole characteristics on porosity formation during pulsed laser-GTA hybrid welding of AZ31B magnesium alloy. *Optics and Lasers in Engineering, 93*, 139-145. doi: https://doi.org/10.1016/j.optlaseng.2017.01.018

Chen, Z., Ding, Y., Ren, S., & Chen, Z. (2018). A Novel Noncircular MUSIC Algorithm Based on the Concept of the Difference and Sum Coarray. *Sensors, 18*(2), 344.

Chengning, Z., Min, X., Mingyang, Z., & Haibo, L. (2010, 7-10 Dec. 2010). *On line quality inspection in tailor welded blank based on laws texture energy and structured light.* Paper presented at the 2010 11th International Conference on Control Automation Robotics & Vision.

Chmelíčková, Hana, & Šebestová, Hana. (2012). Pulsed laser welding *Nd YAG laser*: IntechOpen.

Daubechies, Ingrid, Lu, Jianfeng, & Wu, Hau-Tieng. (2011). Synchrosqueezed wavelet transforms: An empirical mode decomposition-like tool. *Applied and Computational Harmonic Analysis, 30*(2), 243-261. doi: https://doi.org/10.1016/j.acha.2010.08.002

Dausinger, F., & Shen, J. (1993). Energy Coupling Efficiency in Laser Surface Treatment. *ISIJ international, 33*(9), 925-933. doi: 10.2355/isijinternational.33.925

Dawes, C. (1992). *Laser welding: a practical guide*: Woodhead Publishing.

Devnath, L., Nath, S. K., Das, A. K., & Islam, M. R. (2015). Selection of Wavelet and thresholding rule for denoising the ECG signals. *Annals of pure and applied mathematics, 10*(1), 65-73.

Digulescu, A., Murgan, I., Ioana, C., Candel, I., & Serbanescu, A. (2016). *Applications of Transient Signal Analysis Using the Concept of Recurrence Plot Analysis*, Cham.

Digulescu, Angela, Ioana, Cornel, & Serbanescu, Alexandru. (2019). Phase Diagram-Based Sensing with Adaptive Waveform Design and Recurrent States Quantification for the Instantaneous Frequency Law Tracking. *Sensors, 19*(11). doi: 10.3390/s19112434

Dowling, A. P., & Ffowcs Williams, J. E. (1983). *Sound and sources of sound*: Horwood.

Dreyfus, G. (2005). *Neural networks: methodology and applications*: Springer Science & Business Media.

Duley, W. W., & Mao, Y. L. (1994). The effect of surface condition on acoustic emission during welding of aluminium with CO2laser radiation. *Journal of Physics D: Applied Physics, 27*(7), 1379-1383. doi: 10.1088/0022-3727/27/7/007

Durak, L., & Arikan, O. (2003). Short-time Fourier transform: two fundamental properties and an optimal implementation. *IEEE Transactions on Signal Processing, 51*(5), 1231-1242. doi: 10.1109/TSP.2003.810293

Efroymson, MA. (1960). Multiple regression analysis. *Mathematical methods for digital computers*, 191-203.

Eriksson, I., Powell, J., & Kaplan, A. F. H. (2013). Melt behavior on the keyhole front during high speed laser welding. *Optics and Lasers in Engineering, 51*(6), 735-740. doi: https://doi.org/10.1016/j.optlaseng.2013.01.008

Eriksson, Ingemar, Gren, Per, Powell, John, & Kaplan, Alexander. (2010). New high-speed photography technique for observation of fluid flow in laser welding. *Optical Engineering, 49*(10), 100503.

Faerber, M. (1995). Gases for increased productivity of laser processing. *Optical and Quantum Electronics, 27*(12), 1449-1455. doi: 10.1007/BF00326496

Fahrmeir, L., Kneib, T., Lang, S., & Marx, B. (2013). Regression Models *Regression: Models, Methods and Applications* (pp. 21-72). Berlin, Heidelberg: Springer Berlin Heidelberg.

Farson, D, Ali, A, & Sang, Yan. (1998). Relationship of optical and acoustic emissions to laser weld penetration. *Welding journal, 77*(4), 142. s-148. s.

Farson, D, Hillsley, K, Sames, J, & Young, R. (1996). Frequency–time characteristics of air-borne signals from laser welds. *Journal of Laser Applications, 8*(1), 33-42.

Farson, D. F., Ali, A., & Li, X. C. (1999). Laser weld penetration monitoring with multiple emission signal measurements. *Journal of Laser Applications, 11*(2), 47-53. doi: 10.2351/1.521887

Farson, D. F., & Kim, K. R. (1999). Generation of optical and acoustic emissions in laser weld plumes. *Journal of Applied Physics, 85*(3), 1329-1336. doi: 10.1063/1.369263

Fidali, M. (2018, 2018//). *Detection of Welding Process Instabilities Using Acoustic Signals.* Paper presented at the Advances in Technical Diagnostics, Cham.

Fish, P. J. (2017). *Electronic noise and low noise design*: Macmillan International Higher Education.

Frewin, M. R., & Scott, D. A. (1999). Finite element model of pulsed laser welding. *WELDING JOURNAL-NEW YORK-, 78*, 15-s.

Frostevarg, J., & Kaplan, A. F. H. (2014). Undercuts in Laser Arc Hybrid Welding. *Physics Procedia, 56*, 663-672. doi: https://doi.org/10.1016/j.phpro.2014.08.071

Gao, Q., Xiang, J., Hou, S., Tang, H., Zhong, Y., & Ye, S. (2021). Method using L-kurtosis and enhanced clustering-based segmentation to detect faults in axial piston pumps. *Mechanical Systems and Signal Processing, 147*, 107130. doi: https://doi.org/10.1016/j.ymssp.2020.107130

Gao, X. L., Zhang, L. J., Liu, J. T., & Zhang, J. X. (2014). Porosity and microstructure in pulsed Nd:YAG laser welded Ti6Al4V sheet. *Journal of Materials Processing Technology, 214*(7), 1316-1325. doi: https://doi.org/10.1016/j.jmatprotec.2014.01.015

Gao, X., You, D., & Katayama, S. (2012). Infrared image recognition for seam tracking monitoring during fiber laser welding. *Mechatronics, 22*(4), 370-380. doi: https://doi.org/10.1016/j.mechatronics.2011.09.005

Gao, Xiao-Long, Zhang, Lin-Jie, Liu, Jing, & Zhang, Jian-Xun. (2014). Porosity and microstructure in pulsed Nd:YAG laser welded Ti6Al4V sheet. *Journal of Materials Processing Technology, 214*(7), 1316-1325. doi: https://doi.org/10.1016/j.jmatprotec.2014.01.015

García-Laencina, P. J., Sancho-Gómez, J. L., & Figueiras-Vidal, A. R. (2010). Pattern classification with missing data: a review. *Neural Computing and Applications, 19*(2), 263-282. doi: 10.1007/s00521-009-0295-6

Giurgiutiu, V., & Yu, L. (2003). *Comparison of short-time fourier transform and wavelet transform of transient and tone burst wave propagation signals for structural health monitoring*. Paper presented at the Proceedings of 4th international workshop on structural health monitoring.

Gratzke, U., Kapadia, P. D., Dowden, J., Kroos, J., & Simon, G. (1992). Theoretical approach to the humping phenomenon in welding processes. *Journal of Physics D: Applied Physics, 25*(11), 1640-1647. doi: 10.1088/0022-3727/25/11/012

Gu, H., & Duley, W. W. (1996). A statistical approach to acoustic monitoring of laser welding. *Journal of Physics D: Applied Physics, 29*(3), 556-560. doi: 10.1088/0022-3727/29/3/011

Guo, Ning, Xing, Xiao, Zhao, Hongyun, Tan, Caiwang, Feng, Jicai, & Deng, Zongquan. (2017). Effect of water depth on weld quality and welding process in underwater fiber laser welding. *Materials & Design, 115*, 112-120. doi: https://doi.org/10.1016/j.matdes.2016.11.044

Gupta, A., Nelwamondo, F., Mohamed, S., Ennett, C., & Frize, M. *Statistical Normalization and Back Propagation for Classification*.

Hazra, A. (2017). Using the confidence interval confidently. *Journal of thoracic disease, 9*(10), 4125.

He, C., Xing, J., Li, J., Yang, Q., & Wang, R. (2015). A New Wavelet Threshold Determination Method Considering Interscale Correlation in Signal Denoising. *Mathematical Problems in Engineering, 2015*, 280251. doi: 10.1155/2015/280251

Heider, A, Engelhardt, T, Weber, R, & Graf, T. (2015). *Influence of Ambient Pressure on Spatter Formation during Laser Welding of Copper.* Paper presented at the Proc. of the int. WLT-Conference on Lasers in Manufacturing (Munich).

Hoffman, J., Szymanski, Z., Jakubowski, J., & Kolasa, A. (2002). Analysis of acoustic and optical signals used as a basis for controlling laser-welding processes. *Welding International, 16*(1), 18-25. doi: 10.1080/09507110209549484

Hong, K. M., & Shin, Y. C. (2017). Prospects of laser welding technology in the automotive industry: A review. *Journal of Materials Processing Technology, 245*, 46-69. doi: https://doi.org/10.1016/j.jmatprotec.2017.02.008

Hosking, J. R. M. (1990). L-Moments: Analysis and Estimation of Distributions Using Linear Combinations of Order Statistics. *Journal of the Royal Statistical Society: Series B (Methodological), 52*(1), 105-124. doi: https://doi.org/10.1111/j.2517-6161.1990.tb01775.x

Hosking, J. R. M. (1992). Moments or L Moments? An Example Comparing Two Measures of Distributional Shape. *The American Statistician, 46*(3), 186-189. doi: 10.1080/00031305.1992.10475880

Huang, R. S., Kang, L., & Ma, X. (2008). Microstructure and Phase Composition of a Low-Power YAG Laser-MAG Welded Stainless Steel Joint. *Journal of Materials Engineering and Performance, 17*(6), 928-935. doi: 10.1007/s11665-008-9241-5

Huang, W., & Kovacevic, R. (2009). Feasibility study of using acoustic signals for online monitoring of the depth of weld in the laser welding of high-strength steels. *Proceedings of the Institution of Mechanical Engineers, Part B: Journal of Engineering Manufacture, 223*(4), 343-361. doi: 10.1243/09544054JEM1320

Huang, W., & Kovacevic, R. (2011). A neural network and multiple regression method for the characterization of the depth of weld penetration in laser welding based on acoustic signatures. *Journal of Intelligent Manufacturing, 22*(2), 131-143. doi: 10.1007/s10845-009-0267-9

Iatsenko, Dmytro, McClintock, Peter V. E., & Stefanovska, Aneta. (2015). Linear and synchrosqueezed time–frequency representations revisited: Overview, standards of use, resolution, reconstruction, concentration, and algorithms. *Digital Signal Processing, 42*, 1-26. doi: https://doi.org/10.1016/j.dsp.2015.03.004

Jan, J. (2000). *Digital signal filtering, analysis and restoration*: IET.

Jerbic, A. B , Horki, P. , Sovilj, S., Isgum, V., & Cifrek, M. (2015, 2015//). *Hilbert-Huang Time-Frequency Analysis of Motor Imagery EEG Data for Brain-Computer Interfaces.* Paper presented at the 6th European Conference of the International Federation for Medical and Biological Engineering, Cham.

Jiang, Z., Tao, W., Yu, K., Tan, C., Chen, Y., Li, L., & Li, Z. (2016). Comparative study on fiber laser welding of GH3535 superalloy in continuous and pulsed waves. *Materials & Design, 110*, 728-739. doi: https://doi.org/10.1016/j.matdes.2016.08.055

Jones, Morgan. (2013). *Building valve amplifiers*: Newnes.

Kadoi, K., Fujinaga, A., Yamamoto, M., & Shinozaki, K. (2013). The effect of welding conditions on solidification cracking susceptibility of type 310S stainless steel during laser welding using an in-situ observation technique. *Welding in the World, 57*(3), 383-390. doi: 10.1007/s40194-013-0023-9

Kamen, E. W., & Heck, B. S. (2006). *Fundamentals of signals and systems using the web and matlab*: Prentice-Hall, Inc.

Kaplan, A. F. H., & Powell, J. (2011). Spatter in laser welding. *Journal of Laser Applications, 23*(3), 032005. doi: 10.2351/1.3597830

Karthikeyan, P, Murugappan, M, & Yaacob, S. (2012). ECG signal denoising using wavelet thresholding techniques in human stress assessment. *International Journal on Electrical Engineering and Informatics, 4*(2), 306.

Katayama, S. (2013). 12 - Defect formation mechanisms and preventive procedures in laser welding. In Seiji Katayama (Ed.), *Handbook of Laser Welding Technologies* (pp. 332-373): Woodhead Publishing.

Katayama, S. (2018). 7 - Understanding and Improving Process Control in Pulsed and Continuous Wave Laser Welding☆. In Jonathan Lawrence (Ed.), *Advances in Laser Materials Processing (Second Edition)* (pp. 153-183): Woodhead Publishing.

Kawahito, Y., Katayama, S., & Nakamura, H. (2015). Fundamental Study for the Relationship between Melt Flow and Spatter in High-Power Laser Welding of Pure Titanium. *Transactions of JWRI, 44*(2), 27-32.

Kawahito, Y., Mizutani, M., & Katayama, S. (2009). High quality welding of stainless steel with 10 kW high power fibre laser. *Science and Technology of Welding and Joining, 14*(4), 288-294. doi: 10.1179/136217108X372531

Kelkar, G. (2008). Pulsed laser welding. *WJM Technologies, Cerritos*.

Kinsey, Brad, Liu, Zhihong, & Cao, Jian. (2000). A novel forming technology for tailor-welded blanks. *Journal of Materials Processing Technology, 99*(1), 145-153. doi: https://doi.org/10.1016/S0924-0136(99)00412-4

Klein, T., Vicanek, M., Kroos, J., Decker, I., & Simon, G. (1994). Oscillations of the keyhole in penetration laser beam welding. *Journal of Physics D: Applied Physics, 27*(10), 2023-2030. doi: 10.1088/0022-3727/27/10/006

Kong, F., Ma, J., Carlson, B., & Kovacevic, R. (2012). Real-time monitoring of laser welding of galvanized high strength steel in lap joint configuration. *Optics & Laser Technology, 44*(7), 2186-2196. doi: https://doi.org/10.1016/j.optlastec.2012.03.003

Kriesel, D. (2007). A brief introduction on neural networks.

Kroos, J., Gratzke, U., & Simon, G. (1993). Towards a self-consistent model of the keyhole in penetration laser beam welding. *Journal of Physics D: Applied Physics, 26*(3), 474-480. doi: 10.1088/0022-3727/26/3/021

Kuo, T. Y. (2005). Effects of pulsed and continuous Nd–YAG laser beam waves on welding of Inconel alloy. *Science and Technology of Welding and Joining, 10*(5), 557-565. doi: 10.1179/174329305X46709

Kuryntsev, S. V., Morushkin, A. E., & Gilmutdinov, A. Kh. (2017). Fiber laser welding of austenitic steel and commercially pure copper butt joint. *Optics and Lasers in Engineering, 90*, 101-109. doi: https://doi.org/10.1016/j.optlaseng.2016.10.008

Lassami, N., Aïssa-El-Bey, A., & Abed-Meraim, K. (2020). Low cost sparse subspace tracking algorithms. *Signal Processing, 173*, 107522. doi: https://doi.org/10.1016/j.sigpro.2020.107522

Lawrence, FV, & Munse, WH. (1973). Fatigue crack propagation in butt welds containing joint penetration defects. *Welding journal, 52*(5).

Lee, C. J., Kim, J. D., & Kim, Y. C. (2015). Study on monitoring of plasma emission signal in lap welding of Zn coated steel sheet using CO2 laser. *International Journal of Precision Engineering and Manufacturing, 16*(3), 495-500. doi: 10.1007/s12541-015-0067-4

Lee, Seounghwan, Ahn, Suneung, & Park, Changsoon. (2014). Analysis of Acoustic Emission Signals During Laser Spot Welding of SS304 Stainless Steel. *Journal of Materials Engineering and Performance, 23*(3), 700-707. doi: 10.1007/s11665-013-0791-9

Lewis, GK, & Dixon, RD. (1985). Plasma monitoring of laser beam welds. *Laser, 13*, 2.

Li, H. (2010). *Complex Morlet wavelet amplitude and phase map based bearing fault diagnosis.* Paper presented at the 2010 8th World Congress on Intelligent Control and Automation.

Li, K., Lu, F., Guo, S., Cui, H., & Tang, X. (2015). Porosity sensitivity of A356 Al alloy during fiber laser welding. *Transactions of Nonferrous Metals Society of China, 25*(8), 2516-2523. doi: https://doi.org/10.1016/S1003-6326(15)63870-5

Li, L. (2002). A comparative study of ultrasound emission characteristics in laser processing. *Applied Surface Science, 186*(1), 604-610. doi: https://doi.org/10.1016/S0169-4332(01)00695-X

Li, L., Brookfield, D. J., & Steen, W. M. (1996). Plasma charge sensor for in-process, non-contact monitoring of the laser welding process. *Measurement Science and Technology, 7*(4), 615-626. doi: 10.1088/0957-0233/7/4/019

Li, M. M. (2011). 1 - Weld integrity of tailor welded blanks. In Brad L. Kinsey & Xin Wu (Eds.), *Tailor Welded Blanks for Advanced Manufacturing* (pp. 3-23): Woodhead Publishing.

Li, S. C., Chen, G. Y., Katayama, S., & Zhang, Y. (2014). Relationship between spatter formation and dynamic molten pool during high-power deep-penetration laser welding. *Applied Surface Science, 303*, 481-488. doi: https://doi.org/10.1016/j.apsusc.2014.03.030

Li, Shichun, Chen, Genyu, & Zhou, Cong. (2015). Effects of welding parameters on weld geometry during high-power laser welding of thick plate. *The International Journal of Advanced Manufacturing Technology, 79*(1), 177-182. doi: 10.1007/s00170-015-6813-z

Liu, H., & Shi, Z. (2020). A Fault Detection Approach Using Variational Mode Decomposition, L-kurtosis and Random Decrement Technique for Rotating Machinery. *International Journal of Mechanical Engineering and Applications, 8*(1), 16.

Liu, J. T., Weckman, D. C., & Kerr, H. W. (1993). The effects of process variables on pulsed Nd:YAG laser spot welds: Part I. AISI 409 stainless steel. *Metallurgical Transactions B, 24*(6), 1065-1076. doi: 10.1007/BF02660998

Liu, L., Shi, J., Hou, Z., & Song, G. (2018). Effect of distance between the heat sources on the molten pool stability and burn-through during the pulse laser-GTA hybrid welding process. *Journal of Manufacturing Processes, 34*, 697-705. doi: https://doi.org/10.1016/j.jmapro.2018.06.038

Liu, Q., Zhou, Q., Venezuela, J., Zhang, M. J., & Atrens, A. (2018). The role of the microstructure on the influence of hydrogen on some advanced high-strength steels. *Materials Science and Engineering: A, 715*, 370-378. doi: https://doi.org/10.1016/j.msea.2017.12.079

Liu, S., Hou, S., He, K., & Yang, W. (2018). L-Kurtosis and its application for fault detection of rolling element bearings. *Measurement, 116*, 523-532. doi: https://doi.org/10.1016/j.measurement.2017.11.049

Lopes, J. C., Ribeiro, F. S. F., Javaroni, R. L., Garcia, M. V., Ventura, C. E. H., Scalon, V. L., . . . Bianchi, E. C. (2020). Mechanical and thermal effects of abrasive cut-off applied in low and medium carbon steels using aluminum oxide cutting disc. *The International Journal of Advanced Manufacturing Technology, 109*(5), 1319-1331. doi: 10.1007/s00170-020-05753-5

Luo, Z., Liu, W., Wang, Z., & Ao, S. (2016). Monitoring of laser welding using source localization and tracking processing by microphone array. *The International Journal of Advanced Manufacturing Technology, 86*(1), 21-28. doi: 10.1007/s00170-015-8095-x

Lv, C., Xing, Y., Zhang, J., Na, X., Li, Y., Liu, T., . . . Wang, F. (2018). Levenberg–Marquardt Backpropagation Training of Multilayer Neural Networks for State Estimation of a Safety-Critical Cyber-Physical System. *IEEE Transactions on Industrial Informatics, 14*(8), 3436-3446. doi: 10.1109/TII.2017.2777460

Malek, G. F., Hamedi, M. J., Torkamany, M. J., & Sabbaghzadeh, J. (2007). Weld metal microstructural characteristics in pulsed Nd: YAG laser welding. *Scripta Materialia, 56*(11), 955-958. doi: https://doi.org/10.1016/j.scriptamat.2007.02.019

Marquardt, D. W. (1963). An Algorithm for Least-Squares Estimation of Nonlinear Parameters. *Journal of the Society for Industrial and Applied Mathematics, 11*(2), 431-441. doi: 10.1137/0111030

Martukanitz, Richard. (2005). *A critical review of laser beam welding* (Vol. 5706): SPIE.

Masoumi, M., Ariza, E. A., Sinatora, A., & Goldenstein, H. (2018). Role of crystallographic orientation and grain boundaries in fatigue crack propagation in used pearlitic rail steel. *Materials Science and Engineering: A, 722*, 147-155. doi: https://doi.org/10.1016/j.msea.2018.03.028

Matsunawa, A., Katayama, S., Ikeda, H., & Nishizawa, K. (1992). Effect of pulse shaping on defect reduction in pulsed laser welding. *International Congress on Applications of Lasers & Electro-Optics, 1992*(1), 547-556. doi: 10.2351/1.5058527

Meng, W., Li, Z., Lu, F., Wu, Y., Chen, J., & Katayama, S. (2014). Porosity formation mechanism and its prevention in laser lap welding for T-joints. *Journal of Materials Processing Technology, 214*(8), 1658-1664. doi: https://doi.org/10.1016/j.jmatprotec.2014.03.011

Mihov, S. G., Ivanov, R. M., & Popov, A. N. (2009). Denoising speech signals by wavelet transform. *Annual Journal Of Electronics*(6), 2-5.

Miyachi, Amada. (2017). Laser welding fundamentals.

Montgomery, A., Hook, P., Clapham, L., & Wild, P. (2003). Non-destructive evaluation of laser welds in tailor-welded blanks using magnetic flux leakage. *International Congress on Applications of Lasers & Electro-Optics, 2003*(1), 1304. doi: 10.2351/1.5059997

Montgomery, D. C., & Runger, G. C. (2010). *Applied statistics and probability for engineers*: John Wiley & Sons.

Montgomery, Douglas C, Peck, Elizabeth A, & Vining, G Geoffrey. (2012). *Introduction to linear regression analysis* (Vol. 821): John Wiley & Sons.

Montgomery, Douglas C, & Runger, George C. (2014). *Applied statistics and probability for engineers*: Wiley.

Moraitis, G. A., & Labeas, G. N. (2009). Prediction of residual stresses and distortions due to laser beam welding of butt joints in pressure vessels. *International Journal of Pressure Vessels and Piping, 86*(2), 133-142. doi: https://doi.org/10.1016/j.ijpvp.2008.11.004

Nakamura, S., Sakurai, M., Kamimuki, K., Inoue, T., & Ito, Y. (2000). Detection technique for transition between deep penetration mode and shallow penetration mode in CO2laser welding of metals. *Journal of Physics D: Applied Physics, 33*(22), 2941-2948. doi: 10.1088/0022-3727/33/22/311

Nath, A. K., Sridhar, R., Ganesh, P., & Kaul, R. (2002). Laser power coupling efficiency in conduction and keyhole welding of austenitic stainless steel. *Sadhana, 27*(3), 383-392. doi: 10.1007/BF02703659

O'Neill, W., Sparkes, M., Varnham, M., Horley, R., Birch, M., Woods, S., & Harker, A. (2004). High power high brightness industrial fiber laser technology. *International Congress on Applications of Lasers & Electro-Optics, 2004*(1), 301. doi: 10.2351/1.5060263

Olive, D. J. (2017). Multiple Linear Regression *Linear Regression* (pp. 17-83). Cham: Springer International Publishing.

Pakmanesh, M. R., & Shamanian, M. (2018). Optimization of pulsed laser welding process parameters in order to attain minimum underfill and undercut defects in thin 316L stainless steel foils. *Optics & Laser Technology, 99*, 30-38. doi: https://doi.org/10.1016/j.optlastec.2017.09.047

Pang, S., Chen, X., Shao, X., Gong, Sh., & Xiao, J. (2016). Dynamics of vapor plume in transient keyhole during laser welding of stainless steel: Local evaporation, plume

swing and gas entrapment into porosity. *Optics and Lasers in Engineering, 82*, 28-40. doi: https://doi.org/10.1016/j.optlaseng.2016.01.019

Panwisawas, C., Perumal, B., Ward, R. M., Turner, N., Turner, R. P., Brooks, J. W., & Basoalto, H. C. (2017). Keyhole formation and thermal fluid flow-induced porosity during laser fusion welding in titanium alloys: Experimental and modelling. *Acta Materialia, 126*, 251-263. doi: https://doi.org/10.1016/j.actamat.2016.12.062

Pastor, M, Zhao, H, Martukanitz, RP, & DebRoy, T. (1999). Porosity, underfill and magnesium lose during continuous wave Nd: YAG laser welding of thin plates of aluminum alloys 5182 and 5754. *WELDING JOURNAL-NEW YORK-, 78*, 207-s.

Piezotronics, PCB. (2016). PCB 378B02 Microphone Specification. 3425, Walden Avenue, Depew, NY 14043.

Popescu, Diana, & Amza, Catalin. (2017). Additive Manufacturing Automation for Industry 4.0. *Res. & Sci. Today, 13*, 50.

Portnoff, M. (1980). Time-frequency representation of digital signals and systems based on short-time Fourier analysis. *IEEE Transactions on Acoustics, Speech, and Signal Processing, 28*(1), 55-69. doi: 10.1109/TASSP.1980.1163359

Purtonen, T., Kalliosaari, A., & Salminen, A. (2014). Monitoring and Adaptive Control of Laser Processes. *Physics Procedia, 56*, 1218-1231. doi: https://doi.org/10.1016/j.phpro.2014.08.038

Quintino, L., & Assunção, E. (2013). 6 - Conduction laser welding A2 - Katayama, Seiji *Handbook of Laser Welding Technologies* (pp. 139-162): Woodhead Publishing.

Quintino, L., Costa, A., Miranda, R., Yapp, D., Kumar, V., & Kong, C. J. (2007). Welding with high power fiber lasers – A preliminary study. *Materials & Design, 28*(4), 1231-1237. doi: https://doi.org/10.1016/j.matdes.2006.01.009

Rabbi, Navid Fazle. (2021). Design, Implementation, Comparison, and Performance analysis between Analog Butterworth and Chebyshev-I Low Pass Filter Using Approximation, Python and Proteus. *arXiv preprint arXiv:2102.09048*.

Raj, A Stanley, Oliver, D Hudson, Srinivas, Y, & Viswanath, J. (2016). Wavelet denoising algorithm to refine noisy geoelectrical data for versatile inversion. *Modeling Earth Systems and Environment, 2*(1), 36.

Ready, J. F., & Farson, D. F. (2001). LIA Handbook of Laser Materials Processing, Laser Institute of America Magnolia Publishing. *Inc, United State of America*.

Reinhold, Isabella, Sandsten, Maria, & Starkhammar, Josefin. (2018). Objective detection and time-frequency localization of components within transient signals. *The Journal of the Acoustical Society of America, 143*(4), 2368-2378. doi: 10.1121/1.5032215

Rosu, Georgiana, Digulescu, Angela, Candel, Ion, Serbanescu, Alexandru, Culea-Florescu, Anisia, Rau, Miuta Carmina, & Baltag, Octavian. (2018). *The MCG Filtering Based on the Phase Diagram Representation Domain.* Paper presented at the 2018 International Conference on Communications (COMM).

Saunders, F. I., & Wagoner, R. H. (1996). Forming of tailor-welded blanks. *Metallurgical and Materials transactions A, 27*(9), 2605-2616. doi: 10.1007/BF02652354

Sebestova, H., Chmelickova, H., Nozka, L., & Moudry, J. (2012). Non-destructive Real Time Monitoring of the Laser Welding Process. *Journal of Materials Engineering and Performance, 21*(5), 764-769. doi: 10.1007/s11665-012-0193-4

Sheng, Jie, Cai, Yan, Li, Fang, & Hua, Xueming. (2017). Online detection method of weld penetration based on molten pool morphology and metallic vapor radiation for fiber laser welding. *The International Journal of Advanced Manufacturing Technology, 92*(1), 231-245. doi: 10.1007/s00170-017-0129-0

Shi, W., Fang, Q., Zhu, X., Norwood, R. A., & Peyghambarian, N. (2014). Fiber lasers and their applications [Invited]. *Applied Optics, 53*(28), 6554-6568. doi: 10.1364/AO.53.006554

Sibillano, T., Rizzi, D., Ancona, A., Saludes-Rodil, S., Rodríguez Nieto, J., Chmelíčková, H., & Šebestová, H. (2012). Spectroscopic monitoring of penetration depth in CO2 Nd:YAG and fiber laser welding processes. *Journal of Materials Processing Technology, 212*(4), 910-916. doi: https://doi.org/10.1016/j.jmatprotec.2011.11.016

Simon, G., Gratzke, U., & Kroos, J. (1993). Analysis of heat conduction in deep penetration welding with a time-modulated laser beam. *Journal of Physics D: Applied Physics, 26*(5), 862-869. doi: 10.1088/0022-3727/26/5/022

Singh, P. Johan, Achar, D. R. G., Guha, B., & Nordberg, H. (2002). Influence of weld geometry and process on fatigue crack growth characteristics of AISI 304L cruciform joints containing lack of penetration defects. *Science and Technology of Welding and Joining, 7*(5), 306-312. doi: 10.1080/174329313X13789830157465

Smith, Elizabeth Therese. (1999). *Monitoring laser weld quality using acoustic signals.*

Smith, Steven W. (1997). *The scientist and engineer's guide to digital signal processing* (Vol. 14): California Technical Pub. San Diego.

Sokolov, M., Salminen, A., Kuznetsov, M., & Tsibulskiy, I. (2011). Laser welding and weld hardness analysis of thick section S355 structural steel. *Materials & Design, 32*(10), 5127-5131. doi: https://doi.org/10.1016/j.matdes.2011.05.053

Staszewski, W. J., & Worden, K. (2009). Signal processing for damage detection. *Encyclopedia of structural health monitoring*.

Steen, W. M, & Mazumder, J. (2010). *Laser material processing*: springer science & business media.

Stout, R. D., & Doty, W. D. (1971). *Weldability of steels*: Welding Research Council.

Su, Jinlong, Qiu, Xiaoming, Xing, Fei, & Ruan, Ye. (2019). Effect of Preheating Temperature on Microstructure and Properties of 42CrMo4/38MnVS6 Heterogeneous Laser Welded Joint. *Metals, 9*(8), 870.

Sun, A., Asibu, E. K., & Gartner, M. (2000). Real-time monitoring of laser weld penetration using sensor fusion. *International Congress on Applications of Lasers & Electro-Optics, 2000*(1), E24-E34. doi: 10.2351/1.5059502

Sun, A., Kannatey-Asibu, E., & Gartner, M. (1999). Sensor systems for real-time monitoring of laser weld quality. *Journal of Laser Applications, 11*(4), 153-168. doi: 10.2351/1.521893

Sun, A., Kannatey-Asibu, E., Williams, W., & Gartner, M. (2001). *Time-frequency analysis of laser weld signature* (Vol. 4474): SPIE.

Szymanski, Z., Hoffman, J., & Kurzyna, J. (2000). Plasma plume oscillations during welding of thin metal sheets with a CW CO_2 laser. *Journal of Physics D: Applied Physics, 34*(2), 189-199. doi: 10.1088/0022-3727/34/2/307

Thomy, C., Seefeld, T., & Vollertsen, F. (2008). Humping Effect in Welding of Steel with Single-Mode Fibre Laser. *Welding in the World, 52*(5), 9-18. doi: 10.1007/BF03266636

Tisza, Miklós. (2013). Recent development trends in sheet metal forming. *Int. J. of Microstructure and Materials Properties, 8*, 125-140. doi: 10.1504/IJMMP.2013.052651

Tomaz, I. V., Colaço, F. H. G., Sarfraz, S., Pimenov, D. Y., Gupta, M. K., & Pintaude, G. (2021). Investigations on quality characteristics in gas tungsten arc welding process using artificial neural network integrated with genetic algorithm. *The International Journal of Advanced Manufacturing Technology, 113*(11), 3569-3583. doi: 10.1007/s00170-021-06846-5

Vaissiere, L, Laurent, JP, & Reinhardt, A. (2002). Development of pre-coated boron steel for applications on PSA Peugeot Citroen and Renault bodies in white: SAE Technical Paper.

Valencia, D., Orejuela, D., Salazar, J., & Valencia, D. (2016). *Comparison analysis between rigrsure, sqtwolog, heursure and minimaxi techniques using hard and soft thresholding methods.* Paper presented at the 2016 XXI Symposium on Signal Processing, Images and Artificial Vision (STSIVA).

Verma, N., & Verma, A. K. (2012). Performance analysis of wavelet thresholding methods in denoising of audio signals of some Indian Musical Instruments. *Int. J. Eng. Sci. Technol, 4*(5), 2040-2045.

Vidal, F, Pineiro, E, Mato, JL, Besteiro, R, Varela, R, Rodriguez, MJ, & Meizoso, F. (2010). *Defect Characterization in Tailor Welded Blanks using an Eddy Current and Harmonic Flux Leakage Integration.* Paper presented at the Proceedings of 10th European Conference on Non-Destructive Testing, Moscow.

Volpp, J. (2017). Keyhole stability during laser welding—Part II: process pores and spatters. *Production Engineering, 11*(1), 9-18. doi: 10.1007/s11740-016-0705-4

von Witzendorff, P., Kaierle, S., Suttmann, O., & Overmeyer, L. (2015). Using pulse shaping to control temporal strain development and solidification cracking in pulsed laser welding of 6082 aluminum alloys. *Journal of Materials Processing Technology, 225*, 162-169. doi: https://doi.org/10.1016/j.jmatprotec.2015.06.007

Wahba, M., Mizutani, M., Kawahito, Y., & Katayama, S. (2010). Keyhole stability in disc laser welding of AZ31B and AZ61A magnesium alloys and weld metal properties. *Science and Technology of Welding and Joining, 15*(7), 559-566. doi: 10.1179/136217110X12720264008592

Wan, X., Wang, Y., Zhao, D., Huang, Y., & Yin, Z. (2017). Weld quality monitoring research in small scale resistance spot welding by dynamic resistance and neural network. *Measurement, 99*, 120-127. doi: https://doi.org/10.1016/j.measurement.2016.12.010

Wang, P., Chen, X., Pan, Q., Madigan, B., & Long, J. (2016). Laser welding dissimilar materials of aluminum to steel: an overview. *The International Journal of Advanced Manufacturing Technology, 87*(9), 3081-3090. doi: 10.1007/s00170-016-8725-y

Weckman, D. C., Kerr, H. W., & Liu, J. T. (1997). The effects of process variables on pulsed Nd:YAG laser spot welds: Part II. AA 1100 aluminum and comparison to AISI 409 stainless steel. *Metallurgical and Materials Transactions B, 28*(4), 687-700. doi: 10.1007/s11663-997-0043-1

Weerasinghe, V. M., Kamalu, J. N., Hibberd, R. D., & Steen, W. M. (1990). Acoustic signals from laser back reflections. *Optics & Laser Technology, 22*(6), 381-386. doi: https://doi.org/10.1016/0030-3992(90)90091-H

Westerbaan, D., Parkes, D., Nayak, S. S., Chen, D. L., Biro, E., Goodwin, F., & Zhou, Y. (2014). Effects of concavity on tensile and fatigue properties in fibre laser welding of automotive steels. *Science and Technology of Welding and Joining, 19*(1), 60-68. doi: 10.1179/1362171813Y.0000000163

Wu, D. J., Ma, G. Y., Niu, F. Y., & Guo, D. M. (2013). Pulsed Laser Welding of Hastelloy C-276: High-Temperature Mechanical Properties and Microstructure. *Materials and Manufacturing Processes, 28*(5), 524-528. doi: 10.1080/10426914.2012.736652

Wu, G. D., & Lo, S. L. (2010). Effects of data normalization and inherent-factor on decision of optimal coagulant dosage in water treatment by artificial neural network. *Expert Systems with Applications, 37*(7), 4974-4983. doi: https://doi.org/10.1016/j.eswa.2009.12.016

Yaakob, KI, Ishak, M, & Idris, SRA. (2017). The effect of pulse welding parameters on weld geometry of boron steel using low power fibre laser. *Journal of Mechanical Engineering and Sciences, 11*(3), 2895-2905.

Yan, F., Liu, S., Hu, C., Wang, Ch., & Hu, X. (2017). Liquation cracking behavior and control in the heat affected zone of GH909 alloy during Nd: YAG laser welding. *Journal of Materials Processing Technology, 244*, 44-50. doi: https://doi.org/10.1016/j.jmatprotec.2017.01.018

You, D. Y., Gao, X. D., & Katayama, S. (2014). Review of laser welding monitoring. *Science and Technology of Welding and Joining, 19*(3), 181-201. doi: 10.1179/1362171813Y.0000000180

Young, D., & Roychoudhuri, C. (2003). Results and comparison of a cladding pumped fiber simulation using a decagon-shaped fiber. *Optics express, 11*(7), 830-837. doi: 10.1364/OE.11.000830

Yu, Hao, & Wilamowski, Bogdan M. (2011). Levenberg-marquardt training. *Industrial electronics handbook, 5*(12), 1.

Zhang, M. J., Chen, G. Y., Zhou, Y., Li, S. C., & Deng, H. (2013). Observation of spatter formation mechanisms in high-power fiber laser welding of thick plate. *Applied Surface Science, 280*, 868-875. doi: https://doi.org/10.1016/j.apsusc.2013.05.081

Zhang, Tianhu, & You, Xueyi. (2015). Improvement of the Training and Normalization Method of Artificial Neural Network in the Prediction of Indoor Environment. *Procedia Engineering, 121*, 1245-1251. doi: https://doi.org/10.1016/j.proeng.2015.09.152

Zhang, Y., Shi, R., & Li, L. (2012). Determination of energy coupling to material in laser welding by a novel "sandwich" method. *Transactions of Nonferrous Metals Society of China, 22*(7), 1701-1710. doi: https://doi.org/10.1016/S1003-6326(11)61376-9

Zhang, Y., Ying, Y., Liu, X., & Wei, H. (2016). Deformation control during the laser welding of a Ti6Al4V thin plate using a synchronous gas cooling method. *Materials & Design, 90*, 931-941. doi: https://doi.org/10.1016/j.matdes.2015.11.035

Zhang, Z., Chen, H., Xu, Y., Zhong, J., Lv, N., & Chen, S. (2015). Multisensor-based real-time quality monitoring by means of feature extraction, selection and modeling for Al alloy in arc welding. *Mechanical Systems and Signal Processing, 60-61*, 151-165. doi: https://doi.org/10.1016/j.ymssp.2014.12.021

Zhang, Z., Kannatey-Asibu, E., Chen, S., Huang, Y., & Xu, Y. (2015). Online defect detection of Al alloy in arc welding based on feature extraction of arc spectroscopy signal. *The International Journal of Advanced Manufacturing Technology, 79*(9), 2067-2077. doi: 10.1007/s00170-015-6966-9

Zhao, D., Wang, Y., Liang, D., & Ivanov, M. (2020). Performances of regression model and artificial neural network in monitoring welding quality based on power signal. *Journal of Materials Research and Technology, 9*(2), 1231-1240. doi: https://doi.org/10.1016/j.jmrt.2019.11.050

Zhou, J., & Tsai, H. L. (2006). Porosity Formation and Prevention in Pulsed Laser Welding. *Journal of Heat Transfer, 129*(8), 1014-1024. doi: 10.1115/1.2724846

Zhou, K., Taigang, Liu, & Lifeng, Zhou. (2015, 15-17 Aug. 2015). *Industry 4.0: Towards future industrial opportunities and challenges.* Paper presented at the 2015 12th International Conference on Fuzzy Systems and Knowledge Discovery (FSKD).

APPENDICES

Appendix A:

ACADEMIC CONTRIBUTIONS

Journal

1. Yusof, M. F. M., Ishak, M., & Ghazali, M. F. (2020). Weld depth estimation during pulse mode laser welding process by the analysis of the acquired sound using feature extraction analysis and artificial neural network. *Journal of Manufacturing Processes*. Available online 18 May 2020, In Press, Corrected Proof. https://doi.org/10.1016/j.jmapro.2020.04.004

2. Yusof, M. F. M., Ishak, M., & Ghazali, M. F. (2020). Classification of weld penetration condition through synchrosqueezed-wavelet analysis of sound signal acquired from pulse mode laser welding process. *Journal of Materials Processing Technology*, *279*, 116559.

3. Yusof, M. F. M., Ishak, M., & Ghazali, M. F. (2019). L-Statistical Analysis of Sound Signal Acquired from Pulse Mode Laser Welding for Characterising Weld Geometry. *International Journal of Automotive and Mechanical Engineering*, *16*, 6987-7006.

Proceeding Journal

1. Yusof, M. F. M., Ishak, M., & Ghazali, M. F. (2020, April). Detection of irregularities on weld bead from the L-Statistic analysis of the acquired sound during pulse mode laser welding process. In *IOP Conference Series: Materials Science and Engineering* (Vol. 788, No. 1, p. 012015). IOP Publishing.

2. Yusof, M. F. M., Ishak, M., & Ghazali, M. F. (2017, September). Feasibility of using acoustic method in monitoring the penetration status during the Pulse Mode Laser Welding process. In *IOP Conference Series: Materials Science and Engineering* (Vol. 238, p. 012006).

Appendix B:

CHEMICAL COMPOSITIONS TEST REPORT

Element %	Burn 1	Burn 2	Burn 3	Burn 4	Burn 5	Average
Fe	98	97.9	98	98	98	97.98
C	0.215	0.252	0.249	0.271	0.26	0.2494
Si	0.243	0.241	0.238	0.225	0.228	0.235
Mn	1.17	1.17	1.12	1.16	1.15	1.154
P	0.0089	0.0094	0.0082	0.0096	0.01	0.00922
Si	< 0.003	< 0.003	< 0.003	< 0.003	< 0.003	< 0.003
Cr	0.146	0.149	0.149	0.147	0.146	0.1474
Mo	< 0.005	< 0.005	< 0.005	< 0.005	< 0.005	< 0.005
Ni	< 0.005	0.0055	< 0.005	< 0.005	< 0.005	< 0.005
Al	0.106	0.095	0.0595	0.0614	0.0606	0.0765
Co	<0.001	< 0.001	< 0.001	< 0.001	< 0.001	< 0.001
Cu	0.0052	0.0048	0.0039	0.0047	0.0049	0.0047
Nb	0.0165	0.0164	0.0148	0.0157	0.015	0.01568
Ti	0.0394	0.0401	0.0374	0.0394	0.0375	0.03876
V	<0.002	< 0.002	< 0.002	< 0.002	< 0.002	< 0.002
W	<0.0150	< 0.0150	< 0.0150	< 0.0150	< 0.0150	< 0.0150
Pb	<0.0250	< 0.0250	< 0.0250	< 0.0250	< 0.0250	< 0.0250
Sn	< 0.0020	< 0.0020	< 0.0020	< 0.0020	< 0.0020	< 0.0020
B	0.0026	0.0027	0.0026	0.003	0.0029	0.00276
Ca	> 0.001	> 0.001	> 0.001	> 0.001	> 0.001	> 0.001
Zr	0.0033	0.0045	< 0.002	0.0029	0.0032	0.003475
As	< 0.0050	< 0.0050	< 0.0050	< 0.0050	< 0.0050	< 0.0050
Bi	< 0.0300	< 0.0300	< 0.0300	< 0.0300	< 0.0300	< 0.0300